

## AN ABSTRACT OF THE THESIS OF

Larry A. Silva for the degree of Doctor of Philosophy in Physics presented on August 17, 1989.

Title: The Optical Properties of Liquid Se-Te Alloys

Redacted for Privacy

Abstract approved: \_

Melvin Cutler

Techniques have been developed to prepare films of liquid semiconductors with sub-micrometer thicknesses. This makes it possible to determine the complex dielectric function at photon energies where interband transitions take place using information about both the transmissivity and reflectivity of the liquid, and provides a more direct probe of the electronic structure than an analysis of the reflectivity properties alone.

Optical measurements have been performed on the liquid system  $\text{Se}_x\text{Te}_{1-x}$  in composition steps of 20 atomic percent, and at temperatures from the melting point to 500°C. In this range of temperatures the optical absorption data for the liquids containing 0-80% Te show the presence of an optical band gap; these liquids are semiconductors. Possible forms for the density of electron states at the valence and conduction band edges have been derived using the non-direct transition model for optical absorption.

Evidence for the onset of a transition from semiconducting to metal-like properties first appears in the  $\text{Se}_{20}\text{Te}_{80}$  data at the highest measured temperatures. The data for liquid Te clearly show semimetallic properties: the reflectivity is large at far-infrared photon energies, decreasing at higher energies, and the absorption

coefficient data extrapolate to a negative band gap energy. The complex dielectric function of liquid Te has been separated into interband and intraband components using the Drude model to determine the optical properties of the free charge carriers (holes). The energy dependence of the interband component of the data was found to be consistent with the preservation of 2-fold bonding across the semiconductor-semimetal transition.

Data for the absorption coefficient at photon energies below the band gap of the Se-rich liquids have also been measured. The absorption edge of pure Se varies exponentially with photon energy. The behavior of the edge in the alloys is similar to that of Se, but a non-exponential tail is present at the lowest absorption levels measured. The exponential portion of the absorption edge could be represented by the Urbach equation  $\alpha = e^{12.0} e^{(\hbar\omega - E_0)\sigma/kT}$ , with  $\sigma$  a function of temperature and composition, and  $E_0$  a function of composition alone.

The Optical Properties of Liquid Se-Te Alloys

by

Larry A. Silva

A THESIS

submitted to

Oregon State University

in partial fulfillment of  
the requirements for the  
degree of

Doctor of Philosophy

Completed August 17, 1989

Commencement June 1990

Approved:

Redacted for Privacy

---

Professor in Physics in charge of major

Redacted for Privacy

---

Chairman of the Department of Physics

Redacted for Privacy

---

Dean of the Graduate School

Date thesis is presented August 17, 1989

Typed by Larry Silva for Larry Silva

## TABLE OF CONTENTS

### 1. Background

1.1 Optical Properties of Liquid Metals	1
1.2 Optical Properties of Liquid Semiconductors	5
1.2.1 The Fundamental Absorption Band	7
1.2.2 The Absorption Edge	15
1.3 Semiconductor-Semimetal Transition in Se-Te Alloys	20
1.3.1 From Order to Disorder	20
1.3.2 The Semiconductor to Semimetal Transition	26
1.4 Objectives of this Work	30

### 2. The Optical Measurements

2.1 Optical Measurements on Thin Film Samples	32
2.1.1 Film Preparation	32
2.1.2 Reflectivity and Transmissivity Measurements	32
2.1.3 Cell Measurements and the Refractive Index of the Liquid	35
2.1.4 Determining the Film Thickness	37
2.1.5 Calculating the Refractive Index of the Liquid	39
2.2 Reflectivity Measurements	40
2.3 Errors and Uncertainties	43
2.3.1 Equipment Limitations	44
2.3.2 Sample Conditions	45
2.3.3 Film Thickness Measurements	47

### 3. Presentation of Results

3.1 Reflectivity	49
3.2 Absorption Coefficient above the Band Gap	51

3.3 Dielectric Function	57
3.4 The Absorption Edge	62
<b>4. The Density of Electron States in the Semiconducting Alloys</b>	<b>65</b>
4.1 $ M ^2$ Constant	68
4.2 $ M ^2$ Energy Dependent	74
4.3 Summary	77
<b>5. The Semiconductor-Semimetal Transition</b>	<b>79</b>
5.1 Optical Transitions, and the Drude Model	80
5.2 The Intraband and Interband Optical Components	86
5.3 Implications for the Microscopic Structure	90
<b>6. The Absorption Edge</b>	<b>92</b>
6.1 Comparison of Experimental Data	92
6.2 Absorption Processes in the Liquid	99
<b>7. Summary</b>	<b>103</b>
 <b>Bibliography</b>	 <b>107</b>
<b>Appendix A Methods for Producing Thin Films of High Temperature Liquids</b>	<b>110</b>

## LIST OF FIGURES

1.1 The complex dielectric function of liquid Sn, and the Drude model fit to the data.	4
1.2 The optical conductivity of liquid and solid Pb.	6
1.3 The energy dependence of the dipole matrix function for optical transitions in trigonal and amorphous Se as calculated by Mashke and Thomas.	11
1.4 The energy dependence of the dipole matrix element function as derived by Abe and Toyozawa.	12
1.5 The crystal structure of trigonal selenium and tellurium.	22
1.6 The band structure and density of states in trigonal Se and Te.	23
1.7 X-ray and UV photoemission results on trigonal and amorphous Se and Te.	23
1.8 Optical absorption edges in amorphous and crystalline Se and Te.	25
1.9 Density of states models for the semiconductor-semimetal transition.	29
2.1 Apparatus for measuring film reflectance and transmittance.	34
2.2 Diagram of film interference parameters.	36
2.3 The cell and clamp used to measure the reflectivity of the liquid.	41
2.4 Apparatus for reflectivity measurements.	42
3.1 A representative set of curves for the reflectivity of Se-Te liquids.	50
3.2 The absorption coefficient of the liquid.	52
3.3 Detail of the absorption edge above the band gap.	53
3.4 Two views of the changes in the 'band gap' energy $E_g$ .	55
3.5 The real part of the complex dielectric function.	58
3.6 The imaginary part of the complex dielectric function.	59
3.7 Detailed view of the complex dielectric function for the Se-rich alloys.	60

3.8 Data for the complex dielectric function of liquid Te.	61
3.9 The absorption coefficient below the band gap.	63
4.1 The energy dependence of the quantity $\epsilon_2(\hbar\omega)^2$ in liquid Se at 250, 400°C	66
4.2 $\epsilon_2(\hbar\omega)^2$ vs. $\hbar\omega$ for the alloys containing 0-80% Te.	66
4.3 Band states calculated with the approximation $N_c(E) = N_v(E)$ .	69
4.4 Valence band density of states calculated by Kao and Cutler for metallic Se-Te alloys.	71
4.5 $N_c(E)$ for a parabolic valance band.	73
4.6 The energy dependence of the average dipole matrix function if the valence and conduction bands are taken to be parabolic.	76
4.7 The composition dependence of the calculated average dipole matrix function.	76
5.1 The band structure model used to separate the intra- and inter-band contributions to the optical data.	81
5.2 The volume contraction plotted against the hole concentration in the liquid.	85
5.3 The factor $(1/\hbar\omega N_F^2) \int N(E) N(E+\hbar\omega) dE$ for a parabolic conduction band and $E_F = 1\text{eV}$ .	85
5.4 The measured complex dielectric function of liquid Te at 445°C $\epsilon_m$ separated into interband $\epsilon$ and intraband $\sigma/\omega$ components.	88
5.5 Data for the measured absorption coefficient of liquid Te plotted along with the absorption coefficient of the calculated interband component.	89
5.6 The effect of changing the ratio $(m^*/n)$ on the calculated interband absorption.	89
6.1 The exponential absorption in liquid selenium.	94
6.2 The exponential absorption in liquid $\text{Se}_{80}\text{Te}_{20}$ .	95
6.3 The exponential absorption in liquid $\text{Se}_{60}\text{Te}_{40}$ .	96
6.4 The temperature dependence of the steepness parameter $\sigma$ .	97
6.5 Values for the steepness parameter $\sigma$ from different measurements.	97



## **LIST OF APPENDIX FIGURES**

- |   |     |
|---|-----|
| 1. The optical cell and clamp.  | 115 |
| 2. An example of the measurements obtained using the optical cell shown in Fig 1. | 116 |
| 3. Two optical cell designs used with the compressed-liquid technique.            | 117 |

## **LIST OF TABLES**

1.1 Liquid semiconductors whose optical properties have been determined above the band gap.	13
3.1 Parameters for the fundamental absorption edge in Se-Te alloys.	56
5.1 The free-carrier parameters for the valence band holes.	84

## Preface

Liquid  $\text{Se}_x\text{Te}_{1-x}$  is one of many binary liquid systems which exhibit a transition from semiconducting to metallic behavior as the composition is varied. This work focuses on examining how the electronic transition in Se-Te alloys affects the optical properties in the spectral region near and above the optical band gap. The measurement of the data to be presented was made possible by the development of special techniques to prepare optically flat liquid film samples at high temperatures with submicron thicknesses.

The chapters are organized as follows. The first chapter reviews the theories and experimental information necessary to understand the physics of the transition. In sections 1.1 and 1.2 the optical properties of liquid metals and semiconductors are reviewed in general. The metal-semiconductor transition in liquid Se-Te alloys is also accompanied by changes in the thermodynamic and structural properties; in section 1.3 the nature of these changes is discussed, along with currently proposed models for the mechanism behind the transition. Chapters 2 and 3 cover the experimental aspects of this work-- how the optical data were obtained, their accuracy, and a comparison of the results to previous optical measurements on this liquid system. In chapters 4 and 5 the fundamental absorption band (absorption above the band gap) is examined with the aim of understanding the band structure in the semiconducting phase of the liquid, and how this band structure changes in the transition to the metal-like phase. Data for the absorption edge (absorption below the band gap) of the semiconducting alloys has also been obtained in this experiment; they are discussed in chapter 6. The final chapter presents a summary of the conclusions of this work.

# The Optical Properties of Liquid Se-Te Alloys

## 1. Background

### 1.1 Optical Properties of Liquid Metals

Materials which fall in the classification of 'liquid metals' include the elements which are also metallic or semimetallic in the solid phase, elements such as Si and Ge which are normally semiconducting in the solid phase but which undergo changes in local atomic bonding to form a metallic state upon melting, and a wide range of low resistance alloy systems. The distinction between liquid metals and liquids which may better be described as semiconducting is not a clear one; an examination of the values of the conductivity  $\sigma$  compiled by Mott and Davis for several liquids shows that there is not a natural break in  $\sigma$  between low and high conductivity materials [1]. The magnitude of  $\sigma$  for many liquids places them in a 'grey' area, and different authors may refer to them as metallic, semiconducting, or perhaps semimetallic. In general, though, liquid metals are taken to be those materials with a conductivity higher than about  $5000 \text{ cm}^{-1}\Omega^{-1}$ . Most of the optical measurements done on liquid metals have been on single element liquids; the discussion given here will focus on this work.

Because transmissivity measurements have not been feasible for liquid metals, all of the optical parameters found thus far have been determined from variations in the reflectivity of the liquid. Two parameters are required to characterize the optical dispersion of a metal, therefore two independent reflectivity parameters have to be measured. The possibilities include changes in the phase, polarization, or intensity of the reflected light, at a single angle of incidence or two different angles. An alternative approach is to measure one of the

optical parameters over as wide a wavelength range as possible and deduce the complementary optical parameter by using the Kramers-Kronig relations.

Regardless of the measurement technique used, it is necessary to model the character of the liquid surface in order to relate the reflectivity data to the optical parameters. Usually the simplest possible model is applied: it is assumed that the surface is abrupt and the dielectric function changes sharply between the metal and the window or vacuum on the other side of the interface; usually it is also tacitly assumed that the optical behavior of the metal near the surface is the same as that in the interior of the liquid. In some cases where an oxide layer is known to be on the surface, the data analysis is modified slightly to take this into consideration.

The relation between the dispersion characteristics of liquid metals and their electronic structure has been derived by several authors from different points of view. Faber [2] derived an expression for  $\sigma(\omega)$  based on a pseudo particle view of the electrons in the limit where the electron-ion scattering is weak and the Born approximation is valid. Sturm and Pajanne [3] have also derived an expression for  $\sigma(\omega)$  in the weak scattering limit; their result relates the high frequency conductivity to the dc conductivity model developed by Ziman. Tosi *et al* have attempted to describe the optical properties of liquid metals in the strong scattering limit by treating the liquid as a two component system-- ions and electrons-- using three partial structure factors to model their interaction in the presence of an applied field [4].

The curious aspect of all the theoretical optical work is that in the appropriate limits the results should correspond to the simplest of all models, the Drude model. This model is based on treating the valence electrons as classical free particles which are scattered by the atomic cores as they are accelerated by

the electric field. The resulting optical conductivity and real dielectric function are given by

$$\begin{aligned}\sigma(\omega) &= \frac{ne^2\tau/m}{1 + \omega^2\tau^2} = \frac{\sigma_0}{1 + \omega^2\tau^2} \\ \epsilon(\omega) - 1 &= -\frac{\sigma_0}{\omega} \frac{\omega\tau}{1 + \omega^2\tau^2}\end{aligned}\tag{1.1}$$

where  $n$  is the free carrier density,  $m$  is the carrier mass, and  $\tau$  is the relaxation time. The quantity  $\sigma_0 = (ne^2\tau/m)$  is just the dc conductivity predicted by the Drude model. While the ansatz used to derive this result is certainly not correct from a quantum mechanical point of view, it has been found experimentally that the optical behavior of many liquid metals follows this simple form. A good example of Drude-like behavior is given by Sn, Fig 1.1 [5]. Characteristic of most liquid metals, the data for the complex conductivity  $\epsilon_1 + i\epsilon_2$  are smooth and relatively featureless, and show no indication of the presence of residual band structure from the solid phase. It should be pointed out that the close fit of Eq 1.1 to the optical data is often achieved by treating  $n$  and  $\tau$  as adjustable parameters. In the Drude model the carrier density is just the product of the valency of the atoms and the atomic density in the liquid, and the relaxation time is found from the value of the dc conductivity. Faber has tabulated the exact Drude parameters for several liquid metals along with the values which have been used to match the reflectivity data. The differences between the two sets of numbers are on the order of several percent.

Among single-element liquid metals, the transition metals form the main exceptions to Drude behavior. This is because of the close proximity of the d bands to the conduction band of the liquid. In the case of the noble metals Ag, Au, and Cu, the highest filled d states are only a few eV below the Fermi level. This affects the optical behavior in two ways. At UV energies, direct excitation of electrons

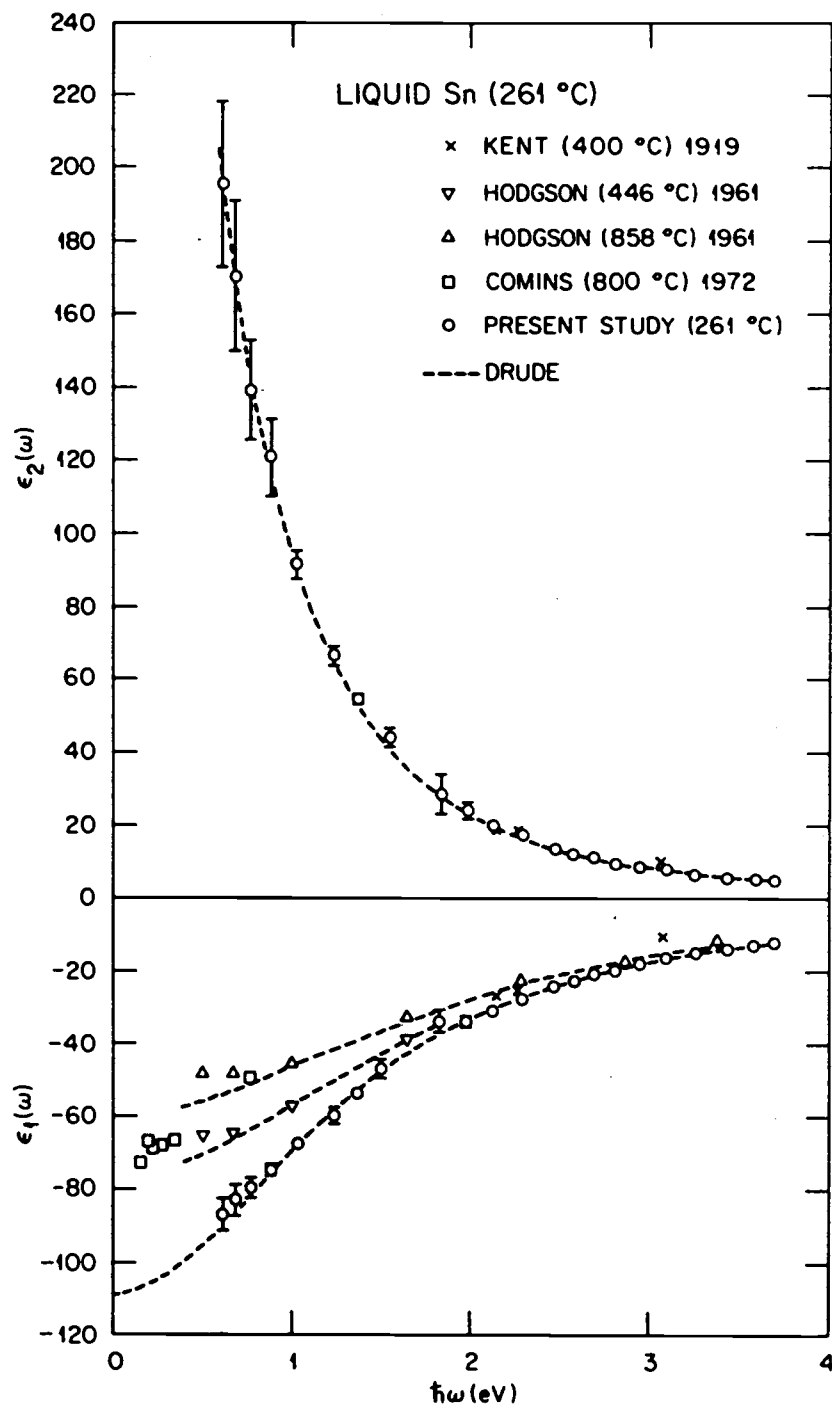


**Fig 1.1** The complex dielectric function of liquid Sn, and the Drude model fit to the data.

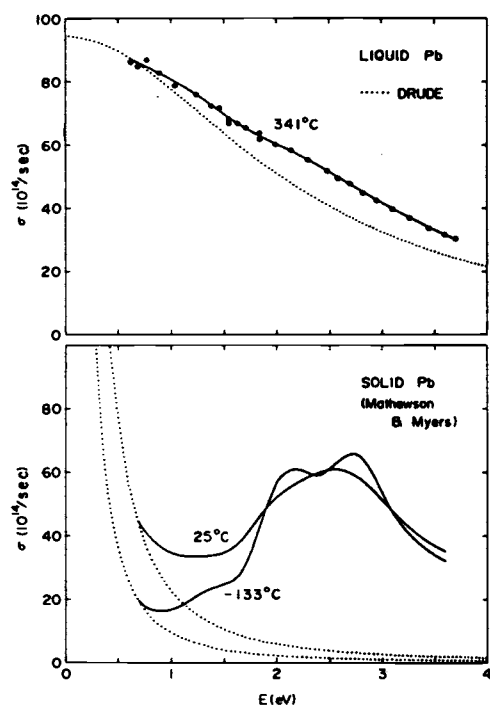
from the d band to states above the Fermi level produces distinct features in  $\sigma$  and  $\epsilon$  similar to those seen in the solid metal; and at lower photon energies there is a significant contribution to  $\epsilon$  from virtual excitations of the same sort. If the d band contribution to  $\epsilon$  is subtracted from the low energy data, however, the data for  $\epsilon$  and  $\sigma$  are still fit by Eq 1.1. For the transition elements with fewer d electrons the situation is complicated by the fact that the d band energy levels overlap the conduction band, and both bands will contribute to the optical behavior.

Until recently it was generally thought that no interband features were present in the optical spectra of liquid metals; ie, while intraband behavior and the effects of electron states below the conduction band were seen, it was thought there were no transitions from the Fermi level to any additional band structure above the conduction band. This was accepted on the grounds that the interband features seen in solid metals were the result of local bonding structure, and this was completely lost in the liquid state. However, in the case of liquid Pb at least, ultraviolet photoemission spectra and accurate ellipsometer reflectivity measurements have shown that features in the density of states structure of the solid can persist in the liquid. The results for Pb found by Inagaki *et al* [6] are shown in Fig 1.2. In (a) the optical conductivity of liquid Pb is compared to that of the solid. The solid clearly displays interband features above 1eV, whereas the liquid has a small excess conductivity above the Drude curve in the same region. By subtracting the Drude contribution from  $\sigma(\omega)$  the similarity of the interband behavior becomes apparent, (b).

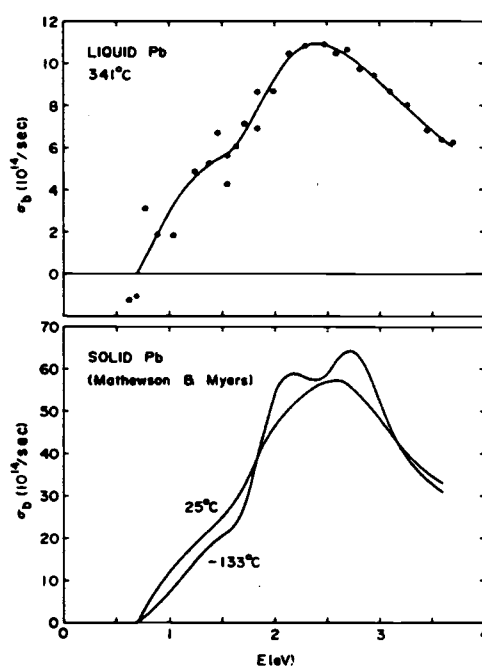
## 1.2 Optical Properties of Liquid Semiconductors

As mentioned in section 1.1, the boundary between liquid semiconductors and liquid metals is arbitrary when the conductivity is of order  $1000 \text{ cm}^{-1}\Omega^{-1}$ . At





(a)



(b)

**Fig 1.2** (a) The optical conductivity of liquid and solid Pb as a function of photon energy. (b) The interband optical conductivity found by subtracting the intraband (Drude) contribution to the data in (a).

the low conductivity end of the scale, liquid semiconductors are distinguished from other high resistance liquids-- molecular liquids (eg water), and molten salts (eg molten NaCl)-- in that they conduct electronically. The elements which are semiconductors in the liquid phase at normal pressures are S, Se, As, B, I, and P. Binary, tertiary, and more complicated compound liquid semiconductors can be prepared as well; many of the alloys that have been studied contain an chalcogenide element (group VIB of the periodic chart). There are also interesting binary systems such as Mg-Bi, where the two constituents by themselves are good liquid metals, but when combined near a certain stoichiometry the liquid becomes a semiconductor.

A discussion of the optical properties of liquid semiconductors can be divided into two parts: the behavior in the region of the absorption edge below the optical band gap, where phonons, excitons, impurities and defect states can be expected to play a role, and the behavior in the fundamental absorption band above the optical band gap, where interband transitions are the dominant optical mechanism. The optical properties above and below the band gap will be discussed in the next two subsections.

### 1.2.1 The Fundamental Absorption Band

#### a) *The Non-direct Transition Model*

The standard model used for the optical properties of liquid semiconductors is one originally proposed to explain the properties of solid amorphous semiconductors [7]. In this model it is assumed that disorder in noncrystalline materials produces a strong interaction between the valence electrons and the atomic cores, strong enough that wavevector conservation rules for electronic

transition which conserves energy is allowed to take place. This model has come to be known as the 'non-direct transition' model, or NDT model. A simple derivation using linear response theory leads to the following expression for the imaginary part of the dielectric function

$$\epsilon_2 = 2\Omega \left( \frac{\pi e \hbar}{m} \right)^2 \frac{1}{(\hbar\omega)^2} \int_{-\infty}^{\infty} N_v(E) N_c(E + \hbar\omega) |M(\hbar\omega)|^2 dE \quad (1.2)$$

This is for a semiconductor with valence and conduction band state densities  $N_v$  and  $N_c$ , respectively;  $m$  is the optical effective mass of the electron, and  $\Omega$  is the volume of a unit cell. The function  $|M(\hbar\omega)|^2$  is the average squared dipole matrix element between all states which can be coupled by a photon of energy  $\hbar\omega$ . A further approximation often applied within the NDT model is that the function  $|M(\hbar\omega)|^2$  depends only weakly on  $\hbar\omega$ , and can be treated as a constant. This leaves an expression for  $(\hbar\omega)^2 \epsilon_2$  which is proportional to the convolution of the density of states. Theoretical justification for this approximation can be found in work done by Hindley [8]. He developed a 'random phase model' for the transport and optical properties of disordered materials in which the phase of the probability amplitude for finding an electron on a particular atomic site varies randomly from atom to atom. Hindley derived a general expression for the matrix element of an arbitrary operator between a pair of such electronic states, and applying this to the dipole operator  $\partial/\partial x$  he argued that the average matrix element function  $|M(\hbar\omega)|^2$  is dominated by a single constant term, namely, the *intra* site coupling term.

The NDT model has been used to infer information about the shape of the valence band and conduction band edges in liquid and amorphous materials by

assuming that both edges can be represented by a simple power law separated by an energy gap  $E_g$ . If  $N_v \propto E^{r_v}$ ,  $N_c \propto (E-E_g)^{r_c}$ , and  $|M|^2$  is constant then Eq 1.2 predicts  $(\hbar\omega)^2\epsilon_2$  should have the form

$$(\hbar\omega)^2\epsilon_2 = A(\hbar\omega - E_g)^r \quad r = r_v + r_c + 1 \quad (1.3)$$

where  $A$  contains the constant prefactors. For many amorphous solids  $r$  has been reported to have a value close to 2. This agrees with the usual model of parabolic band edges where  $r_v = r_c = 1/2$ , and it also tends to support the view that  $|M|^2$  is relatively constant. There are materials with a value of  $r$  quite different from 2, however. Certain multicomponent glasses have  $r=3$ , and amorphous Se and liquid  $\text{TeS}_2$  are fit with  $r$  close to 1 [9,10]. It should be noted as well that experimental data for  $\epsilon_2$  are usually smooth curves which can be fit by a range of values for  $r$  by adjusting  $A$  and  $E_g$ . Depending on the energy interval in the data being fit the value of  $r$  may vary substantially.

There have been attempts to improve the NDT model by going beyond the random phase approximation for  $|M|^2$ . Maschke and Thomas have proposed that the energy dependence of the average matrix function may be obtained from the corresponding crystal matrix elements by removing those features in the crystal spectra which can be attributed to long range order [11]. Basically, they expressed the polarization averaged complex dielectric function of the crystal in a form similar to the NDT model

$$\begin{aligned} \omega^2\epsilon_2^c &= A \left| M^{cr}(\omega) \right|^2 \sum_{n,m,k} [\delta(E_n(k) - E_m(k) + \hbar\omega)] \\ \text{crystal} \quad &= A \left| M^{cr}(\omega) \right|^2 n_j(\omega) \end{aligned}$$

$$\text{NDT model} \quad \omega^2 \epsilon_2^{\text{am}} = A |M^{\text{am}}(\omega)|^2 n_c(\omega)$$

Here the sum over crystal eigenstates  $|n,m,k\rangle$  gives the joint density of states  $n_j$ ,  $|M^{\text{cr}}(\omega)|^2$  is the average squared crystal dipole matrix element at frequency  $\omega$ ,  $n_c$  is the convolution of the density of states in the amorphous (or disordered) material, and  $|M^{\text{am}}(\omega)|^2$  is the parameter being sought. Maschke and Thomas used previously calculated band structure data for the crystal to calculate values for  $\epsilon_2^{\text{c}}$  and  $n_j$ . The ratio  $\omega^2 \epsilon_2^{\text{c}}/n_j$  then produces a curve for the energy dependence of  $|M^{\text{cr}}(\omega)|^2$ . Similarly, they used the crystal band structure to approximate the density of states in the amorphous material, which allowed them to calculate  $n_c$ , and using measured  $\epsilon_2^{\text{am}}$  data a curve for  $|M^{\text{am}}(\omega)|^2$  was obtained. This procedure was carried out for amorphous Se, Ge, and Si. Their results for Se are shown in Fig 1.3. Maschke and Thomas argued that the large peak in  $|M^{\text{cr}}(\omega)|^2$  at 4eV could be attributed to Umklapp processes in the crystal, and if this 'long range order' feature is removed the energy dependence of the two curves in Fig 1.3 would be about the same. While this approach to finding the energy dependence of the matrix elements may be valid for some materials, it has the disadvantages of being somewhat phenomenological, and requiring the existence of a crystal form that matches the structure and composition of the disordered material.

In more recent theoretical work, Abe and Toyozawa [12], and Dersch *et al* [13] have calculated the energy dependence of the matrix element function for a model two band semiconductor with random short-range disorder potentials. The model Hamiltonian used by both groups was for a set of non-interacting electrons described by tight binding wavefunctions with random diagonal energy terms

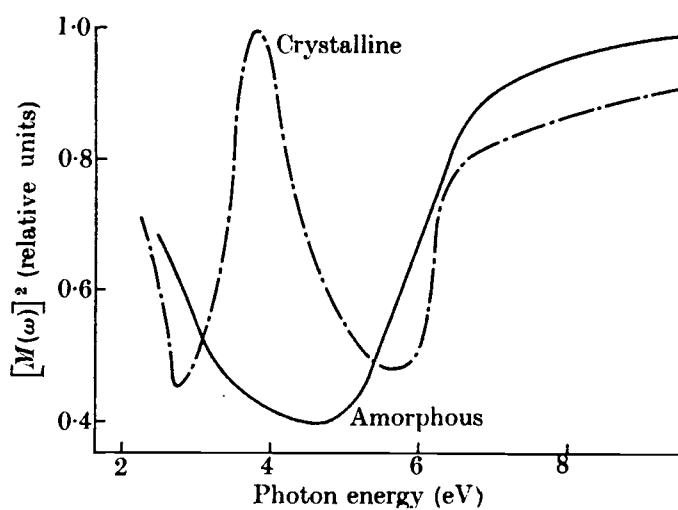


**Fig 1.3** The energy dependence of the dipole matrix function for optical transitions in trigonal and amorphous Se as calculated by Maschke and Thomas.

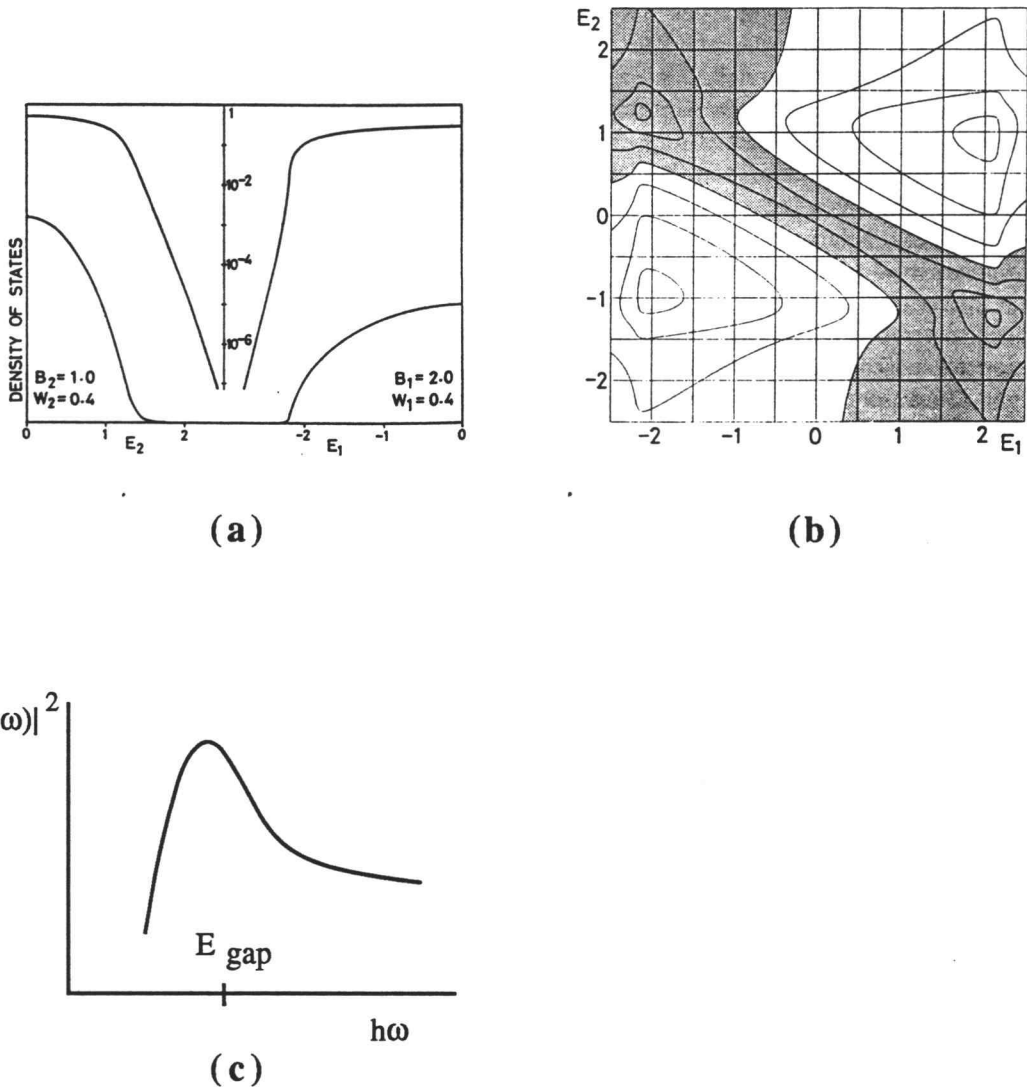


**Fig 1.4** The energy dependence of the dipole matrix element function as derived by Abe and Toyozawa. The model density of states they used is shown in (a) in both linear (lower) and logarithmic (upper) scales. Abe and Toyozawa write the NDT equation in a different form than is given in Eq. 1.2. In their notation the absorption coefficient is given by

$$\alpha(h\omega) \propto \iint N_c(E_1) N_v(E_2) M(E_1, E_2) \delta(E_1 - E_2 - h\omega) dE_1 dE_2$$

where the dipole matrix function is now a function of the electron energies  $E_1$  and  $E_2$  coupled by the photon  $h\omega$ . The calculated values for  $M(E_1, E_2)$  are plotted in (b) as a contour plot. In (c) their results are replotted in terms of the function  $|M(h\omega)|^2$  as defined in Eq. 1.2.

$$H^{\mu} = \sum_n |n\mu\rangle E_n^{\mu} \langle n\mu| + \sum_{n \neq m} |n\mu\rangle V_{nm}^{\mu} \langle m\mu|$$

The wavefunction  $|n\mu\rangle$  is for an electron at site  $n$  in either the conduction band ( $\mu=c$ ) or valence band ( $\mu=v$ );  $E_n^{\mu}$  is a random single site energy, and  $V_{nm}$  is the normal intersite energy for the ordered system. Abe and Toyozawa, and Dersch *et al* also considered the effects of short range correlations in  $E_n^{\mu}$  between the conduction band and valence band, which might be expected near charged defects and impurities, for example. Their methods for calculating the optical properties of this model system were quite different, but they both reached the general conclusion that  $|M(\hbar\omega)|^2$  is maximum at energies near the band gap, and gradually decreases at higher energies. The results obtained by Abe and Toyozawa for uncorrelated disorder potential energies  $E_n^{\mu}$  are shown in Fig 1.4.

#### b) *Experimental Work*

The optical properties of few liquid semiconductors have been measured in the fundamental absorption band region. Because of the experimental difficulties involved in making transmissivity measurements, all of the current data have been determined by reflectivity measurements alone, and these have been confined to intensity measurements at normal incident angles. The table below lists most of the materials which have been studied.

**Table 1.1** Liquid semiconductors whose optical properties have been determined above the band gap.

Liquid	Energy range of R measured (eV)	Reference
Te	0.5 - 3.0	14
S	0.5 - 5.0	15



$\text{Se}_x\text{Te}_{1-x}$	0.5 - 5.0	16,17
$\text{Ga}_x\text{Te}_{1-x}$	0.65 - 3.0	18
$\text{Tl}_x\text{Te}_{1-x}$	0.65 - 3.0	18
$\text{In}_x\text{Te}_{1-x}$	0.65 - 3.0	18
$\text{Cs}_x(\text{CsCl})_{1-x}$	0.65 - 5.5	19
$\text{TlS}_2$	0.6 - 5.0	9
<u>Hg (expanded)</u>	<u>0.5 - 4.0</u>	<u>20</u>

As can be seen from the table, measurements of R have been limited to a range of 3-5eV centered at visible energies. This makes a direct Kramers-Kroenig analysis of the data a questionable method for determining the dielectric properties; therefore, most of the optical dispersion results have been derived using one of the following two alternative methods. The simplest of the two methods is to use a model for the shape of the conduction band and valence band density of states with a few adjustable parameters for the contours of the bands and the band gap. The complex dielectric function is then determined via Eq 1.2 and a Kramers-Kronig calculation of  $\epsilon_1$  from  $\epsilon_2$ , and the fitting parameters are varied to optimize the fit between the measured reflectance and the reflectance calculated from  $\epsilon$ . This approach is useful for investigating trends in the overall features of the data with a minimal amount of computational work, but it certainly cannot be used to obtain accurate and detailed results. The second method for calculating the optical parameters of the liquid is based on using a set of classical damped harmonic oscillators as basis functions to fit the reflectivity data [21]. The functional form of  $\epsilon$  is

$$\epsilon = \epsilon_1 + i\epsilon_2 = \epsilon_\infty + \sum_{n=1}^N \frac{f_n}{1 - (\omega/\omega_n)^2 - i\Gamma_n(\omega/\omega_n)}, \quad (1.4)$$

where each oscillator introduces three adjustable parameters  $f_n$ ,  $\omega_n$ , and  $\Gamma_n$  to fit the reflectivity data. For lattice vibrations these parameters would be associated with the strength, frequency and linewidth of an oscillation mode, but in the case of interband absorption they have no physical significance. Eq 1.4 must be used carefully when calculating the dielectric dispersion because it is possible that more than one set of fitting parameters may match the reflectivity measurements. In practice, it is best to use data for the absorption coefficient of the liquid below the band gap as an additional constraint in determining the oscillator parameters.

### 1.2.2 The Absorption Edge

The type of optical absorption edge found most frequently among liquid semiconductors is an exponential, or 'Urbach' edge. This has the general form

$$\alpha(\hbar\omega) = \alpha_0 e^{\sigma(\hbar\omega - E_0)/k_B T} \quad (1.5)$$

where the parameters  $E_0$ ,  $\alpha_0$ , and  $\sigma$  may be temperature dependent. Experimental data for the absorption edge are usually presented as a plot of  $\ln(\alpha)$  versus  $\hbar\omega$ . When viewed in this way an Urbach edge appears as a line with slope  $\sigma/k_B T$  beginning in the range of  $10^4 \text{ cm}^{-1}$  to  $10^3 \text{ cm}^{-1}$  and extending down to absorption levels 2 or more decades lower in  $\alpha$ . If data at different temperatures are plotted together, a family of lines is produced with slopes that decrease with temperature; these lines usually have a common extrapolated focal point at the absorption level  $\alpha = \alpha_0$  and photon energy  $\hbar\omega = E_0$ . The magnitude of the energy term  $E_0$  is always close to the optical band gap energy of the semiconductor. Urbach absorption edges have been observed in a diverse group of materials including ionic and

covalent crystals, organic insulators, and amorphous and liquid semiconductors. In ionic crystals the steepness parameter  $\sigma$  has a specific temperature dependence

$$\sigma = \sigma_0(2k_B T/\hbar\omega_p) \tanh(\hbar\omega_p/2k_B T), \quad (1.6)$$

where  $\sigma_0$  is a constant, and  $\hbar\omega_p$  is an energy term with a magnitude of the order of a phonon energy. In disordered materials, however, the temperature dependence of  $\sigma$ ,  $\alpha_0$ , and  $E_0$  are all material-dependent.

Because an exponential edge is such a common feature among otherwise quite different materials, many researchers have come to believe that it should be attributable to some underlying universal mechanism which is material independent. An examination of the literature shows that there is no shortage of theoretical work directed at finding such a mechanism. It is outside the scope of this work to give a detailed account of the various models proposed to explain the Urbach edge; only a brief overview the subject will be given here.

The most widely quoted models for Urbach behavior are those of Sumi and Toyozawa (ST), and Dow and Redfield (DR) [22,23]. Sumi and Toyozawa propose that the Urbach edge is due to the formation of Frenkle-type excitonic states in the presence of exciton-phonon interactions. In their model, the absorption characteristics of both free and localized excitons contribute to the exponential line shape. Free excitons have an absorption line shape which is Lorentzian. ST propose that there are also momentarily localized excitonic states present which appear randomly in space and time in the course of thermal vibrations; these localized excitons have a Gaussian absorption line shape. The exponential absorption edge may be viewed as an intermediate shape between the low energy edge of the Lorentzian and Gaussian absorption curves. In the calculations done by ST the Urbach edge results from the energy dependence of the

self-energy of the exciton+many phonon system as the exciton changes character from that of a free exciton to a locally bounded exciton. More recently, Schreiber and Toyozawa [24] have performed a Monte-Carlo calculation of the exciton absorption line spectra using a model Hamiltonian for the electron-phonon interactions, without making any assumptions about the existence of momentarily localized excitons. Their calculations produced an Urbach edge with a  $T^{-1}$  temperature dependence in the slope of the edge. By considering the average oscillator strength per exciton state they concluded that the exponential shape could be attributed to the presence of localized excitons, as Sumi and Toyozawa had originally suggested.

The Dow-Redfield model for the Urbach edge is based on a very different optical mechanism. They consider the effects of strong local electric fields, or 'microfields,' on the optical absorption of Wannier-type excitons. The microfields exist on a scale large compared to interatomic distances, but smaller than  $\sim 10^3 \text{\AA}$ , and they may originate from several sources including charged defect states, LO phonons, and impurities. In the DR model a photon is absorbed via the creation of an electron-hole pair in a quantum state defined by the sum potential of their Coulombic attraction and the external field. This may be viewed as the Franz-Keldysh effect modified by including electron-hole interactions, or as excitonic absorption broadened by an external field. The absorption probability in this model depends on the the amplitude of the electron's wave function near the hole. The external field has two effects in this regard: it lowers the final energy of the electron-hole pair state, which allows photons to be absorbed well below the band gap energy, and it also decreases the probability of finding the electron near the hole, leading to an exponentially decreasing absorption cross-section. To calculate numerical values for the optical absorption within this model, Dow and Redfield

simplified the problem by considering the absorption of a Gaussian distribution of uniform external fields. Solving for the wavefunctions numerically they found that the absorption by an electron-hole pair in a field of strength  $F$  had the spectral dependence of an Urbach edge, ie  $\alpha(F, \hbar\omega) \propto \exp[(\hbar\omega - E_0)/F]$ . With a Gaussian field distribution  $P(F)$  the total absorption is the sum of the absorption contributions at each field intensity  $\alpha(\hbar\omega) = \int_0^\infty \alpha(F, \hbar\omega) P(F) dF$ . After performing this integration they found that the exponential behavior still remained over several decades of  $\alpha$ . The fact that the exponential behavior survived the field integration process is important because it indicates that the shape of the absorption edge is insensitive to the details of the field distribution. This is what allows the DR model to explain the presence of Urbach behavior in a wide range of solids and liquids.

In addition to the DR and ST models for the Urbach edge, several other models have been proposed which, in one way or another, lead to an exponential edge through the distortion of the valence and conduction band edges. Thus, Skettrup [25] has derived an exponential edge by considering thermal fluctuations in the band gap-- the idea being that the band gap in all materials depends on the temperature, and random local variations in the phonon density leads to a distribution of local band gap energies. Kolobov and Konstantinov have modeled the Urbach edge based on strain-induced shifts in the band edges [26]. Electron-phonon interactions are dealt with in terms of local strain parameters which shift the conduction band and valence band edges unequally. As with Skettrup's model there is a random distribution of local band gap energies which leads to exponentially smaller absorption levels below the average band gap. Another model for the Urbach edge, proposed several times in different forms, places its origin in the existence of exponential tails in the density of states functions for the

conduction and valence band edges. These electron tail-states are attributed to random potential fluctuations in the material caused by disorder, phonons, and impurities, but their optical properties are not treated directly. Instead, the Urbach edge is derived through the non-direct transition model by convoluting an exponential density of states function in one band with a parabolic density of states function in the other. Recent proponents of this model include Cohen [27] and John [28].

The experimental work done thus far on the behavior of Urbach edges has not singled out any one of the above models as being 'most universal.' The more phenomenological types of models dealing with distortions in the band edges are difficult to test because they do not predict what changes should be expected in the experimentally accessible parameters. They also fail to account for the fact that many materials *do not* have exponential absorption edges. There have been experiments undertaken with the goal of comparing the validity of the DR and ST models. Wiley and Thomas [29] measured the temperature and polarization dependence of the absorption edge in crystalline GeS, and found that an exponential edge was present only in the polarization directions where excitons have been observed. The temperature dependence of the exponential edge followed Eq 1.5, and they were able to associate the energy parameter  $\hbar\omega_p$  with a phonon mode which could not produce an strong electric field. These results seem to discount the DR model because it would be difficult to find a source for the microfields that would lead to an anisotropic absorption edge. Crystalline Se and GSe are other materials which have exponential edges only in the polarization directions where excitons are found.

In support of the DR model, Mohler and Thomas [30] have measured the displacement of the absorption edge in CuCl and TiCl crystals when they are placed

in a large external electric field. The DR and ST models lead to very different field dependences for the absorption level shift  $\Delta\alpha/\alpha$ . Mohler and Thomas determined the relation between the field and temperature dependence of the steepness parameter  $\sigma$ , and their results agreed well the predictions of the DR model. Additional support for the DR model can be found in experiments with doped semiconductors; by adding a large concentration of charged impurities extrinsic Urbach edges have been produced.

Among disordered materials, Bell and Cutler [31] have successfully applied the DR model to liquid Se-Tl alloys to explain the temperature and concentration dependence of the absorption. The electric field dependence of the edge in several amorphous solids has also been measured, but the results are inconclusive at present. The DR model predicts a decrease in the slope of the edge as the field is increased. A decrease in slope has been measured in some materials, but in amorphous  $\text{As}_2\text{Se}_3$ , for example, the slope remains constant, and in amorphous Se the slope increases [1].

In the end, it might be concluded that the prevalence of Urbach behavior is the result of some type of universality among the different absorption processes which could lead to an exponential absorption edge, rather than there being a single absorption mechanism operating in many different materials.

### 1.3 Semiconductor - Semimetal Transition in Se-Te Alloys

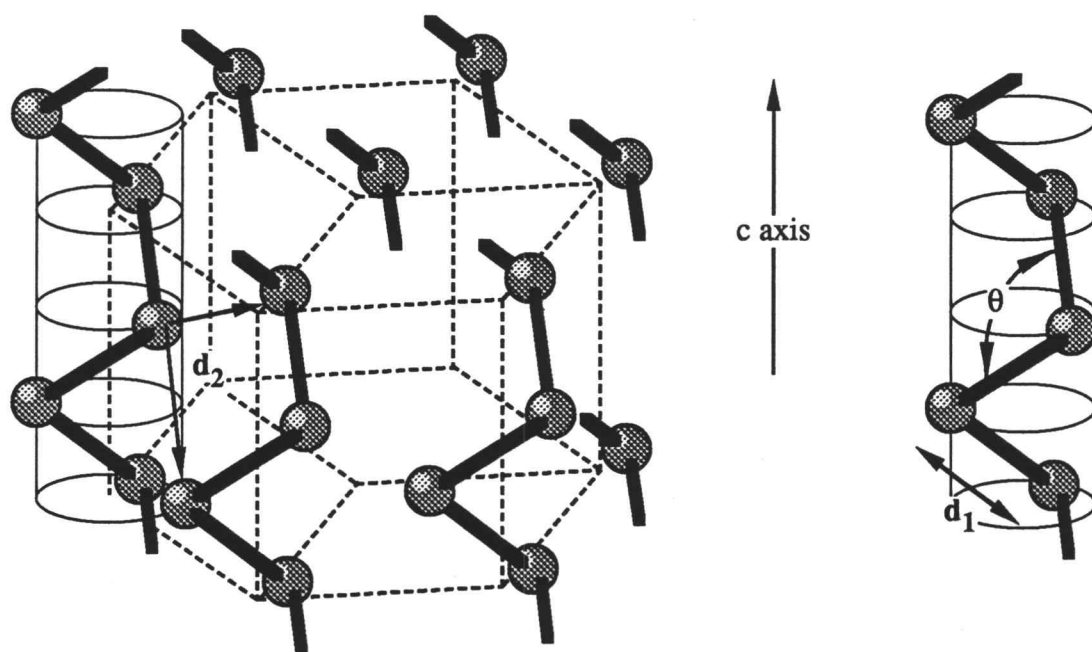
#### 1.3.1 From Order to Disorder

Before discussing the experimental evidence for a semiconductor - semimetal transition in liquid Se-Te alloys it is useful to first look at the crystalline

forms of pure Se and Te to see what changes occur in going to the amorphous solid and then liquid forms. The crystal structure of most interest here is the trigonal form of Se and Te sketched in Fig 1.5. In the trigonal lattice, each atom is covalently bonded to its two nearest neighbors to form chains parallel to the c-axis of the crystal. These chains are held together in the liquid by weaker *inter* chain covalent bonds as well as forces of the Van der Waals type. Values for the interchain and intrachain bonding distances and the bonding angles are also given in the figure. It is worth noting that the ratio of the inter to intra chain bonding distances  $d_2/d_1$  is smaller for Te than for Se; this suggests that the strength of covalent bonding between adjacent chains is larger for Te. The structure of these crystals can be understood by examining a single chain from a molecular orbital point of view. The valence shells of atomic Se and Te are  $4s^2 4p^4$  and  $5s^2 5p^4$ , respectively, and the orbitals responsible for covalent bonding are primarily of p character. Two p orbitals on adjacent atoms form directed bonding  $\sigma$  and antibonding  $\sigma^*$  energy states, leaving a nonbonding  $\pi$  state at each atomic site. Each atom has two of its  $p^4$  electrons in bonding states, two in nonbonding states, and the antibonding states are empty. If the molecular orbitals were of pure p character the bond angles would be  $90^\circ$ , but there is a small amount of hybridization of these levels with the nearest s and d orbitals, which accounts for the larger bond angle and the weak covalent bonding between chains. The crystal band states formed by the  $\sigma$ ,  $\pi$ , and  $\sigma^*$  molecular levels can clearly be seen in the the band structure calculated by Joannopoulos *et al* [32], shown in Fig 1.6. The  $\pi$  states form the valence band and the  $\sigma^*$  states form the conduction band. The optical band gap between these states is 1.9eV in Se and 0.32eV in Te.

Amorphous Se and Te can readily be prepared by vacuum evaporation or sputtering. The details of the structure in these samples depends somewhat on the





	First Neighbor d1 (Å)	Second Neighbor d2 (Å)	Ratio d2/d1	Bond Angle $\theta$
Se	2.37	3.43	1.45	103°
Te	2.88	3.45	1.20	101°

**Fig 1.5** The crystal structure of trigonal selenium and tellurium.

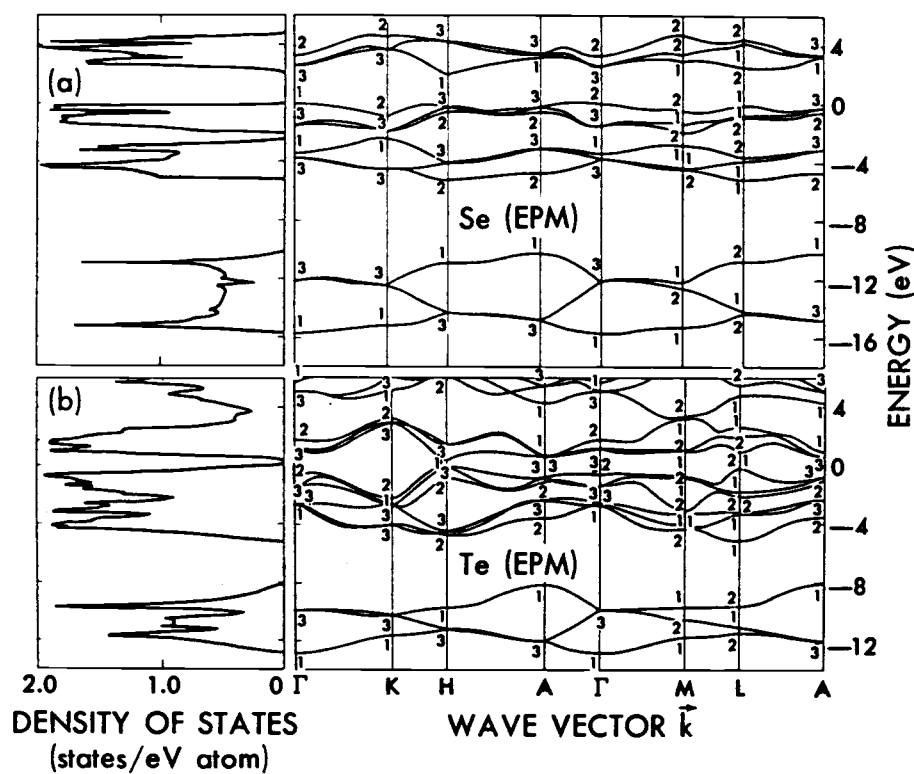


Fig 1.6 The band structure and density of states in trigonal Se and Te.

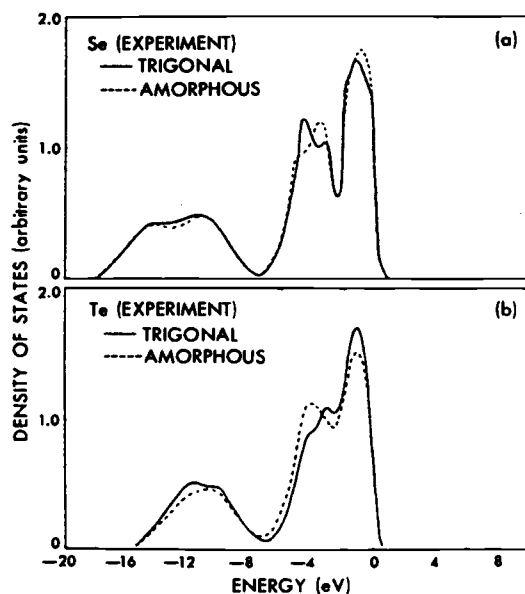
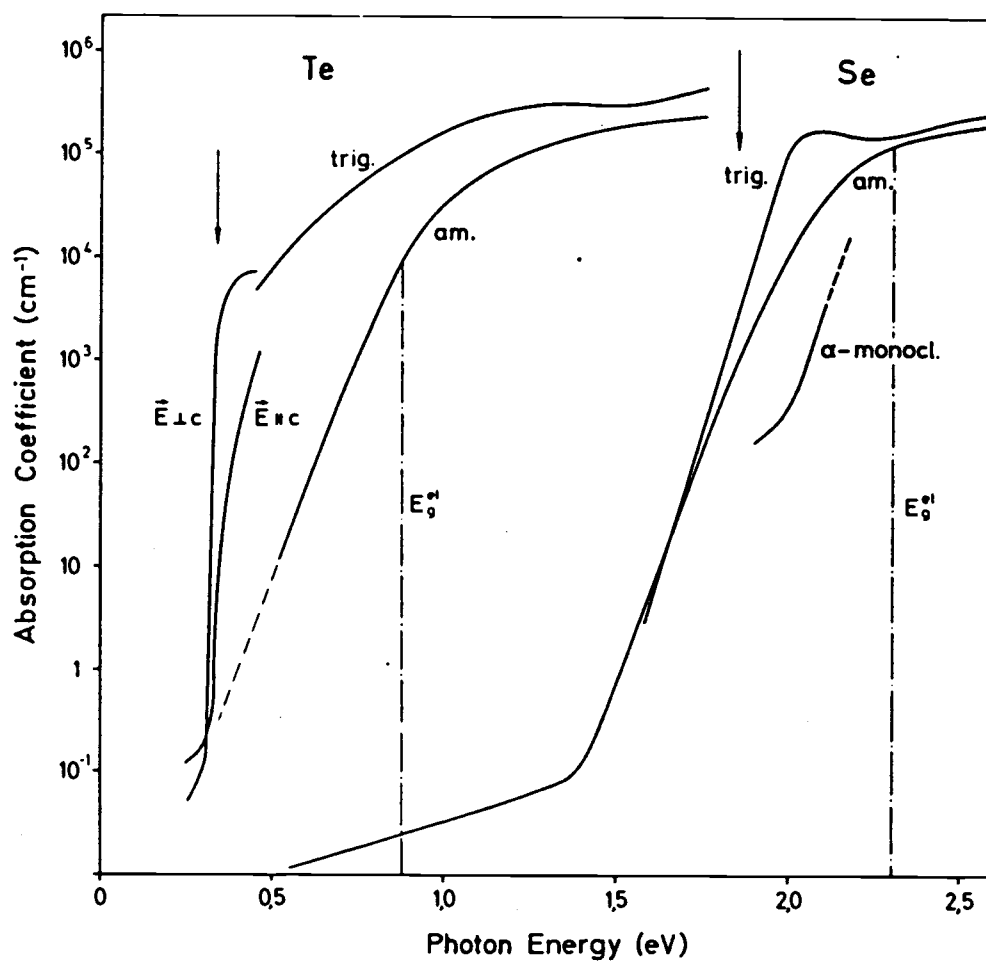


Fig 1.7 (a) X-ray and UV photoemission results on trigonal (solid line) and amorphous (dashed line) Se. (b) X-ray photoemission results on trigonal (solid line) and amorphous (dashed line) Te. [Reference 32]

preparation conditions, but it has been determined that both elements are present in the form of chains in the amorphous solid, much like the c axis chains in the crystal, and in the case of Se there also seems to be a substantial number of closed ring structures. Diffraction measurements show that the average number of atoms per chain in amorphous Te is of order 10, while in Se the chains are much longer,  $\sim 10^4$  atoms. The electron densities of state in amorphous and trigonal Se and Te, determined by X-ray and UV photoemission spectroscopy, are compared in Fig 1.7. The close similarity between the amorphous and trigonal density of states is due to the preservation of local bonding order in the disordered material. There is a change in the relative positions of the conduction and valence band edges, however, which can be seen in the optical absorption data of Fig 1.8 by the shift in the absorption curves to higher photon energies. In the trigonal crystal the band gap is in the vicinity of the H point in reciprocal lattice space. Interchain bonding contributes to the electron states in this region, and it has been suggested that a decrease in the interchain interactions in the amorphous phase is responsible for the widening of the band gap. Experimental support for this explanation is found in the optical absorption measurements of Bogomolow *et al* on separated Se and Te chains trapped in the channels of a mordinite dielectric crystal [34]. They found that the fundamental absorption bands in these samples were shifted with respect to the trigonal spectra by an amount comparable to the shift in the amorphous films.

The final step on the path of disorder from the crystal is the liquid state. Upon melting Se still retains the long molecular chain structure found in the amorphous films. The chains are shorter,  $\sim 10^3$  atoms in length, and bonding defects in the form of chain ends and three-fold coordinated chain branches begin to play a significant role in determining the electronic properties of the material. Liquid Se is still a semiconductor with an optical band gap close to that of the



**Fig 1.8** Optical absorption edges in amorphous and crystalline selenium and tellurium. The data are for room temperature, except for amorphous Te, which was cooled to ~77K to prevent crystallization. [Reference 33]

amorphous solid. Liquid Te, on the other hand, is no longer a semiconductor. Its conductivity is  $1700 \Omega^{-1}\text{cm}^{-1}$  at the melting point and rises slowly with temperature, and the thermopower is very small,  $\sim 30 \mu\text{V}/^\circ\text{C}$ . These are characteristics of a poor metal-- in this paper liquid Te will be referred to as a semimetal. The differences in the conductivity, thermopower, and other properties of Te between the solid and liquid phases has led many researchers to conclude that there is also a difference in the local bonding structure of the atoms. This is still a current topic of discussion, and a review of the relevant facts is best done in the framework of the liquid semiconductor to semimetal transition of Se-Te alloys, which is given in the next subsection.

### 1.3.2 The Semiconductor to Semimetal Transition

Liquid alloys of Se in Te are fully miscible at all temperatures and concentrations. A wide range of studies has been performed on this system using temperature, composition and pressure as variables. For the most part, the measurements can be placed into three categories: 1) electronic-- conductivity, thermopower, magnetic susceptibility, optical absorption and reflectivity [35-37,17], 2) thermodynamic-- density, adiabatic compressibility, specific heat [38-40], and 3) structural-- neutron diffraction, Xray diffraction, and Raman scattering [41-43]. In each of these measurements there are characteristic features in the data which can be associated with the behavior of pure Se and Te, which will be referred to here as phase I and phase II. It is found that a transition from phase I to phase II behavior can be brought about by increasing the Te concentration, temperature, or pressure. The transitions in the electronic, thermodynamic, and structural properties all are well coordinated in terms of these variables, which leads to the conclusion that they are different aspects of a single

transformation taking place in the liquid. The phase I to phase II transition has been termed a 'semiconductor to metal' transition because of the changes in the electronic behavior. For example, the conductivity in phase I increases with temperature with a constant activation energy, then across the transition it levels and becomes weakly temperature dependent; the behavior of the magnetic susceptibility changes from one following the Curie law to Pauli paramagnetism; and the optical reflectivity shows signs of a free carrier component in the infrared. Among the thermodynamic parameters measured, the volume per atom decreases across the transition, and at the same time the adiabatic compressibility reaches a maximum and then decreases. These factors indicate that the liquid makes a transition to a denser, more tightly bound structure in phase II.

Several diffraction and optical scattering experiments have been undertaken with the aim of determining the structural form of the liquid in phase II. The discussion given here is directed toward the changes that occur near the melting point at normal pressures by changing the Te concentration. On the phase I side of the transition the situation is fairly clear: the local bond structure and electronic structure of liquid Se are similar to those of amorphous Se. The electron density of states  $N(E)$  is shown schematically in Fig 1.9a. The presence of bond defects the form of chain ends and branches is thought to add additional electronic states in the liquid. These defects produce acceptor states above the valence edge and donor states below the conduction edge, and their presence is indicated in the figure. As the Te concentration is increased from  $x=0$  to  $x=70$ , the Te atoms tend to place themselves substitutionally into the chain structure. The average chain length decreases and the gap between the  $\pi$  and  $\sigma^*$  states also decreases. The semiconductor to semimetal transition occurs in the vicinity of the composition  $\text{Se}_{20}\text{Te}_{80}$ . Two models have been proposed to explain what happens in the

transition region. One point of view is based on theoretical work done by Cabane and Freidel [44] on the structure of liquid Te. They used the neutron diffraction data of Tourand and Breuil [45], which indicated that the number of atoms in the first coordination sphere of liquid Te increased from 2.5 at the melting point to 3.0 at temperatures above 800°C, as the basis of a model where the 2-fold bonded chains were replaced by a 3-fold bonded network of atoms similar to the structure of amorphous arsenic. As the transformation proceeds, the chains become cross-linked by 3-fold sites, and electrons in the nonbonding  $\pi$  band are transferred to  $\sigma$  and  $\sigma^*$  energy levels. The final form of the density of states leaves a  $\sigma^*$  band that is roughly 1/3 full, which accounts for the metal-like properties of the liquid. The greater degree of local bonding in a 3-fold coordinated structure also explains the measured increase in the density of the liquid and the decrease in its compressibility. The electronic transformation predicted by this model is illustrated in Fig 1.9b. A different model for the semiconductor-semimetal transition proposed by Cutler [35,46,53] retains the local 2-fold bonding through the transition region. In his model, as the average chain length decreases the number of acceptor states increases to the point that they form a band which gradually merges into the valence band edge. This produces a large density of hole states in the valence band of the liquid. The transition is shown in Fig 1.9c. For each broken bond there are two less bonding and antibonding levels in the density of states, and two electron states and two hole states added to the valence band. This model requires a positive value for the thermopower of phase II, which is in agreement with experiment, and contrary to what would be expected for the partially filled conduction band in the previous model. The weakness here is that it is more difficult to reconcile 2-fold atomic bonding with the neutron diffraction data for the first coordination sphere. It is also necessary to introduce an additional interchain

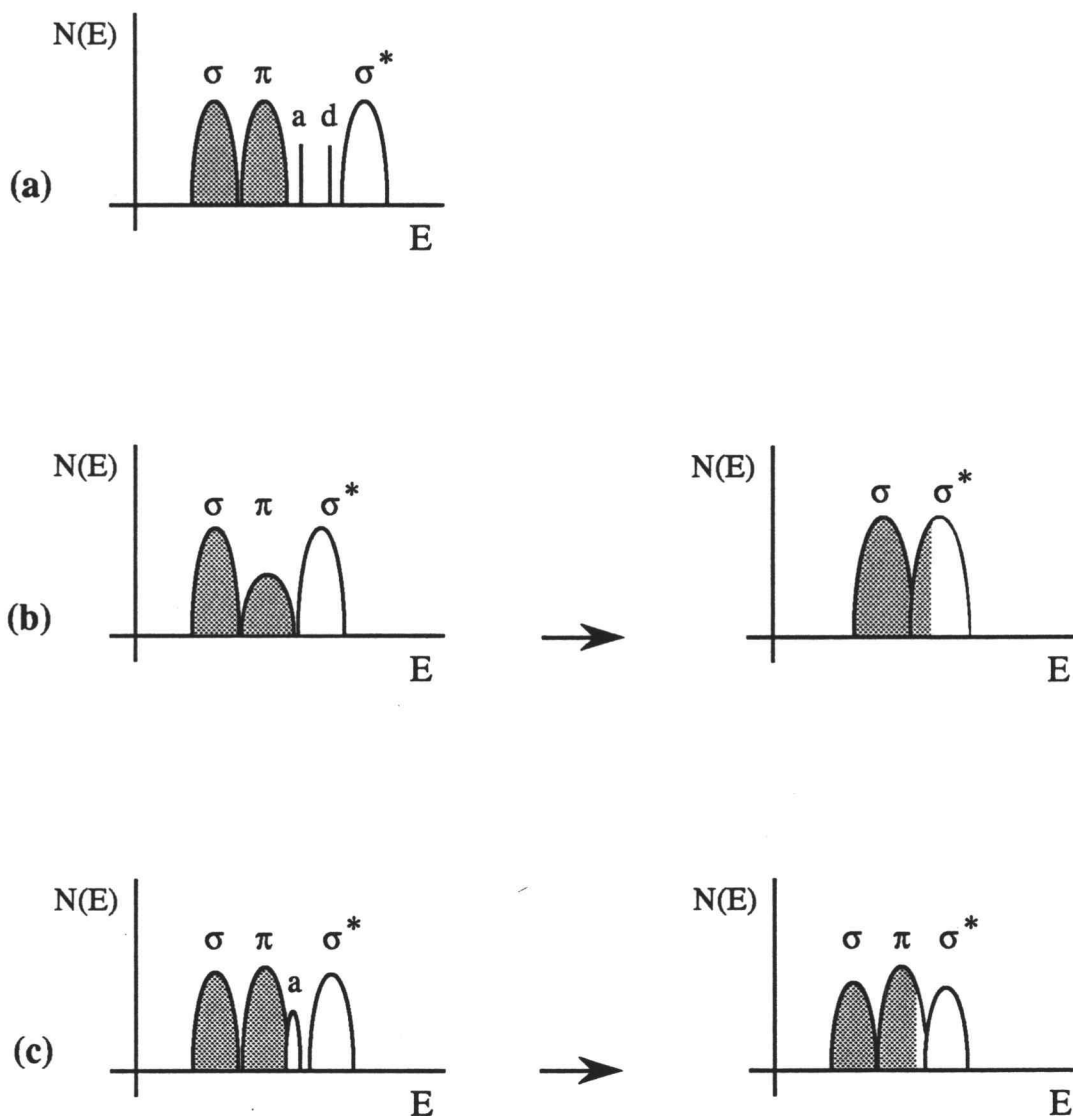


**Fig 1.9** (a) A schematic view of the density of states structure in liquid Se. As the Te concentration is increased the gap between  $\pi$  and  $\sigma^*$  states decreases. (b) Electronic transition proposed by Cabane and Freidel. The  $\pi$  band is depleted as 3-fold bonds form, producing a partially filled  $\sigma^*$  band. (c) Electronic transition proposed by Cutler. As the concentration of broken bonds increases the acceptor states form a band which merges with the top of the valence band.



interaction of some sort to explain the changes in the thermodynamic properties of the liquid.

The two models outlined above are quite different. In the first case the density of states in the  $\sigma$  and  $\sigma^*$  bands increases at the expense of the nonbonding  $\pi$  band, and in the second case the reverse happens. The main support for the arsenic-like structure has been the data from early diffraction experiments, but a review of more recent diffraction measurements has shown that these results are in error [47,48]. The most significant conclusion reached concerning the radial distribution data is that there is a substantial penetration of the first coordination shell by nonbonded Te atoms. Welland *et al* [48] have suggested that nonbonded Te atoms may even contribute to the height of the radial distribution curve at distances closer than the first coordination peak. The result of taking this factor into consideration is that the average number of bonds per atom deduced from diffraction measurements falls to values closer to 2, which is much more in accord with the phase II model of Cutler.

#### 1.4 Objectives of this Work

Measuring the optical dispersion of a material is a time-honored technique for probing the electronic structure. In the past, the only means available for measuring the optical behavior of liquid semiconductors in the fundamental absorption band has been through the reflectivity of the liquid. But this is not necessarily the best way to do the measurement. There is always the question of whether the surface properties of the liquid are the same as those in the interior volume. Results obtained from reflectivity measurements also have limited resolution because a proper analysis of the data involves the use of fitting functions with many adjustable parameters, and there is always some uncertainty in

assigning their values. The first objective of this work is to show that it is possible to prepare liquid samples in a form which allows the transmissivity to be measured in the spectral region where interband electronic transitions take place. This makes it possible to probe the electronic structure of the liquid volume (as opposed to the surface) directly by determining the absorption coefficient.

The second objective of this work is to see if information derived from the optical dispersion of Se-Te alloys may help determine whether the electronic transition in the liquid is also accompanied by a change in the local bonding of the atoms. The two proposed mechanisms for the transition outlined in section 1.2 suggest significantly different changes in the valence and conduction bands, and would be expected to produce very different changes in the optical behavior.

## 2. The Optical Measurements

### 2.1 Optical Measurements on Thin Film Samples

#### 2.1.1 Film Preparation

An account of the methods used to prepare the film samples has already been presented in another paper, a copy of which has been included as an appendix to this work. Only a brief description will be given here. Two techniques were used to prepare the liquid films: one is referred to as the thin film evaporation technique, the other is called the compressed liquid technique. The thin film evaporation technique involves sandwiching a vacuum evaporated sample film and a surrounding evaporated gasket between two optical windows, and then melting the sample to obtain a liquid film. The composition of the alloy was controlled by measuring the thicknesses of the evaporated films with a quartz crystal microbalance. This technique was used to measure the optical properties of Se,  $\text{Se}_{80}\text{Te}_{20}$ , and  $\text{Se}_{60}\text{Te}_{40}$  ( $\text{Se}_{60}\text{Te}_{40}$  at  $350^\circ\text{C}$  only) in the spectral region where the absorption coefficient of the liquid  $\alpha$  was above  $10^3 \text{ cm}^{-1}$ . Measurements on the other alloys, and measurements for  $\alpha$  less than  $10^3 \text{ cm}^{-1}$  were performed on samples prepared by the compressed liquid technique. In this case the liquid film was formed by compressing a small melted piece of a previously made alloy in a cavity between fused quartz windows. The cavity thickness for the thick films ( $\sim 10\mu\text{m}$ ) was set by the thickness of a metal foil gasket. For the submicron sized films the cavity thickness was set by the depth of an etched depression in one of the quartz windows.

#### 2.1.2 Reflectivity and Transmissivity Measurements

The spectrometer used to measure the reflectance and transmittance of the films is shown in Fig 2.1. A dual light source consisting of a quartz-halogen lamp and a xenon arc lamp was used to cover the spectral range of 0.4eV to 5.0eV. This

light was filtered by an Oriel model 77276 dual monochromator and a complementary set of long wavelength pass-filters. It was necessary to use a dual rather than a single monochromator because it was found that at very high absorption levels in the film the specular background radiation from a single monochromator passed through the sample with a higher intensity than the primary wavelength being measured. The light was focused into a beam by a pair of mirrors and then chopped so the signals could be amplified and detected synchronously by lock-in amplifiers. A small portion of the chopped beam was directed to detector D1, which was used to keep track of intensity variations in the light source; the rest of the beam passed through an aperture stop and beam splitter, and then reached the sample cell. The reflected light intensity was measured by detectors D2 and D3. The transmitted light passed through a second aperture stop before it was detected by D4 and D5. The purpose of the exit aperture stop was to decrease the amount of oven-produced IR radiation that reached the detector for the transmitted light. The detector gain, especially for the PbS photoconductor, was affected by changes in the background IR intensity level. For photon energies with a sample transmissivity greater than  $10^{-4}$ , detector D5 was used. The photomultiplier D4 was used at visible and UV energies to measure transmissivities less than  $10^{-4}$ .

The signals produced by D2-D5 were proportional to the reflectivity and transmissivity of the optical cell. These measurements were calibrated against the reflectivity and transmissivity of an empty sample cell using the known refractive index of fused quartz. The neutral density filter shown in front of the photomultiplier in Fig 2.1 was used to attenuate the transmitted light intensity during the calibration measurements.

# Apparatus for Measuring Film Reflectance and Transmittance

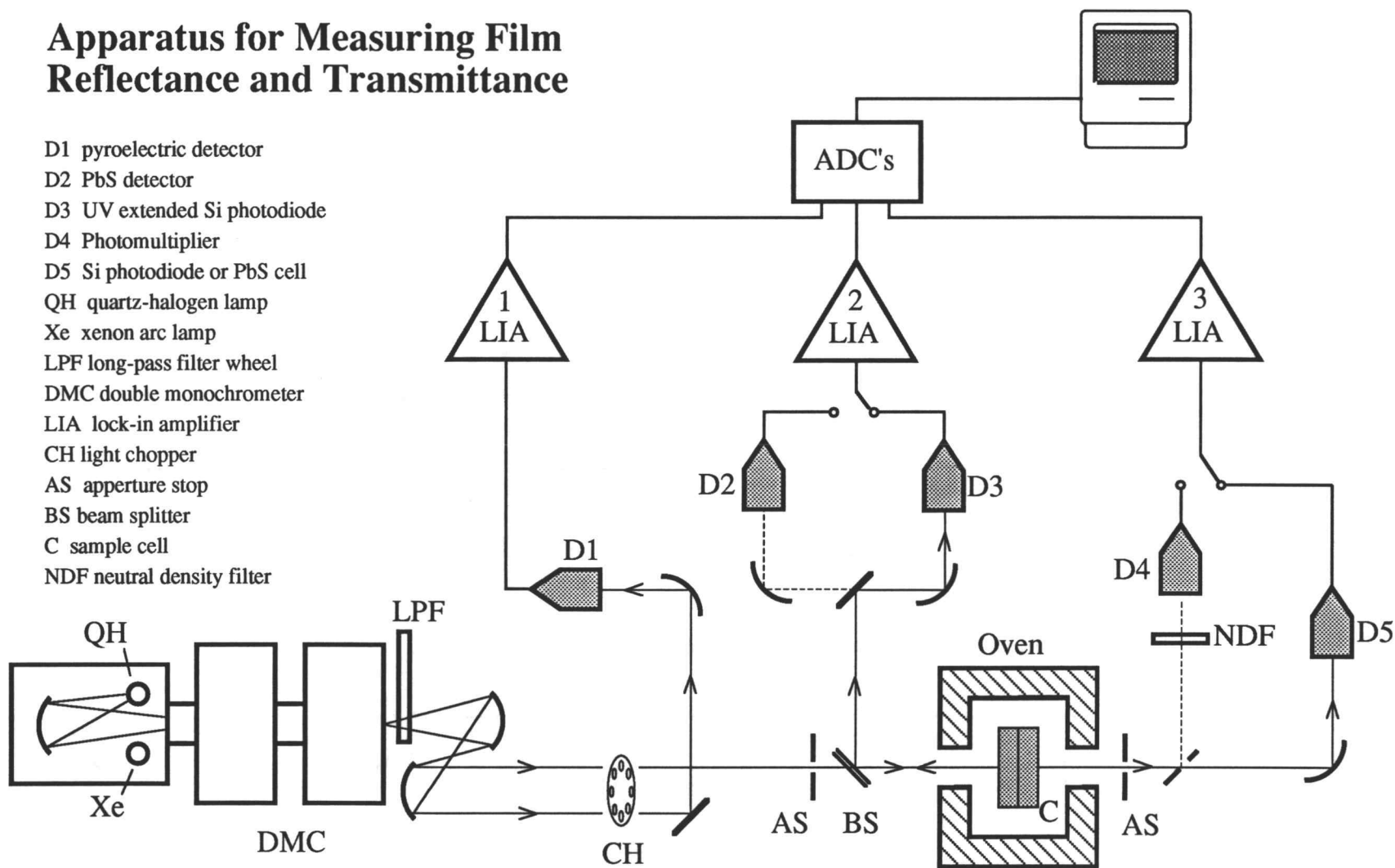


**Fig 2.1** Apparatus for measuring film reflectance and transmittance.

### 2.1.3 Cell Measurements and the Refractive Index of the Liquid

The data produced directly by the spectrometer gives the reflectance and transmittance of the optical cell ( $R_{\text{cell}}, T_{\text{cell}}$ ), which is the reflectance and transmittance of the liquid film ( $R_{\text{film}}, T_{\text{film}}$ ) modified by the additional reflections at the window-air interfaces. The reflectivity of a quartz-air interface is small, about 4%, and the multiple reflections this produces within the optical cell can easily be separated from  $R_{\text{cell}}, T_{\text{cell}}$  to find  $R_{\text{film}}, T_{\text{film}}$ . An example of the results obtained for liquid selenium at 250°C is shown in Fig 2 in the appendix. The next step in the data reduction process is to invert the data for  $R_{\text{film}}, T_{\text{film}}$  to find the complex index of refraction  $n + ik$  of the liquid. A diagram illustrating the physical problem is shown in Fig 2.2. The most general relation between  $R, T$  and  $n, k$  is [50]

$$T_{\text{film}} = tt^* = \left[ \frac{(1 - r^2)e^{-i(\delta - i\beta)}}{1 - r^2e^{-2i(\delta - i\beta)}} \right] * \infty \quad (2.1)$$

$$R_{\text{film}} = rr^* = \left\{ -r + \left[ \frac{r(1 - r^2)e^{-2i(\delta - i\beta)}}{1 - r^2e^{-2i(\delta - i\beta)}} \right] \right\} * \infty \quad (2.2)$$

where  $t$  and  $r$  are the amplitude transmittance and reflectance of the film, which contain the factors

$d$  : the film thickness

$n_0$  : the refractive index of the windows

$E = \hbar\omega$  : the photon energy

$\delta = \frac{2\pi E}{hc}nd$  real phase factor

$\beta = \frac{2\pi E}{hc}kd$  amplitude attenuation coefficient

$r = \frac{n_0 - (n + ik)}{n_0 + (n + ik)}$  Fresnel reflection coefficient

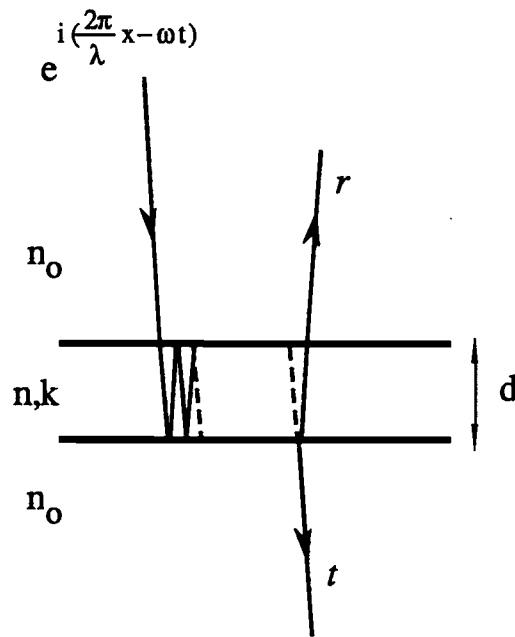


**Fig. 2.2** Monochromatic light in a media with index  $n_o$  is incident normally on an absorptive film with a refractive index  $n+ik$  and thickness  $d$ . Interference occurs in the film, resulting in a total amplitude reflectance  $r$  and amplitude transmittance  $t$  for the film.

The expressions for  $tt^*$  and  $rr^*$  can be expanded into functions of only real variables, of course, but the results are too long and complicated to be of any use here. The end result of the expansion is that  $R_{\text{film}}$  and  $T_{\text{film}}$  are found to be transcendental functions of the sample parameters  $n$ ,  $k$ , and  $d$ . These functions are multivalued: a given pair of values for the reflectance and transmittance measured at single wavelength do not correspond to a unique set of numbers for  $n$ ,  $k$  and  $d$ . In this experiment it was necessary to determine the thickness of the film before proceeding to find  $n$  and  $k$ . The methods used to do this are described next.

#### 2.1.4 Determining the Film Thickness

In the spectral region where  $k$  is small Eqs 2.1 and 2.2 reduce to a much more tractable form:

$$T_{\text{film}} = \frac{8n^2n_o^2}{(n_o^2 + n^2)^2 + 4n^2n_o^2 - (n_o^2 - n^2)^2 \cos\left(\frac{4\pi E}{hc}nd\right)} \quad (2.3)$$

$$R_{\text{film}} = \frac{(n_o^2 + n^2)^2 - 4n^2n_o^2 - (n_o^2 - n^2)^2 \cos\left(\frac{4\pi E}{hc}nd\right)}{(n_o^2 + n^2)^2 + 4n^2n_o^2 - (n_o^2 - n^2)^2 \cos\left(\frac{4\pi E}{hc}nd\right)} \quad (2.4)$$

These are just the equations for the reflectance and transmittance of a transparent film, with the usual sinusoidal-like dependence on photon energy. The conditions for the maxima and minima in the reflectivity (and conversely for the transmissivity) are given by

$$\text{maxima} \quad nd = (2m - 1)\frac{hc}{4E} \quad m = 1, 2, 3, \dots$$

$$\text{minima} \quad nd = l\frac{hc}{2E} \quad l = 0, 1, 2, 3, \dots$$



$R_{\text{film}}$  and  $T_{\text{film}}$  can now be considered to be functions of two new variables: the product  $nd \equiv P$  which appears as a phase factor in the cosine terms, and the real index of the liquid  $n$ .  $P$  determines the locations of the maxima and minima, and the magnitude of  $n$  determines the heights of the reflection peaks. As long as  $n$  is a slowly varying function of energy the thickness of the film can be determined by finding the values of  $P$  and  $n$  which best fit a given interference peak. The thickness is then  $d = P/n$ . In this experiment the phase factors were first estimated by finding the series of integers for  $m$  and  $l$  which fit the measured energy positions of the reflectance extrema. The reflectivity data were used to do this instead of the transmissivity data because the reflectivity is damped less rapidly by increasing values of  $k$ . The final values for  $n$  and  $P$  were taken from a least-squares fit of Eq 2.4 to each of the peaks in the reflectivity spectrum, and the thickness of the film was taken to be the average of the values thus obtained.

The procedure outlined above worked very well for liquid Se and the alloy  $\text{Se}_{80}\text{Te}_{20}$ , which both had a large transparent energy range in the IR. The band gap of the alloys decreases rapidly as the Te concentration is increased, however, and the available transparent range of energy diminishes. In the case of  $\text{Se}_{60}\text{Te}_{40}$  the extinction coefficient could no longer be considered negligible at the longest wavelengths measured, but it was still possible to determine the film thickness from the interference features in an iterative fashion-- first estimating the thickness to get approximate values for  $k$ , and then using these results to improve on the calculated value of  $d$ . For the alloys containing more than 40% Te there were no distinct interference features present in any of the measurements and an indirect method had to be used to find  $d$ . The thicknesses of the films containing  $\text{Se}_{40}\text{Te}_{60}$  and  $\text{Se}_{20}\text{Te}_{80}$  were measured after they had solidified with a Dektak surface profilometer. For the pure tellurium films  $d$  was determined by using the

mass of the sample, its density, and the final surface area of the film. The accuracy of the film thickness measurements using the various methods outlined above is discussed later in section 2.3.

#### 2.1.5 Calculating the Refractive Index of the Liquid

Once the film thickness is determined Eqs 2.1 and 2.2 can be solved numerically to find the values of  $n, k$  at each energy which simultaneously produce the measured values for  $R_{\text{film}}, T_{\text{film}}$ . In general the solutions to these equations are still multivalued, but in the two limits of high absorption and very low absorption the task of finding the correct values for  $n$  and  $k$  simplifies. Where the film is transparent  $k \approx 0$  and the values of  $n$  found in the thickness determination procedure serve as markers to make sure the numerical fitting routine has not strayed off course. At the other other extreme, for energies where  $T_{\text{film}} < .05$  the effects of interference are negligible, and the transmissivity and reflectivity of the film can be written as

$$T = (1 - R^2) e^{-\alpha d}$$

$$R = \left[ \frac{n_o - (n + ik)}{n_o + (n + ik)} \right]^2$$

These equations can be solved to uniquely find  $n$  and  $k$  at each energy

$$\alpha = \frac{4\pi E}{hc} k = -\frac{1}{d} \ln \left[ \frac{T}{(1 - R)^2} \right] \quad (2.5)$$

$$n = n_o \left( \frac{1 + R}{1 - R} \right) \pm \sqrt{n_o^2 \left( \frac{1 + R}{1 - R} \right)^2 - (n_o^2 + k^2)} \quad (2.6)$$

For all of the  $\text{Se}_x\text{Te}_{1-x}$  alloys the positive root in Eq 2.6 is the physically correct choice. To summarize then, the optical properties of the liquid were determined by first finding the thickness of the sample film, applying Eqs 2.5 and 2.6 to calculate

$n, k$  for transmissivities less than .05, and then using the values of  $n, k$  at  $T_{\text{film}} = .05$  as starting values in an iterative numerical solution to Eqs 2.1 and 2.2 for the rest of the measurements.

## 2.2 Reflectivity Measurements

In principle, the values of the complex index of refraction derived from the thin film measurements are complete and no additional measurements are necessary. In practice, however, it was found that there was a small problem due to inconsistent reflectivity values from sample to sample. A partial explanation for this is that the sample surface areas were very small, typically  $5\text{mm}^2$ , so the power in the reflected beam was also very small and prone to inaccuracies. But the largest source of the error seems to have been alignment differences of the optical cell between the liquid film measurements and the empty cell calibration. Any tilting of the windows focuses the reflected light onto a different spot on the detector, producing a proportional change in the signal voltage.

To improve the accuracy of the thin film results, a separate set of reflectivity measurements was undertaken. The configuration of the sample cell used in these measurements is similar to that used in the thin film work, except the surface area of the liquid was much larger ( $\sim 1\text{cm}^2$ ). A diagram of the cell and clamp is shown in Fig 2.3. The sample was prepared by placing weighed amounts of Se and Te into the quartz cell-- enough to produce a 3-4 mm liquid film-- and then setting the cell into its clamp with the screws left untightened. The cell and clamp were then placed in a vacuum system and evacuated to remove the oxygen from inside the cell. The system was back-filled with argon, and the clamp tightened shut to seal the cell. Then this assembly was placed in a vertical orientation into an oven (the

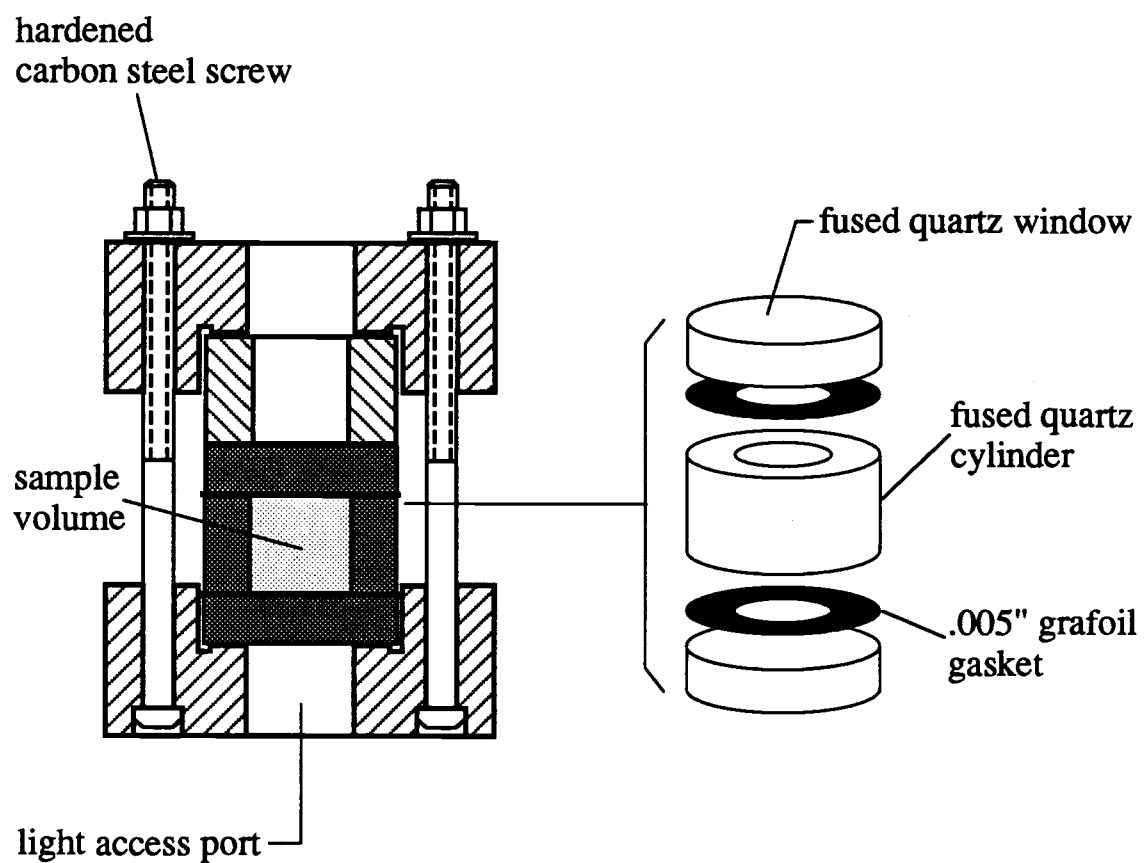


**Fig 2.3** The cell and clamp used to measure the reflectivity of the liquid. Objects are drawn on a 1:1 scale.

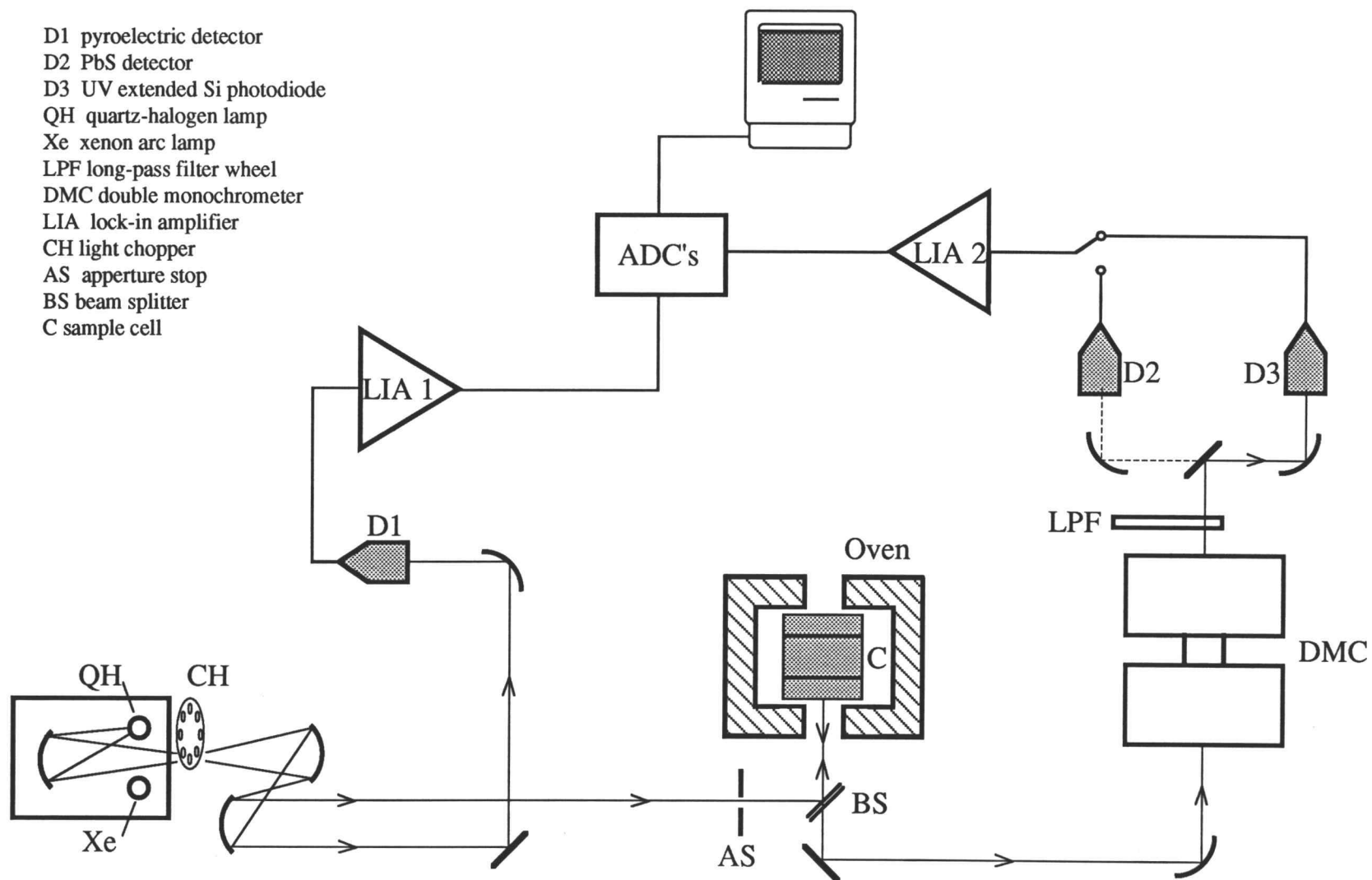


Fig 2.4 Apparatus for reflectivity measurements.

sample resting on the bottom window) and heated to a temperature 100°C above the melting point of the alloy.

A layer of impurities, probably tellurium oxide, always formed on the surface of the liquid. In order to produce a clean quartz-liquid interface for the reflectivity measurements the oven was designed so that it could be rotated 180° in a vertical plane. This allowed a clean layer of the liquid to flow across the opposite quartz window, and it was this liquid-window interface which was measured. It was important to heat the liquid to a temperature at least 100°C above the melting point, not only to facilitate complete mixing of the alloy, but also to prevent the formation of surface irregularities in the layer of liquid in contact with the quartz window.

The equipment used to measure the reflectivity is shown in Fig 2.4. The main difference between this arrangement and the one shown in Fig 2.1 is that the light is dispersed by the monochromator after it has been reflected from the sample, instead of before. This approach has the advantage of dispersing the oven IR inside the monochromator along with the primary light beam, thus greatly reducing the background radiation seen by the detector. The liquid reflectivity measurements were all calibrated against the reflectivity of a single fused quartz window.

### 2.3 Errors and Uncertainties

The data obtained in this experiment are believed to accurately reflect the basic trends in the optical behavior of Se-Te liquids as the temperature and composition are varied. Still, there are several sources of systematic error which limit their absolute accuracy. The errors can be attributed to three sources:

equipment limitations, variable sample conditions, and uncertainties in the film thickness. The magnitude of the effects of these errors will be discussed below.

### 2.3.1 Equipment Limitations

The electronics used to detect, amplify, and digitize the light signals were a relatively small source of error. The lock-in amplifiers had a basic linearity of  $\pm 2\%$  from scale to scale, but because of the large range of light intensities used, the nonlinearity tends to be random across all measurements. There was a considerable problem, however, with variations in the gain of the detectors due to the IR background produced by the oven-- particularly for the PbS detectors. The aperture stop on the transmission side of the oven (Fig 2.1) blocked much of the background radiation, but the gain of the PbS detector still was lowered by as much as 1/2 at the highest oven temperatures. To counter the gain changes, all of the calibration measurements were made at the same oven temperature as the sample measurements; in this way the gain decrease cancels out in the calculations. The effectiveness of this approach was tested by performing two measurements on the same sample, one with the exit aperture stop in place and one with it removed. The calibration data were taken in the same way at the same temperature, and though detector signal was quite different between the two measurements the calculated results were identical.

As mentioned in section 2.2, differences in the alignment of the optical cell between the sample measurements and the calibration measurements were also a source of inaccuracy. In the thin film experiments, cell misalignment affected the reflectivity most because any tilting of the window surfaces directed the reflected light to a different spot on the detector. The transmitted light path was not changed as much when this happened, so the transmissivities are less affected. The

variations in  $R$  from sample to sample were usually  $\approx 7\%$ , but in some cases the difference was 15%. The presence of errors in the reflectivity was very noticeable in the region of low absorption. At the locations of the interference maxima and minima, values of  $R$  which were erroneously too high or too low would cause the calculated values for  $n$  to spuriously diverge to very high or low values. The accuracy of the calculated values for  $n$  and  $k$  was improved by repeating the reflectivity measurements with an optical arrangement more suitable for the task (Fig 2.4). The sample cell and clamp were held in a way which made their position more repeatable, and the results are estimated to be correct to within  $\pm 3\%$ .

### 2.3.2 Sample Conditions

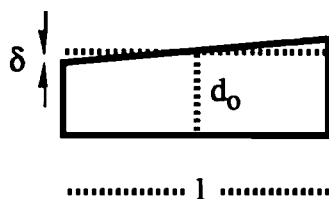
The important factors here are temperature, composition, and flatness of the film. The temperature of the liquid was determined via a thermocouple placed in contact with the outer edges of the cell windows. Tests on a mock-up cell, using this temperature probe and a separate thermocouple located at the sample's position at the center of the cell, showed that the temperature difference between these points ranged from  $0^\circ\text{C}$  to  $7^\circ\text{C}$  for oven temperatures of  $250^\circ\text{C}$  to  $500^\circ\text{C}$ . In all the film measurements this temperature difference was compensated for in setting the oven temperature. The oven temperature was generally stable to within  $\pm 1^\circ\text{C}$ , and accurate to about  $3^\circ\text{C}$ .

Though the mass determinations used to control the alloy concentrations were very precise (4 significant digits), the optical data exhibited shifts between identically prepared samples, which were interpreted as being due to compositional variations of  $\pm 3\%$ ; eg, a nominal  $\text{Se}_{60}\text{Te}_{40}$  alloy had compositional variations between  $\text{Se}_{63}\text{Te}_{37}$  and  $\text{Se}_{57}\text{Te}_{43}$ . Variations in  $x$  could clearly be seen as systematic energy shifts in the absorption edge from one sample to the next. In the



case of the 'compressed liquid' films the variations may have been due to differences in the composition of the initial ~0.3 mg solid alloy used to make the film. The same master-set of alloy materials was used throughout this experiment, so this would require fluctuations in  $x$  within the volume of the master alloys. In the case of the 'thin film evaporation' samples the variations in composition most likely were the result of some leakage of the liquid into the gasket region when the solid films were melted. Because the solid Se and Te film layers melted unevenly and at different temperatures, an excess of one component of the liquid would result if more of the other component leaked past the gasket. The results given in this paper are the average of all the measurements done at each composition.

The flatness of the films with IR transparency could be verified by looking at the interference features in the reflectivity. Another, less direct means to verify the flatness was provided by the surface profilometer scans used to determine the thickness of the film after it had solidified. In general the film thickness rarely deviated by more than 5% across the area of the film exposed to the light. The effect of this amount of distortion can be estimated by considering the transmissivity of a wedge shaped film:



$$T \propto \frac{\sinh(\alpha \delta / 2)}{(2/\alpha l \delta)} e^{-\alpha d_0}$$

For a perfectly flat film the prefactor of the exponential term in  $T$  would be unity. Using parameter values to find the largest error anticipated,  $\delta = 0.03 \mu\text{m}$ ,  $\alpha = 5 \times 10^5 \text{ cm}^{-1}$ , and  $l = 0.3 \text{ cm}$ , the prefactor increases to only 1.006. This indicates that the distortions of the film are negligible.

### 2.3.3 Film Thickness Measurements

All of the computations to derive  $n, k$  from  $R_{\text{cell}}, T_{\text{cell}}$  were done to an accuracy of 0.1%, but their overall accuracy hinges on having good values for the thicknesses of the films. An error in  $d$  directly translates to an equal error with opposite sign in  $\alpha$  and  $k$ , and also affects the calculated value of  $n$  when  $k$  is large. The interference fringe method was the most accurate means of determining the film thickness. The phase factors  $P=nd$  could be found to good precision from the IR reflectivity curves; the limitation in determining  $d$  came from the uncertainty in  $n$ . Below the band gap the real index  $n$  is completely determined by the magnitude of the reflectance. An estimate of the accuracy of  $R$  has been placed at  $\pm 3\%$ ; this figure corresponds to a smaller uncertainty in  $n$ , about  $\pm 1\%$  (see Eq 2.6). It follows that the thicknesses of the thin film samples ( $d < 3\mu\text{m}$ ) of liquid Se and  $\text{Se}_{80}\text{Te}_{20}$  are accurate to about 1%. The values of  $d$  for the  $\text{Se}_{60}\text{Te}_{40}$  thin films were less accurately determined because the films were not completely transparent in the IR, and the effect of absorption on the interference spectra had to be taken into consideration. The uncertainty in the thickness increased to  $\sim 3\%$ .

The thicknesses of the  $\text{Se}_{40}\text{Te}_{60}$  and  $\text{Se}_{20}\text{Te}_{80}$  liquid films were determined by using a surface profilometer to measure the thicknesses of the solidified sample films after the optical measurements had been completed. The accuracy of this technique is limited in part by the the accuracy of the reference standard used to calibrate the profilometer, and also by the assumption that the liquid film does not significantly distorted as it becomes solid. An accuracy of  $\pm 5\%$  seems to be a reasonable estimate in this case.

The data presented in this paper for the absorption of liquid Te were all taken from measurements on a single film sample. The first estimate of the thickness of this sample was based on a simple calculation using the density,

mass, and surface area of the film-- the assumption being that the film was flat and continuous throughout the sample volume. As it turned out, the value of  $d$  found in this way ( $.20\mu\text{m}$ ) was too small to be consistent with the reflectivity measurements. The resulting values for  $k$  were too large and produced a negative quantity under the radical in Eq 2.6. The thickness used to calculate the results given here was the minimum thickness consistent with the reflectivity measurements,  $0.24\mu\text{m}$ . Considering the uncertainty in  $R$  it is possible that the film was actually as thin as  $0.23\mu\text{m}$ , but it is very unlikely that it was more than  $.25\mu\text{m}$ .

As a final note, the thicknesses of the films used to measure the exponential edge ( $12\mu\text{m} < d < 25\mu\text{m}$ ) for Se,  $\text{Se}_{80}\text{Te}_{20}$ , and  $\text{Se}_{60}\text{Te}_{40}$  were found by matching the absorption coefficient curves with the thin film results in the energy range where they overlapped. This was more accurate than using the thickness of the metal foil gasket for  $d$ .

### 3. Presentation of Results

#### 3.1 Reflectivity

Fig 3.1 shows a representative set of curves for the reflectivity of a fused quartz--liquid  $\text{Se}_x\text{Te}_{1-x}$  interface as a function of composition and moderate temperature changes. Several of the characteristics of the Se-Te system can be seen by examining the reflectivity data by itself. Starting with pure selenium,  $R$  is fairly flat in the infrared spectrum up to about 1.5eV, and then it rises to a higher plateau above 2eV. This change is characteristic of a semiconductor with a large energy gap-- in this case ~2eV. The reflectivity is relatively constant at higher photon energies up to 4.5 eV, where it then begins to dip downward. As increasing amounts of tellurium are added to the liquid the reflectivity rises and the band gap decreases. The red shift of the band gap can be seen clearly in the alloys containing 20% to 60% Te by the shift in the rising edge of the reflectivity curve to lower energies. But then there is a noticeable change in the optical behavior between 60% Te and 80% Te. Below 1eV the reflectivity of liquid Te, and liquid  $\text{Se}_{20}\text{Te}_{80}$  at higher temperatures, takes on the characteristics expected when a large number of free charge carriers are present. Materials with comparable optical behavior are heavily doped semiconductor crystals. The reflectivity is high in the IR at frequencies below the plasma frequency of the carriers, and gradually decreases at higher frequencies. In chapter 5 it will be shown that the free carriers responsible for the IR reflectivity of Te are holes appearing in the valence band.

The reflectivities shown in Fig 3.1 are qualitatively the same as those reported by Seyer *et al* [16], who also measured the reflectance of the liquid behind a quartz window. The differences between their results and those given here are mostly a matter of small shifts in magnitude, but the indicated changes produced by

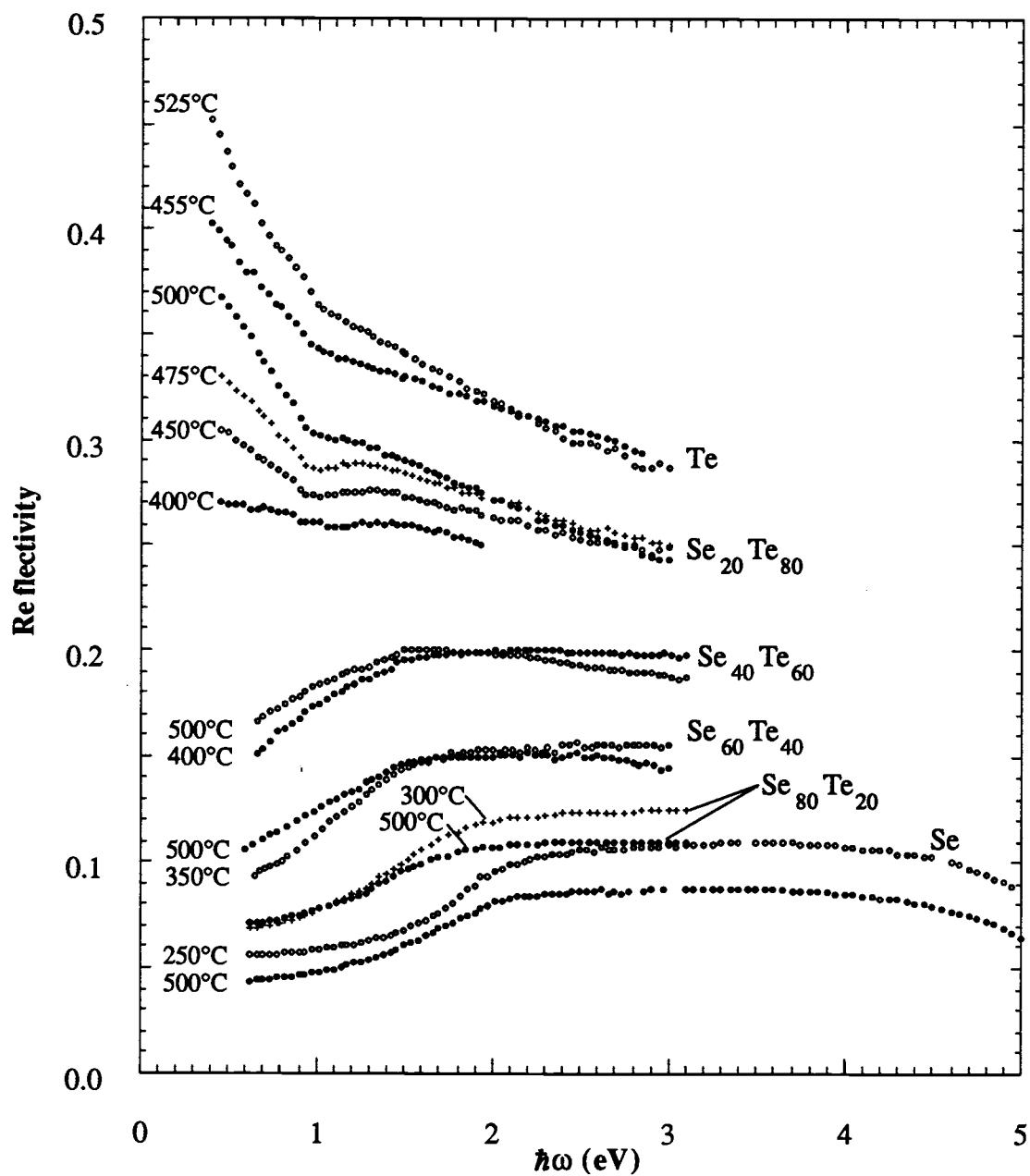


Fig 3.1 A representative set of curves for the reflectivity of Se-Te liquids.

temperature and composition variations are identical. Seyer *et al* measured the reflectivity of alloys containing up to 70% Te over a wide range of temperatures and pressure, and found that the transition to free carrier behavior in the infrared could be produced in all of the alloys within their accessible range of temperature and pressure. As  $x$  was increased the temperatures and pressures required to reach the transition point also increased. Fainchstein and Thompson [17] have also measured the reflectivity of the liquid Se-Te system; their results are for a liquid-sapphire interface at normal pressures. A notable feature which appears in all their reflectivity curves is a sharp rise in  $R$  between 1eV and 0.6eV. This increase is not seen in the results presented here except at high Te concentrations, and it seems most likely that it is due to a systematic error in their measurements. A large increase in the reflectivity is usually associated with an increase in optical absorption, but the absorption coefficient actually decreases in this energy region.

### 3.2 Absorption Coefficient above the Band Gap

The absorption coefficient  $\alpha$  gives information about the position of the band gap of the liquid, and can also be used to look for changes in the shape of the conduction and valence band density of states. Two views of  $\alpha(\hbar\omega)$  are given in Figs 3.2 and 3.3. The most striking feature seen in these data is the linear behavior of  $\alpha$ , which in the case of liquid Se extends nearly 1.5eV above the band gap. At a fixed temperature, the slope of  $\alpha$  slowly increases as  $x$  is decreased from 1 to 0.4. As in the case of the reflectivity, the alloy  $\text{Se}_{20}\text{Te}_{80}$  is a pivotal composition. The absorption begins to rise more rapidly at lower photon energies in the 450°C curve, which lowers the slope, and the temperature dependence of  $\alpha$  becomes very large. Liquid  $\text{Se}_{20}\text{Te}_{80}$  still appears to be a semiconductor in that extrapolating the absorption curves to zero  $\alpha$  still gives a positive energy gap.

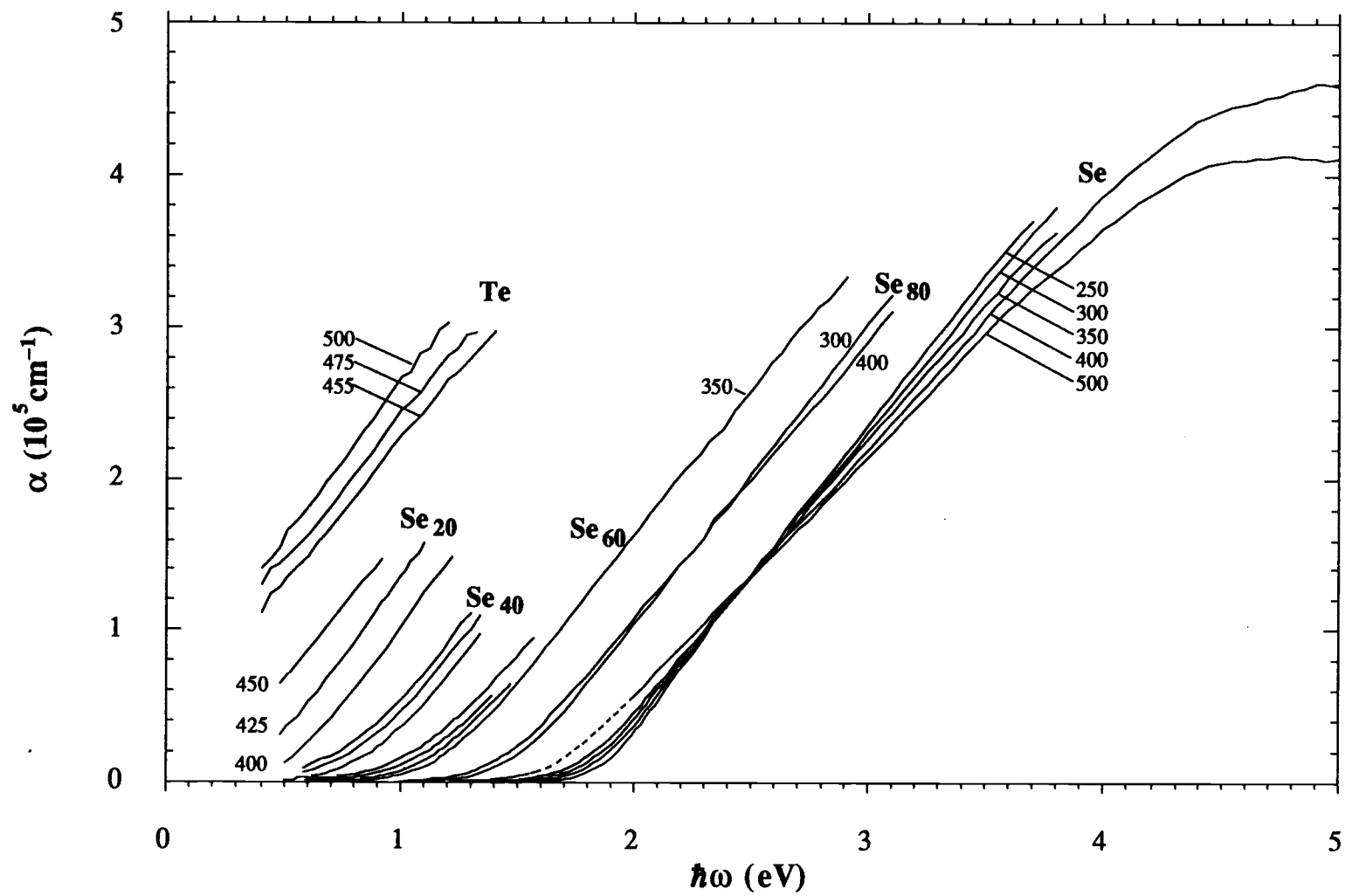
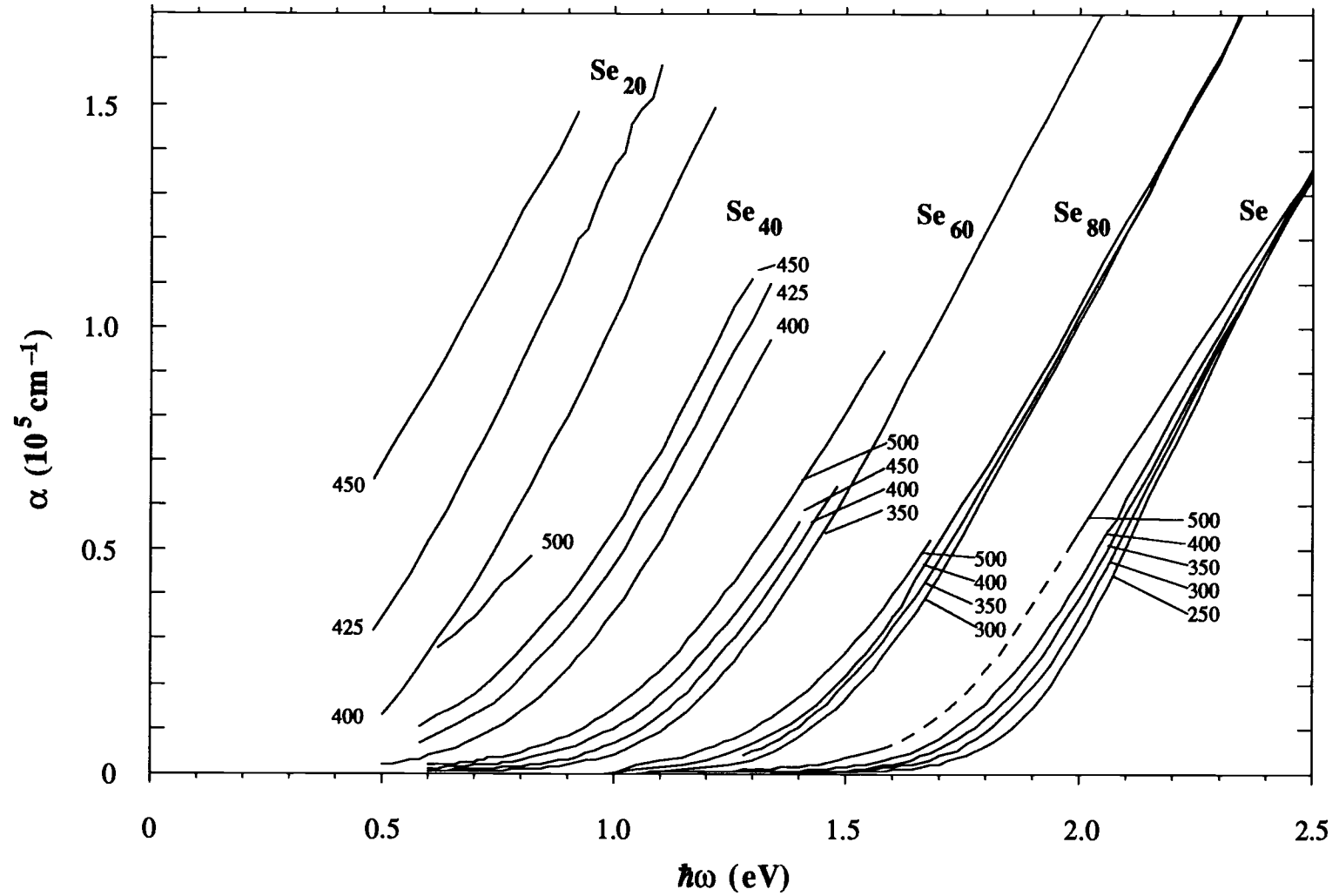


Fig 3.2 The absorption coefficient of the liquid. The Se concentration is indicated for the alloys; temperatures are in °C.



**Fig 3.3** Detail of the absorption edge above the band gap. The Se concentration is indicated for the alloys; the temperatures are in °C.



Liquid Te, however, has a negative extrapolated energy gap. Fig 3.3 gives a detailed view of the fundamental absorption edges of the alloys. Increasing the temperature or Te concentration shifts the absorption edge to lower energies, and also produces a more rounded knee at the bottom of the curve.

The absorption edge data can be used to determine how the band gap changes with temperature and composition, though it should be pointed out that there is not a definitive way of quantifying the change. The term 'band gap' really represents an inexact quantity when applied to disordered materials; there are no sharp features in the absorption edge to identify with a true gap in the density of states. Often the (optical) band gap is defined as the energy where  $\alpha$  reaches some arbitrary magnitude-- a magnitude roughly the same as the absorption coefficient at the band gap in crystalline materials. The band gap may also be defined as the energy where the extrapolation of some functional form of the absorption data reaches an arbitrary value. In this section, a measure of the band gap of the Se-Te liquids has been taken to be the energy  $E_g$  at which the absorption coefficient is  $5 \times 10^4 \text{ cm}^{-1}$ . This value of  $\alpha$  is roughly the boundary between where the slope is rising and where it becomes constant, and falls above the broad tail in the absorption data. (It is also reasonable to use the extrapolation of the linear portion of  $\alpha$  to the zero-absorption energy axis to define the band gap. This would give a smaller energy for the gap, and a larger temperature dependence than found from the  $5 \times 10^4 \text{ cm}^{-1}$  reference mark.)

Values for  $E_g$  are plotted as a function of Se concentration and temperature in Fig 3.4. The lowest temperature values plotted in Fig 3.4a are close to the melting point at each composition. These points follow a linear path fairly well from an energy of 2.1eV for liquid selenium to an extrapolated value of 0.4eV for liquid Te. This behavior might have been expected because the chain structure in trigonal

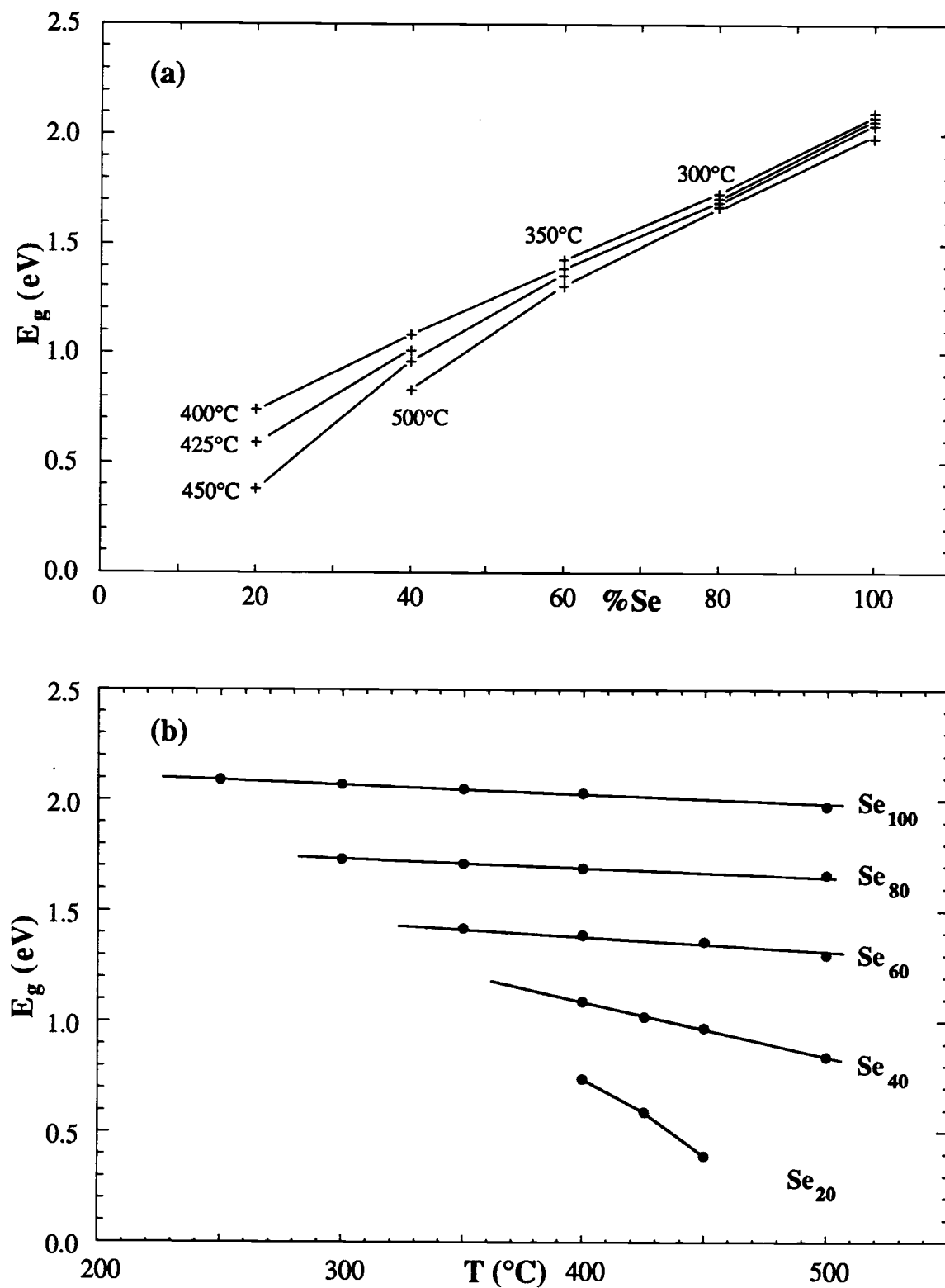


**Fig 3.4** Two views of the changes in the 'band gap' energy  $E_g$ . (a) emphasizes the concentration dependence; (b) emphasizes the temperature dependence.

Compositon	Temperature (°C)	$E_g$ (eV)	$dE_g/dT$ ( $10^{-4}$ eV/°C)	$E_0$ (eV)	$d\alpha/d(\hbar\omega)$ ( $10^5 \text{ cm}^{-1} \hbar\omega^{-1}$ )
Se <sub>100</sub>	250	2.094 eV	4.00	1.84	2.02
	300	2.075		1.81	1.92
	350	2.055		1.77	1.82
	400	2.034		1.72	1.71
	500	1.972		1.66	1.59
Se <sub>80</sub> Te <sub>20</sub>	300	1.728	4.00	1.49	2.00
	350	1.707		1.47	1.93
	400	1.688		1.43	1.85
	500	1.665		--	--
Se <sub>60</sub> Te <sub>40</sub>	350	1.422	7.72	1.18	1.95
	400	1.390		--	--
	450	1.358		--	--
	500	1.304		1.02	1.70
Se <sub>40</sub> Te <sub>60</sub>	400	1.086	24.2	.840	1.95
	425	1.019		.776	1.94
	450	.968		.737	1.98
	500	.836		--	--
Se <sub>20</sub> Te <sub>80</sub>	400	.741		.527	2.16
	425	.591		.369	2.15
	450	.358		.145	1.91
Te <sub>100</sub>	445			[-.17]	
	455			[-.18]	
	465			[-.21]	
	475			[-.22]	
	500			[-.26]	

**Tabel 2.1** Parameters for the linear absorption edge.  $E_g$  is the optical band gap referenced to  $\alpha = 5 \times 10^4 \text{ cm}^{-1}$ ;  $E_0$  and  $d\alpha/d(\hbar\omega)$  are the energy axis intercept and slope, respectively, of the linear portion of the absorption edge. Numbers in brackets for Te represent the extrapolation of the absorption curves to the  $\alpha=0$  energy axis.

Se and Te crystals is still present in the liquid state, and the data points in the figure are for liquids which have not undergone the transition to the semimetallic state. Trigonal Se has a band gap of 2.0eV, and the gap in trigonal Te is 0.32eV. The steady decrease in the band gap of the liquid reflects the energy differences in the 2-fold coordinated bonding of Se and Te atoms in the long-chain structures.

A summary of the features of the fundamental absorption edge is given in Table 3.1, where values for  $E_g$ ,  $dE_g/dT$ , the slope of the linear region, and the extrapolation of the linear region to the  $\alpha=0$  energy axis are tabulated.

### 3.3 Dielectric Function

It is often useful to express the optical properties of a material in terms of the complex dielectric function  $\epsilon = \epsilon_1 + i\epsilon_2$  because the real and imaginary factors are additive; ie, if the optical behavior can be attributed to separate physical processes a,b,c... then  $\epsilon$  is given by the sums

$$\epsilon_1 - 1 = (\epsilon_{1a} - 1) + (\epsilon_{1b} - 1) + (\epsilon_{1c} - 1) \dots$$

$$\epsilon_2 = \epsilon_{2a} + \epsilon_{2b} + \epsilon_{2c} \dots$$

Curves for  $\epsilon_1$  and  $\epsilon_2$  are plotted in Figs 3.5 - 3.8. There is little significance in the shape of  $\epsilon_1(\hbar\omega)$ , except where  $\alpha$  is small and  $\epsilon_1 \approx n^2$ . The imaginary part of the dielectric function, on the other hand, is directly related to the electronic structure of the liquid through the NDT model discussed in chapter 1. These data will be used in chapters 4 and 5 in examining the shape of the density of states in the liquid.

$\epsilon_1$  and  $\epsilon_2$  for liquid Te have been plotted on a separate graph for clarity, Fig 3.8. With the exception of the 500°C data, the data for  $\epsilon_1$  are scattered about a common curve and do not display a consistent temperature dependence. The scatter in the  $\epsilon_1$  is due to the large IR absorption of the liquid; the extinction coefficient  $k$  becomes a major term in determining the reflectance, which has the

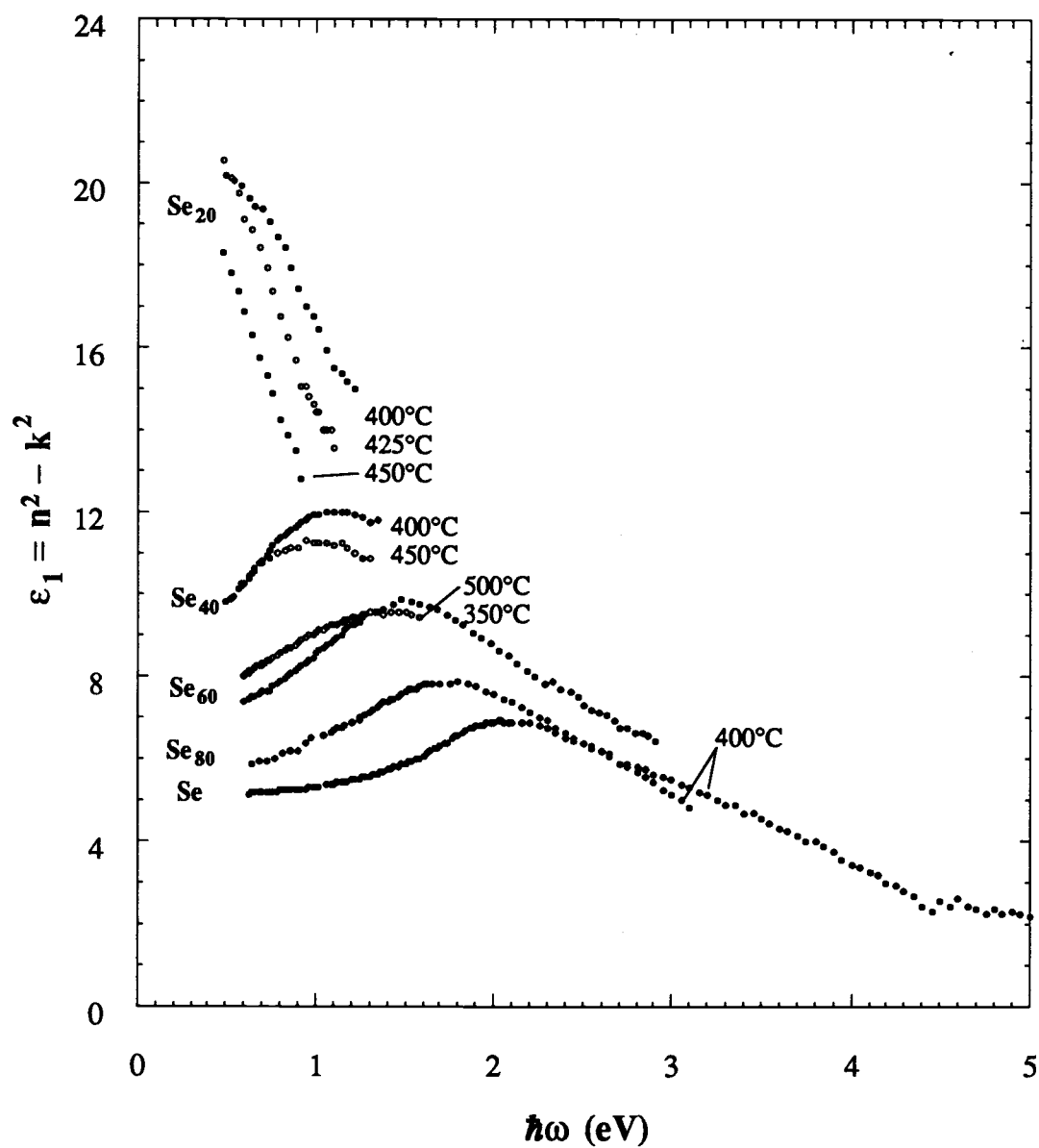


Fig 3.5 The real part of the complex dielectric function.

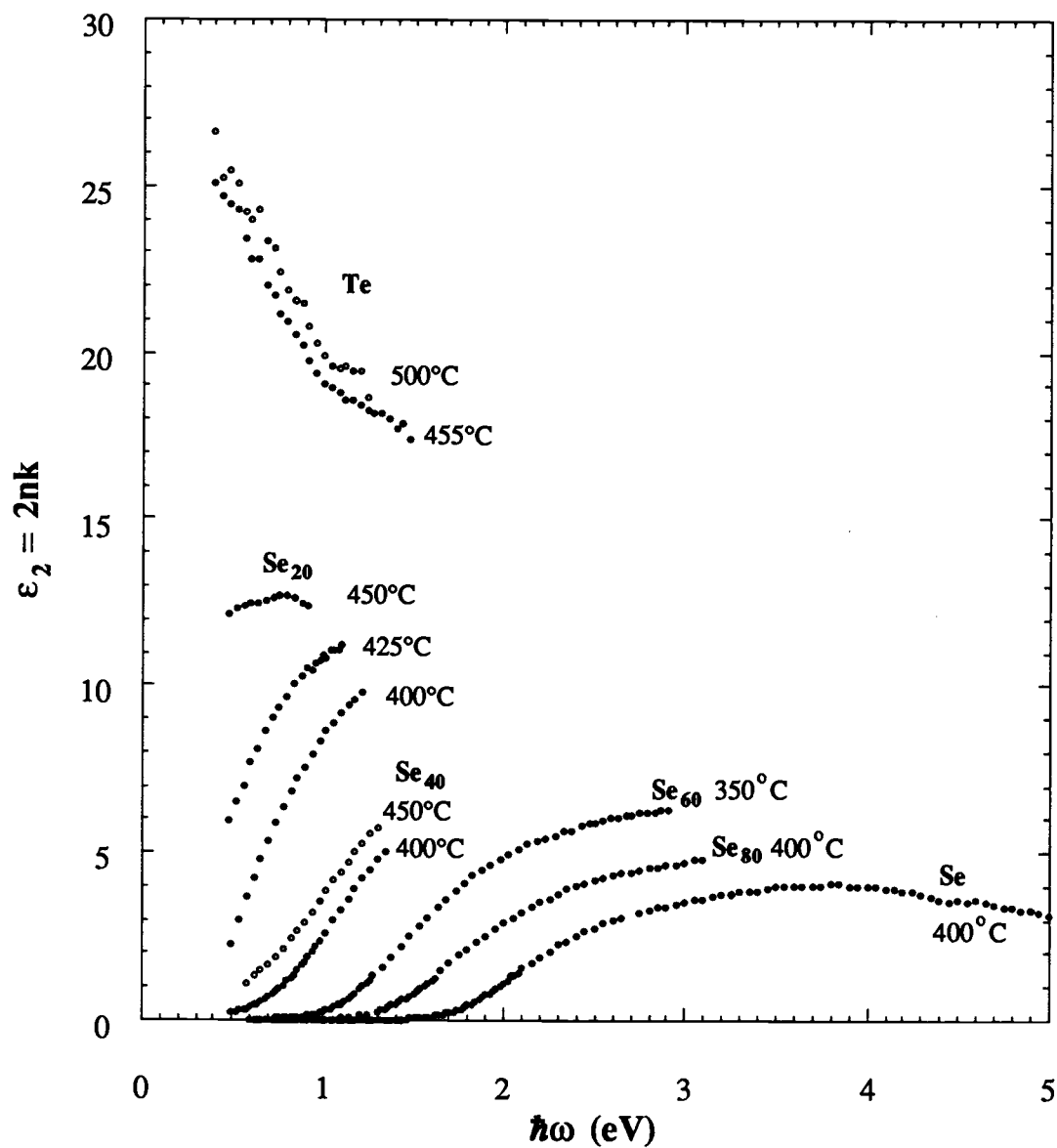


Fig 3.6 The imaginary part of the complex dielectric function.

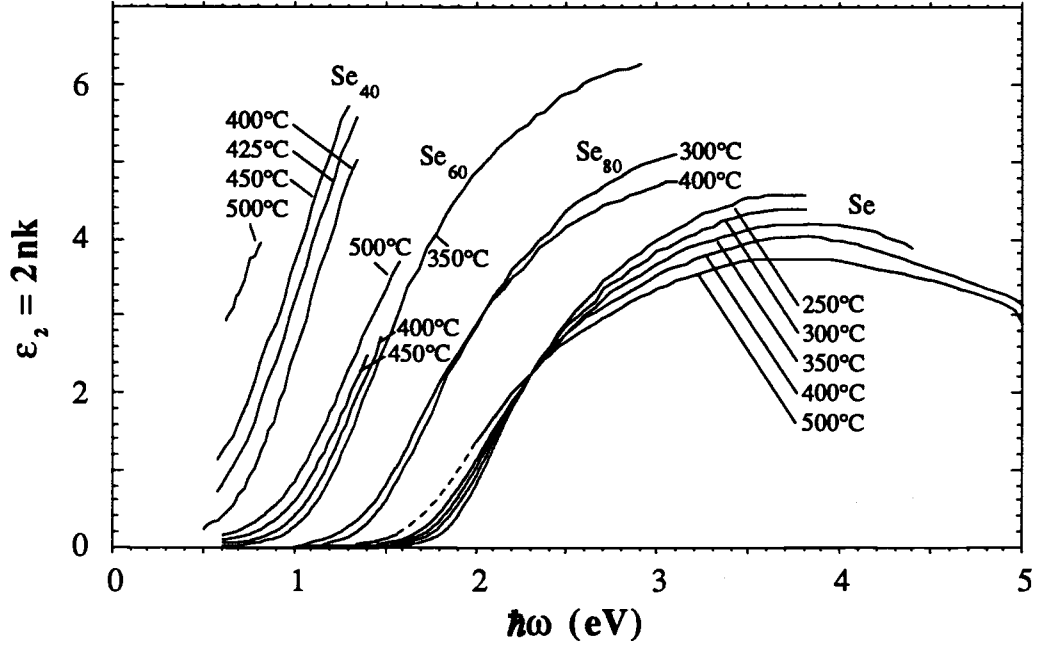
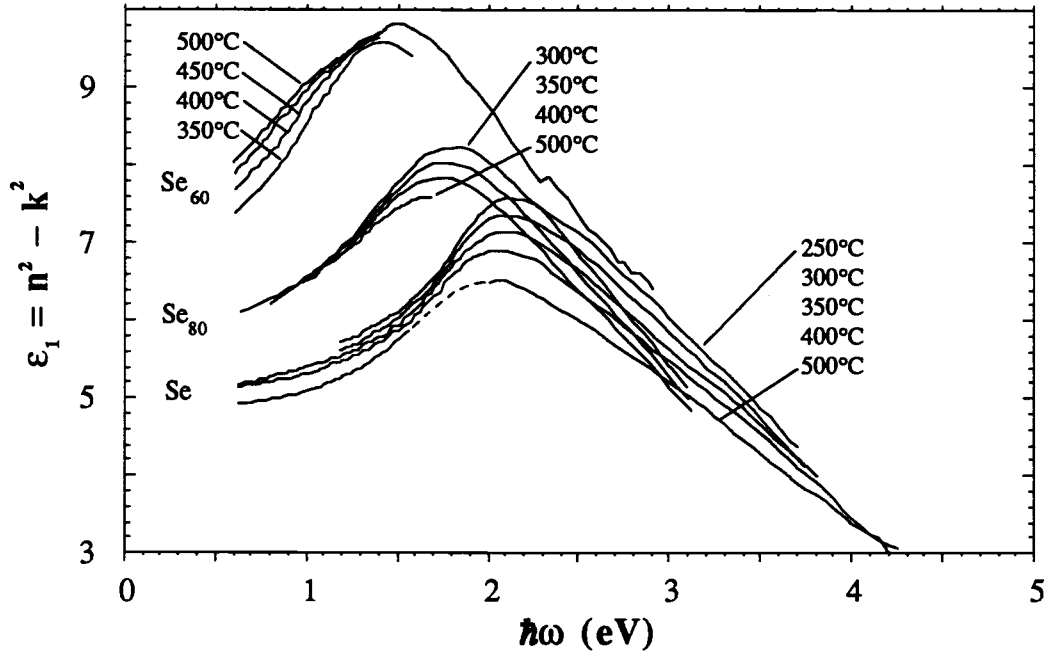


Fig 3.7 Detailed view of the complex dielectric function for the Se-rich alloys.

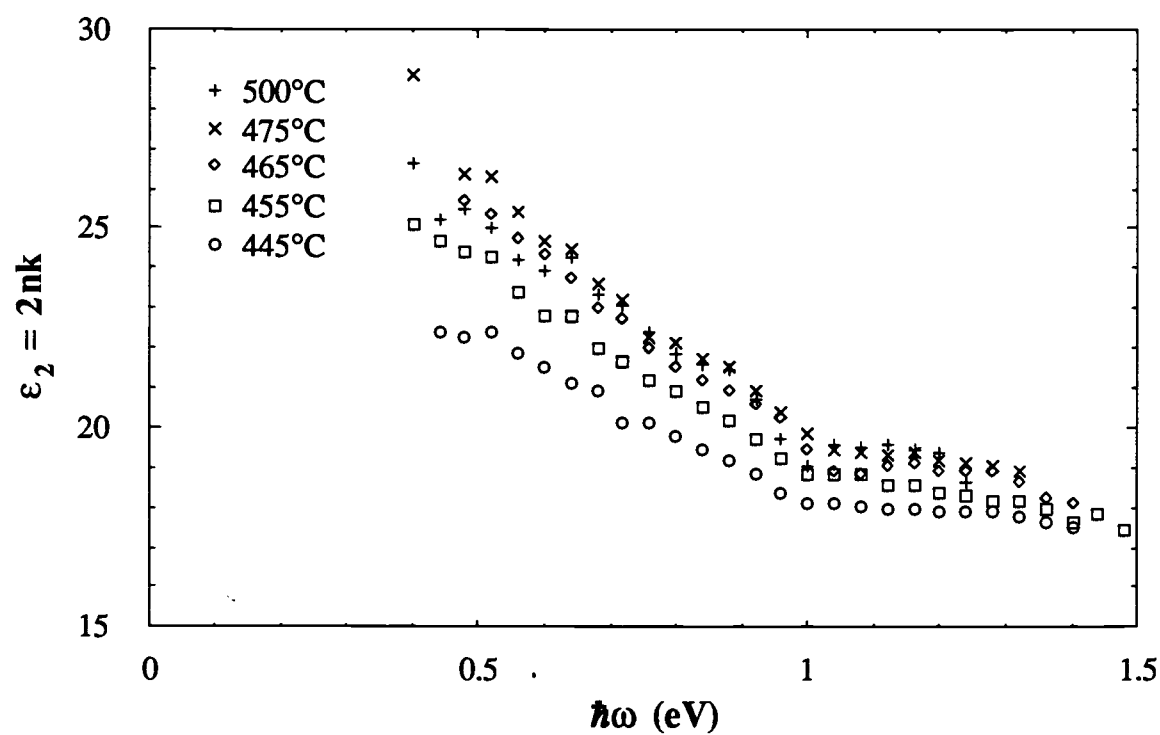
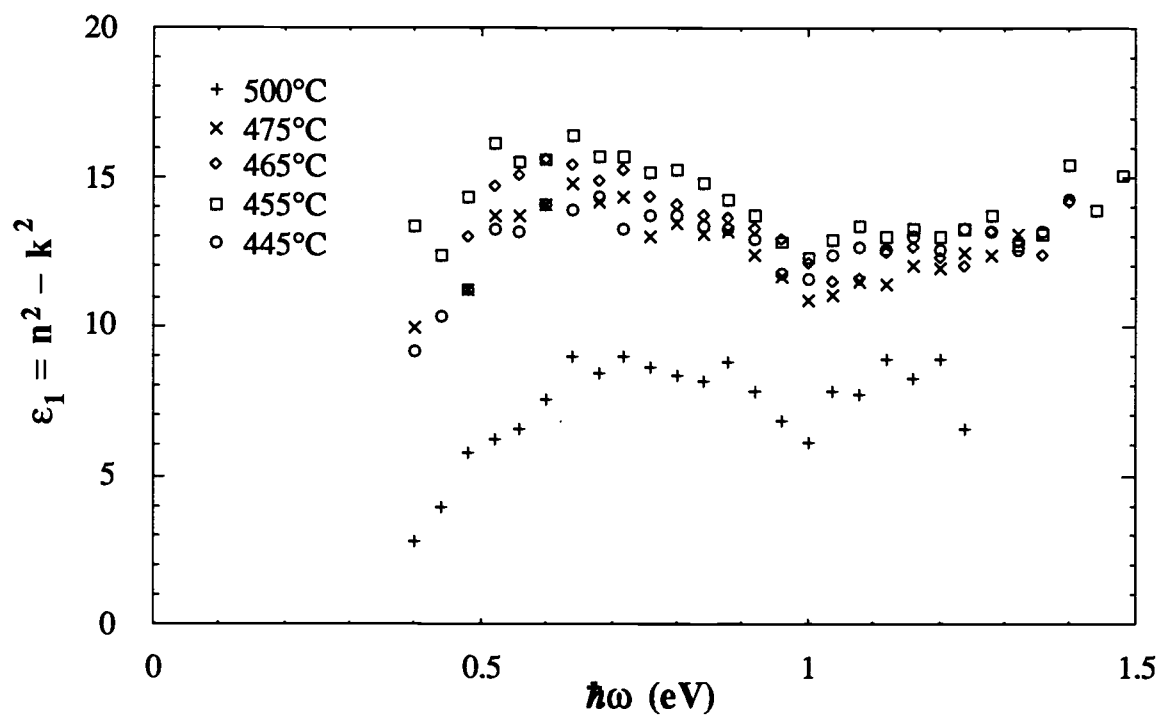


Fig 3.8 Data for the complex dielectric function of liquid Te.



effect of magnifying small errors in  $R$  when  $n$  is calculated with Eq 2.6. This error appears in  $\epsilon_1$  through the relation  $\epsilon_1 = n^2 - k^2$ . The sensitivity of  $n$  to the accuracy of  $R$  can be seen by considering the shift in the 500°C data:  $\epsilon_1$  at 500°C can be brought in line with the other measurements by increasing  $R$  by only 3%. This is within the uncertainty of the measurement.

The dispersion characteristics of Se-Te liquids have been calculated previously by Seyer *et al* using their reflectivity data, along with Perron's optical absorption data, in a modified Kramers-Kroenig analysis. Their results compare well to the results of the more direct measurements presented here. The agreement between Seyer's dispersion results, which depend entirely on the surface properties of the liquid, and the dispersion results found in this work using both the transmissivity and reflectivity of the liquid, indicates that the optical behavior of the surface is much the same as in the interior of the liquid.

### 3.4 The Absorption Edge

Data for the absorption edges of Se, Se<sub>80</sub>Te<sub>20</sub>, and Se<sub>60</sub>Te<sub>40</sub> are shown in a semilog plot in Fig 3.9. The absorption coefficient of liquid selenium exhibits an exponential dependence on photon energy below 5000cm<sup>-1</sup>. The exponential behavior of selenium's edge has been measured by several researchers previous to this work. The results found here confirm the widely held belief that at higher energies the absorption coefficient smoothly levels-off in much the same way as in amorphous Se (compare Fig 1.8). The optical behavior of the alloys containing 20% and 40% Te is similar to that of pure Se, but there is a change in the absorption properties appearing at the low absorption-end of the data which raises  $\alpha$  above the usual exponential form. A bend in the absorption curve is not present within the range of data measured for pure Se. Optical absorption measurements by Rabin

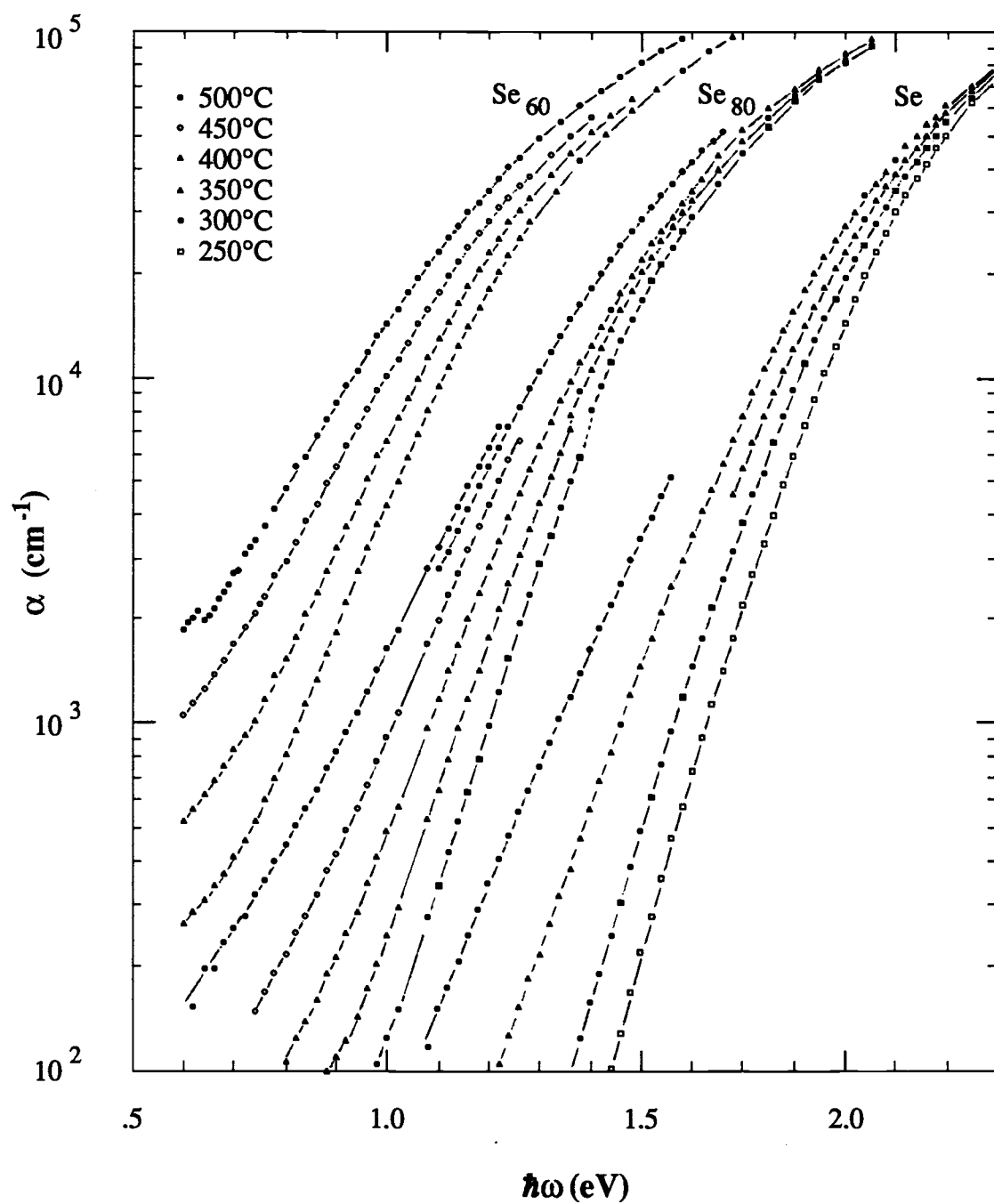


**Fig 3.9** The absorption coefficient below the band gap.

and Perron [51] on liquid Se display a temperature-dependent tailing of the edge between 10 and 100 $\text{cm}^{-1}$  similar to that found here in the alloys, but not all of the reported measurements in this absorption range are not consistent with their results. Bell and Cutler's [31] data for the absorption coefficient of Se are similar those of Rabit and Perron's between 10 and 100  $\text{cm}^{-1}$ . Below 10 $\text{cm}^{-1}$ , however, Bell and Cutler's higher temperature data bend downward, and the slope of the absorption curve increases instead of continuing to decrease. Perron [52] has measured the absorption coefficient of Se-Te alloys containing 10 to 50% Te in the range of 1 to 1000 $\text{cm}^{-1}$ . His alloy data overlap the measurements presented here only at the composition  $\text{Se}_{80}\text{Te}_{20}$ . Perron's data for  $\alpha$  between 100 and 1000 $\text{cm}^{-1}$  appear more linear than the data in Fig 3.9 indicate, but the slopes of the two different measurements are nearly the same in this region.

The source of the bend in the absorption curve appears to be due to transmission losses in the interior of the liquid. There is no anomaly in the reflectivity data in the energy range of the non-exponential absorption. This suggests that it is a bulk phenomena, and not the result of some type of surface excitation. The characteristics of the absorption edge data will be discussed further in chapter 6.

#### 4. The Density of Electron States in the Semiconducting Alloys

The non-direct transition model discussed in chapter 1 relates the optical behavior of the semiconducting alloys in the fundamental absorption region to the density of states structure in the conduction and valence bands. Unfortunately, it is not possible to use the NDT model to calculate definite forms for the band structure because the optical behavior depends on the energy dependence of three functions,  $|M(\hbar\omega)|^2$ ,  $N_v(E)$ , and  $N_c(E)$ , and their contributions to the data cannot be separated. But it is possible to investigate likely forms for the electronic structure by making reasonable assumptions about the energy dependence of two of these functions, and using the optical data to calculate the third. Whatever form these functions may have, the lack of long-range order in the liquid state implies that they should vary smoothly with energy. Even if this is not completely true the convolution process itself in Eq 1.2 tends to produce a smooth curve for  $\epsilon_2$ , and the optical data cannot be expected to indicate the presence of sharp details in  $N_v$  or  $N_c$ .

As a start in exploring the electronic structure, assume that both the conduction and valence band edges can be represented by a simple power law energy dependence with an optical gap in between; this approach was discussed in section (1.2.1). A plot of  $\epsilon_2(\hbar\omega)^2$  vs.  $\hbar\omega$  should produce a curve of the form  $|M(\hbar\omega)|^2(\hbar\omega - E_g)^r$ , where  $r=r_c+r_v+1$ , and  $r_c$  and  $r_v$  are the power factors for the conduction and valence bands. In Fig 4.1 data for Se at 250°C and 400°C are plotted in this fashion. The 250°C data are very similar to the results reported by Davis [10] for amorphous Se, which implies that the density of states structure of the liquid at the melting point is similar to that of the amorphous solid. The data for liquid Se can be fit with  $r=1.1$  over the energy interval 2.0 to 3.5eV. This is

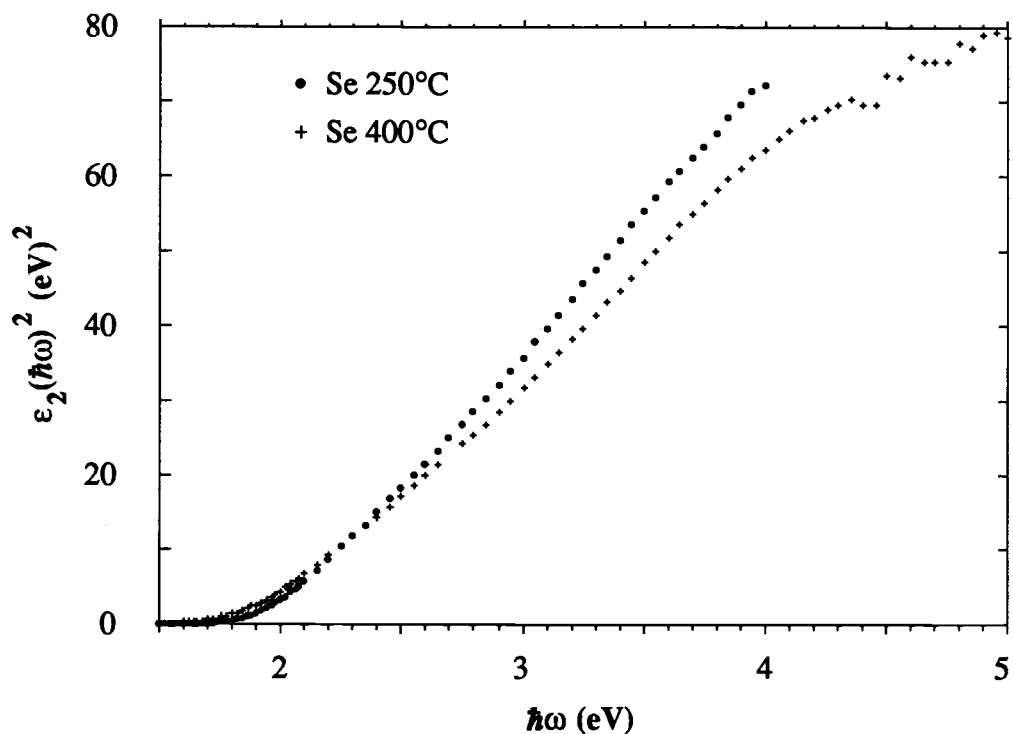


**Fig 4.1** The energy dependence of the quantity  $\epsilon_2(\hbar\omega)^2$  in liquid Se at two temperatures.

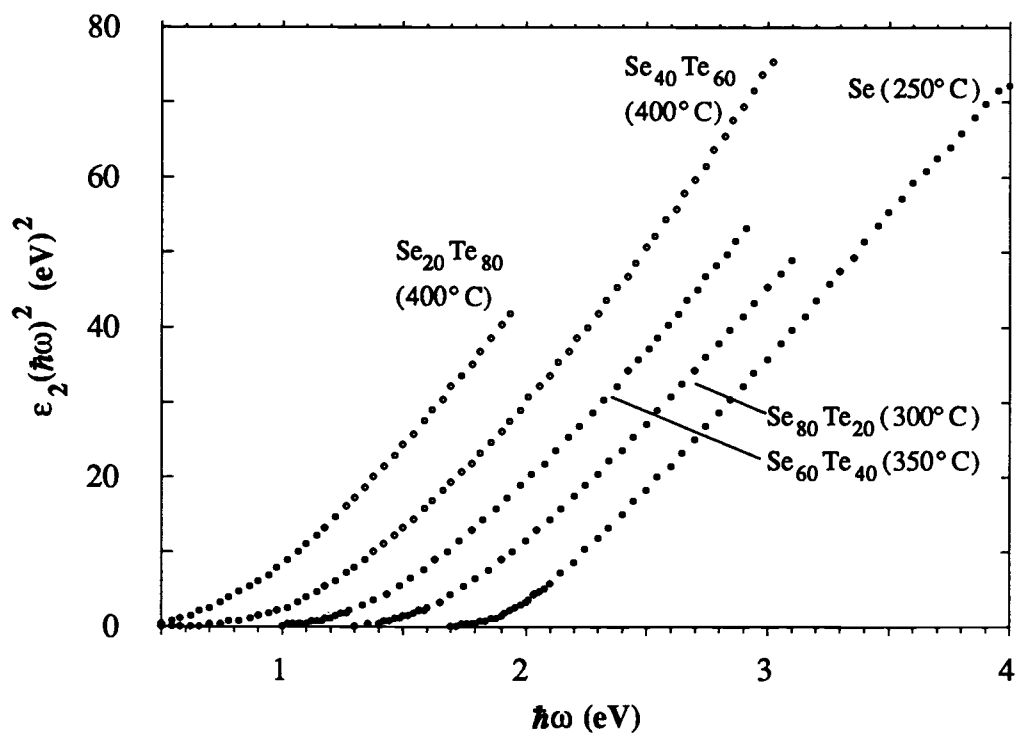


**Fig 4.2** Closed circles are data determined from reflectivity and transmissivity measurements; open circles are from reflectivity measurements alone.

significantly different from the value of 2 expected for parabolic band edges and an energy independent dipole matrix function, so the optical properties cannot be explained with a simple parabolic band model. The source of the relatively low value of  $r$  is the shape of the complex dielectric function above the optical gap. The slope of  $\epsilon_2$  for Se is steepest near the band gap and gradually decreases with energy, producing a convex contour over  $\sim 1.5\text{eV}$ , whereas  $\epsilon_2$  for most disordered semiconductors is much steeper between the band gap and the first peak, and can be concave in shape. A factor which correlates with this difference is bonding structure. Materials with a steep curve for  $\epsilon_2$  are composed of three-dimensional networks of atoms or small molecular units, while disordered materials with a long 2-fold coordinated chain structure-- amorphous and liquid Se, and liquid S at temperatures well above the polymerization point-- have a similar energy dependence for  $\epsilon_2$  and are fit with  $r \approx 1$ . Amorphous Te is also composed of 2-fold coordinated chains, but data for  $\epsilon_2(\hbar\omega)^2$  yield a value of  $r$  close to 2 for this material. This may be due to the larger degree of interchain bonding in amorphous Te compared to Se and S, which might be expected to lead to a form for  $\epsilon_2$  closer to that of the materials with a higher number of bonds per atom. In Fig 4.2 data for  $\epsilon_2(\hbar\omega)^2$  are plotted for the liquid Se-Te alloys. It can be seen that as the Te concentration is increased the curvature in  $\epsilon_2(\hbar\omega)^2$  does tend to increase-- a trend which is consistent with the optical behavior being similar to amorphous Se at one end of the composition range, and amorphous Te at the other.

To go further in determining possible forms for  $N_c$  and  $N_v$  it is necessary to make some guesses about the energy dependence of the functions going into the NDT model, and seeing what the results imply about the electronic structure of the material. The problem can be divided into two cases. In the first case,  $|M|^2$  is assumed to be relatively constant at all photon energies, and the optical properties

are determined primarily by the density of states structure. In the second case, the energy dependence of  $|M|^2$  is taken to be an important factor affecting the optical behavior. Both cases will be discussed below.

#### 4.1 $|M|^2$ Constant

The form of the calculated and measured density of states structure for amorphous and crystalline Se (Figs 1.6, 1.7), coupled with the fact that the optical behavior of Se is essentially the same in the amorphous and liquid states, suggests that the conduction and valence band edges may be fairly symmetric in the liquid. If  $|M|^2$  is constant and  $N_v(E) \approx N_c(E)$  the NDT equation reduces to  $\epsilon_2(\hbar\omega)^2 \propto \int N(E) N(E-\hbar\omega) dE$ . Functions for  $N(E)$  which match the optical data have been calculated using an iterative numerical integration procedure; the results are shown in Fig 4.3. The curves in the figure are for the position and shape of the conduction band, with the valence band being the mirror image starting at the origin of the energy axis. Keep in mind in comparing these curves that changes in the features are significant, but changes in the magnitude are not, because the proportionality factors (unit cell volume and electron effective mass) appearing in Eq 1.2 are not constants. If the assumption that  $N_v(E) \approx N_c(E)$  is correct, the band edges of Se at 250°C (Fig 4.3a) are fairly steep, followed by a slow rise in  $N(E)$  up to 3.5eV. The 400°C curve shows that increasing the temperature broadens the edge, and shifts the knee of  $N(E)$  to slightly lower energies. Increasing the Te concentration also broadens the edge (Figs 4.3 b-e) and the knee becomes a less distinct feature.

The conduction and valence bands found in this way are not inconsistent with the calculated and measured structure of amorphous Se and Te, although the steepness of the edge for liquid Se does seem unusual. There is another possibility to consider. The work done by Kao and Cutler [35] on the transport properties of

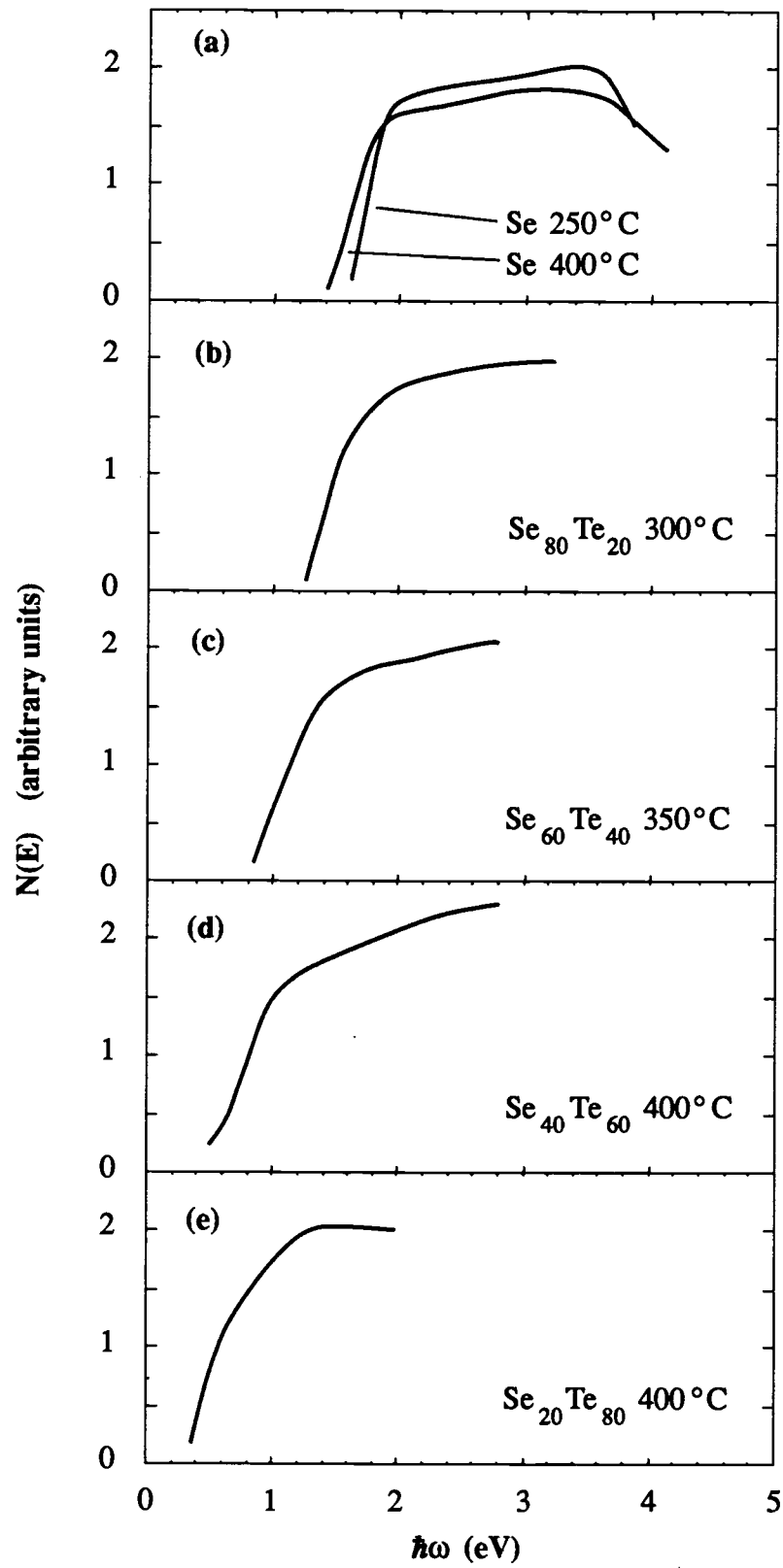
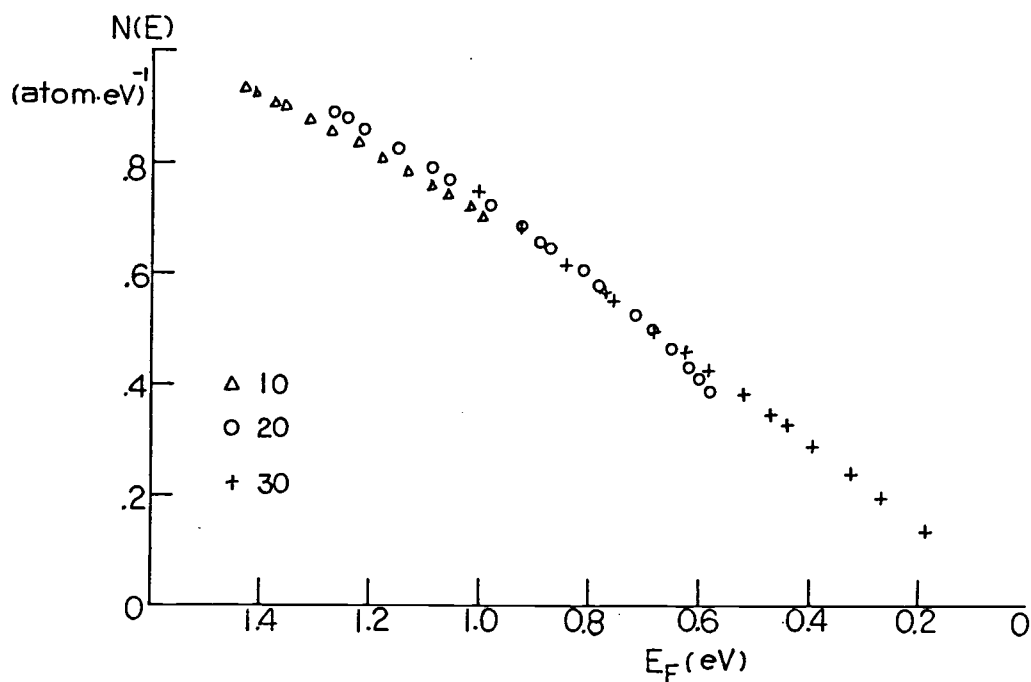


Fig 4.3 Band states calculated with the approximation  $N_v = N_c$ .



liquid Se-Te alloys suggests another way to look at the band structure. They have developed a model for the transport properties in the high conductivity regime based on the Fermi level  $E_F$  moving into the valence band as the temperature or Te concentration is increased. In their model, the magnitudes of  $N_v(E_F)$  and  $[dN_v/dE]_{E_F}$  determine the values of the dc conductivity, thermopower, and magnetic susceptibility. They were able to piece together their calculated values for  $N_v$  and its derivative to find an approximate form for the valence band edge, with the assumption that the shape of this band does not change with temperature and composition. The valence band they found (Fig 4.4) consists of a linear edge  $\sim 0.7\text{eV}$  wide followed by parabolic behavior up to  $1.4\text{eV}$ . The rigid band assumption used to derive this curve is probably not completely valid, and because this result was found for the high conductivity liquids it may be even less correct for Se rich alloys. But it does imply that the valence band edge has an energy dependence that falls somewhere between  $r_v=0.5$  and  $r_v=1$ , and it is worth investigating what this implies for the shape of the conduction band.

As it turns out, the Kao-Cutler form of  $N_v$  (linear edge followed by parabolic behavior) requires an unphysical electronic structure in the conduction band to fit the optical data. The conduction band must rise steeply to fit the data between  $1.6$  and  $2.1\text{eV}$ , and then it must drop nearly to zero and rise to large values again to fit the data at higher energies. This unphysical result is caused by the relatively slow rise of the valence band edge. The linear edge found by Kao and Cutler may, at least in part, be due to ions producing band-tail states in the liquid. Bell and Cutler have proposed a model to explain the exponential edge in liquid  $\text{Se}_x\text{Te}_{1-x}$  based on the Dow-Redfield theory using ionic defects in the liquid as the source of the microfields. To a first approximation, the ions will cause the local conduction and valence band edges to shift equally in energy, and would not lead to a change in the local optical



**Fig 4.4** Valence band density of states calculated by Kao and Cutler for metallic Se-Te alloys. The data are for liquids containing 10, 20 and 30% Se.

band gap. This means that the linear edge would not be detected in the optical measurements; the band structure seen by a photon would be closer to parabolic. But the magnitude of the tailing of the valence band edge caused by ions is probably smaller than Fig 4.4 indicates. Using the dc dielectric constant of liquid Se found by extrapolating the IR optical data, the potential energy shift in the vicinity of an ion is given by  $q/\epsilon r = (.2/r) \text{ eV}$ , where  $r$  is measured in Å. The potential energy shift of a single ion in Se is small except at interatomic distances.

The linear edge may be an artifact of the rigid band assumption used by Kao and Cutler, or it may be partly due to band tailing by ions. In either case, if the linear edge is removed and the valence band is taken to be parabolic at all energies the results for the conduction band become more reasonable. Eq 1.2 becomes  $\epsilon_2(\hbar\omega)^2 \propto \int N_c(E) (E-\hbar\omega)^{1/2} dE$ . This equation has been used to calculate  $N_c(E)$  using the same numerical procedure mentioned earlier in this section, and the results are given in Fig 4.5. For liquid Se at 250°C, a parabolic valence band leads to a conduction band with a steep edge and peak, followed by a gradual decrease in the density going into the band. The peak in the conduction band diminishes with an increase in temperature or Te concentration. It is noteworthy that the shape of  $N_c$  for the alloy  $\text{Se}_{20}\text{Te}_{80}$  in 4.5(e) is about the same as that shown in Fig 4.3(e). In both cases the conduction and valence band edges are close to parabolic.

The shape of  $N_c$  in Fig 4.5(a) is similar to the density of states in a one dimensional conductor, which suggests that the electron states in the conduction band may have one-dimensional characteristics. Such a possibility would require the electron wavefunctions of the conduction and valence bands to be very dissimilar since a parabolic valence band comes from three-dimensional electron states. The long chain structure of liquid Se does lend itself to the possibility of electron states with 1 and 3 dimensional character. The molecular orbitals which form the conduction

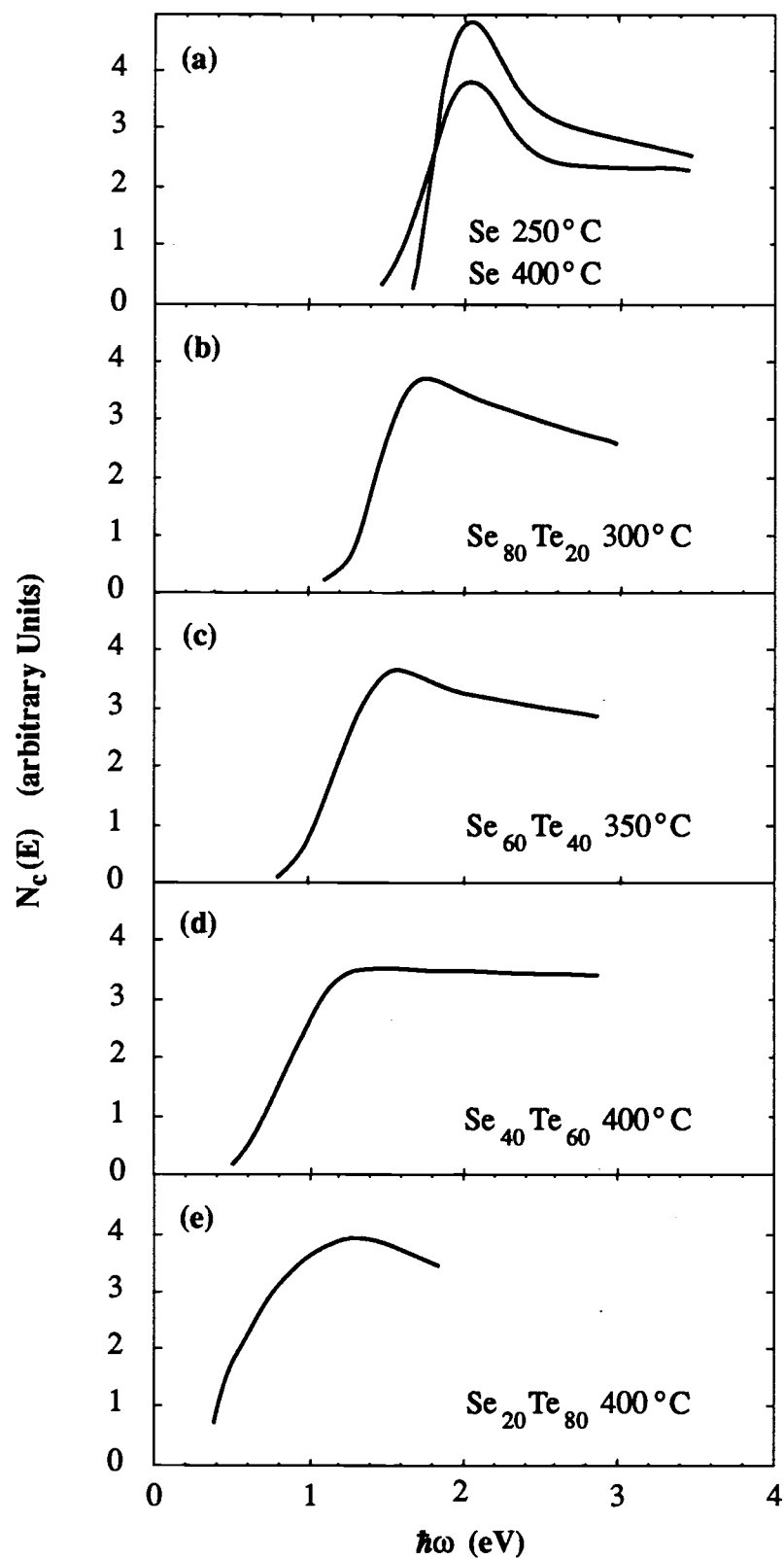


Fig 4.5  $N_c(E)$  for a parabolic valence band.

and valence bands are significantly different: the valence band is composed of lone-pair p orbitals which form weak bonds between chains, while the conduction band is formed by antibonding orbitals with a higher probability density within a chain, and therefore may be more 'one-dimensional.' Whether this picture of one and three dimensional bands is correct, though, is a difficult question to answer theoretically. The situation has to be reconciled with the data for amorphous Te, which has the same structure as Se but different optical behavior. The similarities between the amorphous and liquid forms of Se require that the peak appearing in Fig 4.5 be present in the conduction band of amorphous Se as well. Davis's  $\epsilon_2$  data for amorphous Se have a sharper bend near the band gap than the liquid data at 250°C. This means that the peak in the conduction band must be sharper and higher than in Fig 4.5a, unless the valence band is significantly different between the liquid and amorphous forms. Such a sharp feature in the electronic structure seems unlikely in view of the disordered nature of the material, and it tends to cast doubt on the validity of the one-dimensional conduction band interpretation.

#### 4.2 $|M|^2$ Energy Dependent

Considering the prevalence of parabolic band edges among disordered semiconductors it is tempting to assume that the Se-Te alloys also have parabolic band edges, and the apparent discrepancy in the measured form of  $\epsilon_2(\hbar\omega)^2$  is explained by the energy dependence of  $|M|^2$ . To examine this possibility further it is useful to replot the data for  $\epsilon_2$  in the form of  $\hbar\omega(\epsilon_2)^{1/2}$  vs.  $\hbar\omega$ , because parabolic band edges would produce a straight line in the energy range where  $|M|^2$  does not vary. This type of plot is commonly used in the literature to demonstrate the presence of parabolic band edges. The results of this procedure are somewhat ambiguous, however, when the measured optical data extend only a few tenths of an

eV above the optical band gap. The vicinity of the band gap is always a region where the curvature of  $\epsilon_2$  changes from large to small values, and data plotted in this way will always be linear over some energy range.

The  $\epsilon_2$  data for Se at 250°C are replotted as  $\hbar\omega(\epsilon_2)^{1/2}$  vs.  $\hbar\omega$  in Fig 4.6. The edge of the curve is fairly straight over an interval of  $\sim 0.4$  eV, but then the data bend downward above 2.2 eV. If the bend is due to the energy dependence of  $|M|^2$ , this energy dependence may be estimated by extrapolating the lower portion of the curve to get a value for the optical band gap  $E_g$ , and using the functions  $N_c = E^{1/2}$  and  $N_v = (\hbar\omega - E_g)^{1/2}$  in the integrand of Eq 1.2. The convolution of the the density of states then gives the relation  $\epsilon_2(\hbar\omega)^2 \propto |M|^2(\hbar\omega - E_g)^2$ , which can be solved for  $|M|^2$ . The values of  $|M|^2$  found in this way for the 250°C data are also given in Fig. 4.6. The curve looks very similar to the average matrix element function derived by Maschke and Thomas for amorphous Se, Fig 1.3. The same interpretation used by Maschke and Thomas could then be applied to liquid Se at the melting point, ie the structure of the liquid is similar to that of trigonal Se, and therefore the energy dependence of the matrix elements should be about the same with the details originating from long range order removed. One implication of this view is that the random phase model proposed by Hindley for disordered materials does not apply to Se, because the energy dependence of  $|M|^2$  in Fig 4.6 is considerable. Values of  $|M|^2$  for the liquid alloys have also been calculated and are given in Fig 4.7. Raising the temperature of Se from 250°C to 400°C greatly reduces the magnitude of the peak in  $|M|^2$ . As the composition is changed from pure Se to  $\text{Se}_{20}\text{Te}_{80}$ ,  $|M|^2$  gradually becomes more level; a peak is present in all the curves, but it appears to shift to higher photon energies as the Te concentration increases.

It is interesting to note that the energy dependence of  $|M(\hbar\omega)|^2$  found above is similar to that calculated by Abe and Toyozawa, and Dersch *et al*, with their model

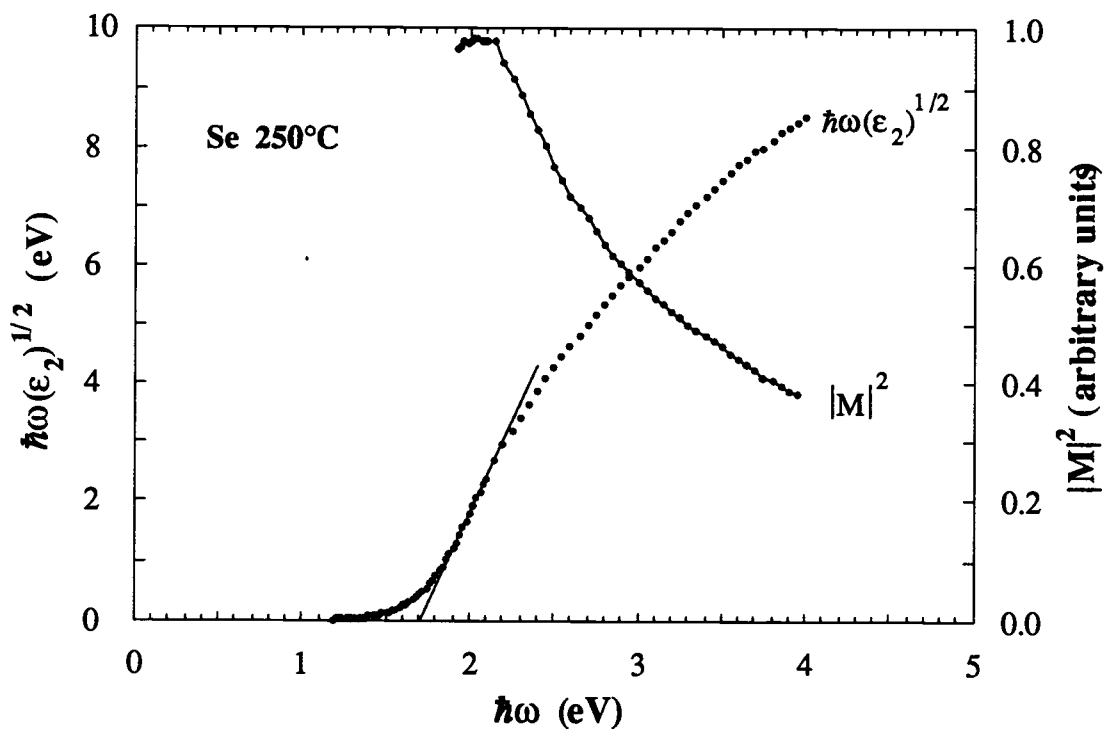


Fig 4.6 The energy dependence of the average dipole matrix function if the valence and conduction bands are taken to be parabolic.

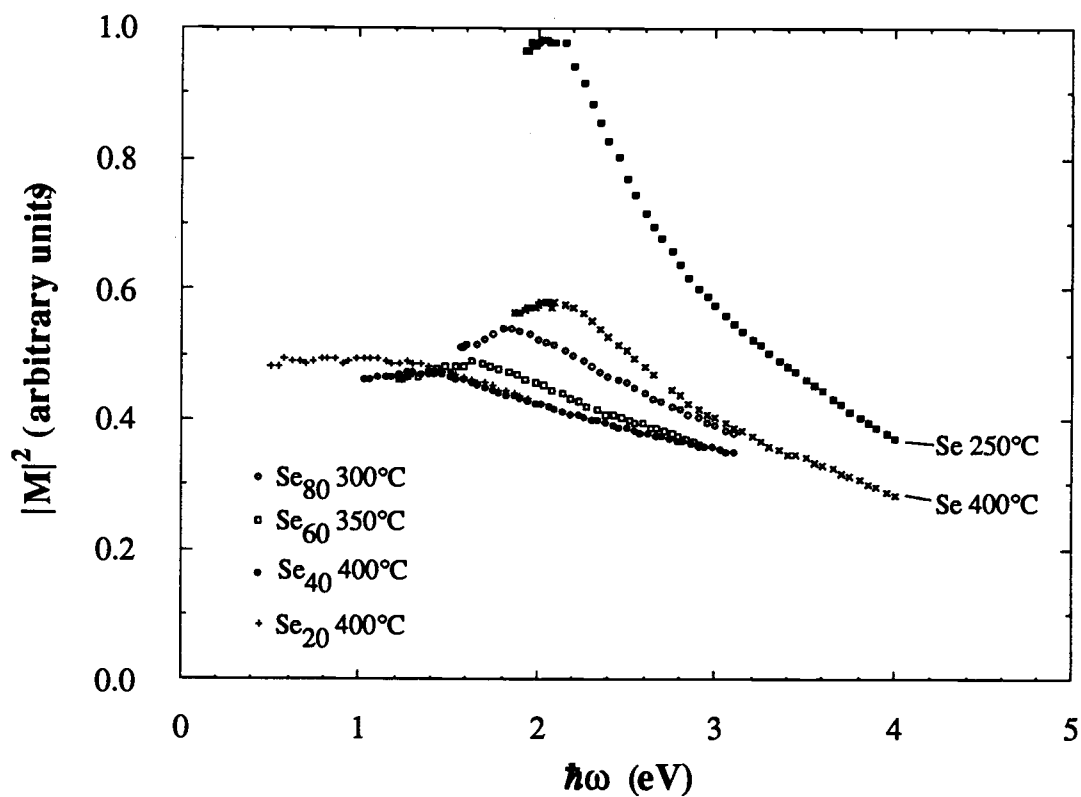


Fig 4.7 The composition dependence of the calculated average dipole matrix function.

Hamiltonian for a disordered solid. It is not certain if there really is any significance in this, however, because their model system is of a general nature, and the energy dependence of  $|M(\hbar\omega)|^2$  for Se-Te alloys (if this interpretation of the optical data is correct) appears to be unusual among disordered materials.

#### 4.3 Summary

Three possibilities for the band structure of semiconducting Se-Te liquids have been presented in this chapter, which were motivated by previous experimental and theoretical work done on these liquids, as well as other disordered materials.

- 1) The density of states in the conduction and valence bands are symmetric.
- 2) The valence band edge is parabolic, and the density of states in the conduction band follows the behavior of a one-dimensional conductor.
- 3) Both conduction and valence band edges are parabolic, and the energy dependent average dipole matrix element function  $|M(\hbar\omega)|^2$  is largest at photon energies near the optical band gap.

At the Se-rich end of the alloy composition, further measurements of the band structure of amorphous Se would help sort out which of the three models may be correct. If a peak is found in the edge of  $N_c(E)$  then it would provide support for the second possibility. If a peak is not found then a comparison of the steepness and symmetry of the band edges in amorphous Se could distinguish between the first and third possibilities. Of course, it is also quite conceivable that the situation is more complicated than any of the three simple band edge models considered here.

The results for the band structure in Figs 4.3 and 4.5 indicate that the band structure of the semiconducting alloys is not static against changes in temperature



and Te concentration, especially between the alloys  $\text{Se}_{40}\text{Te}_{60}$  and  $\text{Se}_{20}\text{Te}_{80}$ . It appears very likely that liquid  $\text{Se}_{20}\text{Te}_{80}$  at  $400^\circ\text{C}$  does have parabolic valence and conduction band edges, at least up to  $1.3\text{eV}$ . This is the situation just before the semiconductor-semimetal takes place, which will be discussed in the next chapter.

## 5. The Semiconductor-Semimetal Transition

In the semiconducting regime the optical properties of Se-Te alloys change gradually with temperature and composition, the most notable change being the shift of the optical band gap to lower energies. The first indication of the semiconductor-semimetal transition in the optical measurements occurs in the sample  $\text{Se}_{20}\text{Te}_{80}$  at  $450^\circ\text{C}$ . The absorption coefficient near  $0.5\text{eV}$  is higher than expected for a shift in the band gap alone, indicating that new absorption processes are taking place. In the case of liquid Te the absorption data extrapolate to a negative optical gap. This is just the result of a large density of free carriers at the Fermi level, which is expected in the semimetal state. Two models for the semiconductor-semimetal transition have been discussed in Chapter 1. The 2-fold to 3-fold bonding transition model proposed by Cabane and Friedel does not seem to fit the optical data very well. In the temperature range of the measurements presented here ( $445^\circ\text{C}$ - $500^\circ\text{C}$ ), their interpretation of the neutron diffraction data predicts that the liquid is in a mixed bonding state with both 2 and 3-fold bonds present. 60% of the atoms would be in the 3-fold state at  $445^\circ\text{C}$ , and 85% at  $500^\circ\text{C}$ . It is not known what the density of states structure would look like in this mixed bonding state, but it seems to require a major re-arrangement of the electron levels in the vicinity of what was formerly the semiconductor band gap, and the band gap should be replaced by a substantial overlap of  $\sigma$  and  $\sigma^*$  energy levels. This would lead to a larger value for the absorption coefficient than has been measured. The optical data for liquid Te are consistent with the semiconductor-semimetal transition proposed by Cutler, however, and this will be demonstrated in this chapter.

### 5.1 The Optical Properties of Te. and the Drude Model

A diagram of Cutler's model for the density of electron states in liquid Te is shown in Fig 5.1. There are a large number of vacant states, or holes, at the top of the valence band; this places the Fermi level at an energy  $E_F$  below the valence band edge. The conduction band edge is above the Fermi level at an energy denoted by  $E_1$ . From this figure it is apparent that the optical absorption of the liquid can be attributed to the contributions of two different electronic transitions: intraband transitions which take an electron from below  $E_F$  to empty valence states above  $E_F$  (or equivalently, a hole transition in the opposite direction), and interband transitions which take an electron below  $E_F$  into the conduction band. If this model is correct, subtracting the intraband contribution to the optical data should yield a second optical component which has essentially the properties of a semiconductor with a band gap  $E_1$ . The purpose of this chapter is to show that this is indeed the case.

The intraband contribution to the optical behavior can be estimated using the Drude model for free-carrier absorption. As discussed in chapter 1, this simple model fairly accurately describes the optical properties of liquid metals. The Drude model is somewhat less valid for liquid Te than for liquid metals because of its relatively high resistivity, but it should be noted that for the higher resistance liquid metals (eg Hg and Bi) the Drude model underestimates the actual optical absorption. The error in using this model for the intraband component of the optical behavior is therefore most likely on the side of predicting a minimum intraband contribution.

Three parameters are need in Eq 1.1 to calculate the intraband behavior: the hole effective mass  $m^*$ , the dc conductivity  $\sigma_0$ , and the density of holes per unit volume  $n$ . Values for the dc conductivity of liquid Te in the temperature range of the

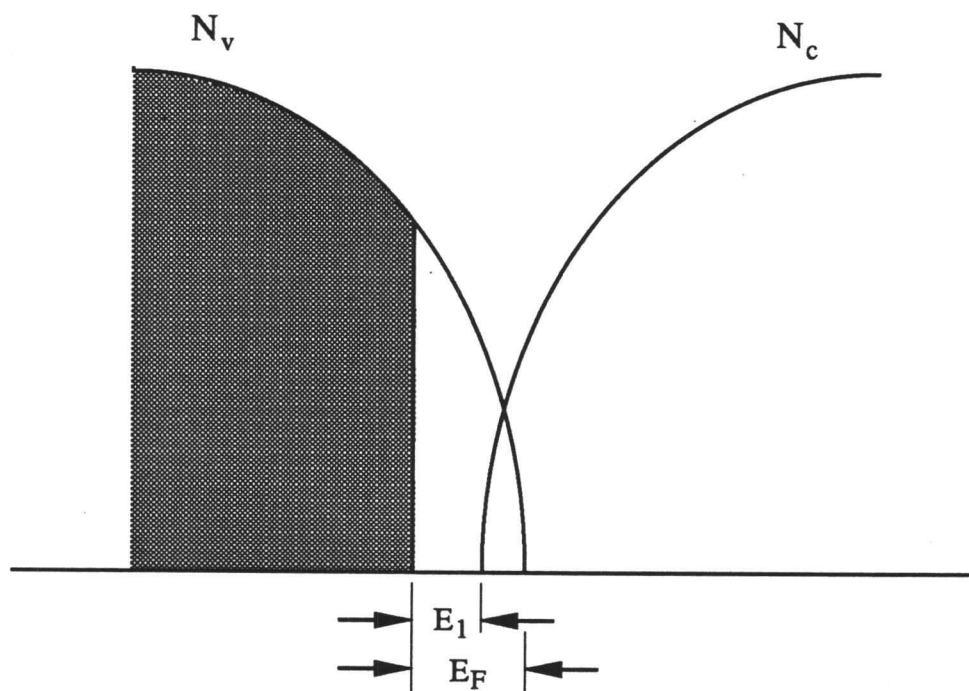


**Fig 5.1** The band structure model used to separate the intra- and inter-band contributions to the optical data.  $E_F$  is the Fermi energy measured from the valence band edge.  $E_1$  is the energy between the highest filled valence level and the conduction band edge.

optical data have been measure by Perron; his data at 445°C, 475°C and 500°C are listed in Table 5.1. The effective mass  $m^*$  is expected to be larger than the free electron mass  $m_e$ , but its value can only be approximately determined. Kao and Cutler have calculated values for  $m^*$  along with  $n$  in the high conductivity regime for the alloys containing 10% to 30% Se. A diffusive transport model was used to simultaneously fit the dc conductivity, thermopower and magnetic susceptibility of the liquid. The values for  $m^*$  they obtained were  $2.45m_e$  for  $\text{Se}_{20}\text{Te}_{80}$  and  $2.38m_e$  for  $\text{Se}_{10}\text{Te}_{90}$ . The optical effective mass is not necessarily the same as the effective mass determined by transport measurements, but the magnitudes should be approximately the same. A value of  $2.35m_e$  will be used for  $m^*$  in the intraband calculations for liquid Te, with an uncertainty of perhaps  $\pm 0.5m_e$ .

The density of holes in liquid Te is the least accurately determined quantity going into this model. Values for  $n$  can be calculated in two ways. In the first method it is assumed that the valence band is basically parabolic in form, as suggested by the band structure calculations for  $\text{Se}_{20}\text{Te}_{80}$  in the previous chapter. It follows that  $n$  is related to the density of states at the Fermi energy  $N(E_F)$  and the effective mass by

$$n = \frac{h^6 \pi^4}{3m^{*3}} N^3(E_F) \quad (5.1)$$

The density of states at the Fermi energy can be calculated using the data for the magnetic susceptibility of the liquid measured by Gardner and Cutler. The relation between  $\chi_m$  and  $N(E_F)$  is

$$\chi_m = \chi_d + (\alpha - \beta)\mu_B N(E_F), \quad (5.2)$$

where  $\chi_d$  is the diamagnetic contribution of the atomic cores, which is taken to be a constant, and the second term is the sum of the Pauli paramagnetic and Landau diamagnetic properties of the holes. The quantity  $(\alpha - \beta)$  has the value  $(1 - 1/3) = 2/3$

for free electrons. Its value is not known for liquid Te, but it is reasonable to expect ( $\alpha-\beta$ ) to be of order unity, and this estimate will be used here. The core diamagnetism  $\chi_d$  has been taken to equal to the magnetic susceptibility of Te at room temperature,  $3.8 \times 10^7$  (cm<sup>3</sup>/mole). The values of  $n$  calculated using  $\chi_m$  and  $m^*=2.35m_e$  are listed in Table 5.1 under the column labeled  $n_1$ .

A second method to calculate  $n$  uses the hole densities found by Kao and Cutler for the 10%, 20%, and 30% Se alloys in the temperature range where the diffusive model is valid. Since the electronic and thermodynamic transitions in Se-Te alloys are correlated, there should be a functional relation between the hole density and the volume contraction of the liquid measured by Thurn and Ruska [38]. Cutler and Rasolondramanitra [53] have derived an empirical expression for the volume contraction by formulating the problem in terms of a law of mass action reaction, where the thermodynamic transition involves transforming the liquid from a low-temperature, low-density form to a high-temperature, high-density form. The atomic volumes (average volume per atom) in the low density form  $V_L$ , and the high density form  $V_H$ , were taken to be linearly dependent on temperature. The measured atomic volume at a given temperature  $V_A$  falls between these two extremes, and the fractional volume contraction of the liquid was defined by

$$C_v = \frac{V_L - V_A}{V_L - V_H} .$$

The law of mass action expression they found for  $C_v$  is

$$\frac{C_v}{1 - C_v} = e^{(-E+ST)/k_B T} , \quad (5.3)$$

where the enthalpy  $E$  is .815eV and the entropy  $S$  depends linearly on the concentration of Se atoms as  $S/k_B = 15.0-.104(x)$ . A plot of  $C_v$  vs.  $n$  for the alloys containing 10%-30% Se, as obtained from Eq 5.3 and the data in reference [35], is

shown in Fig 5.2. The data for the three compositions do fall on roughly the same curve, which supports the hypothesis that  $n$  and  $C_V$  are functionally related.

Values for the hole density in liquid Te were found from this curve by calculating  $C_V$  using Eq 5.3, and locating the corresponding value of  $n$  along the curve. The results are labeled as  $n_2$  in Table 5.1.

**Table 5.1** The free-carrier parameters for the valence band holes.

$T(^{\circ}\text{C})$	$\sigma_o(10^3 \text{ ohm}^{-1}\text{cm}^{-1})$	$m^*(m_e)$	$n_1(10^{22} \text{ cm}^{-3})$	$n_2(10^{22} \text{ cm}^{-3})$
445	1.70	2.35	1.49	1.21
475	1.91	2.35	1.76	1.48
500	2.07	2.35	2.01	1.66

The hole densities found in this way are about 20% smaller than the hole densities found via the parabolic valence band calculation; this is considered to be good agreement in view of the approximations and numerical uncertainties involved. The two methods used to determine  $n$  are not independent of each other, however.  $n_1$  was calculated using an effective mass derived from the diffusive transport model, and both  $n_1$  and  $n_2$  are based on the assumption that  $(\alpha-\beta)=1$ . In the calculations to follow for the intraband optical properties the results for  $n_2$  will be used for the hole density.

Before calculating the intraband contribution to the optical behavior of Te there is one more factor concerning the applicability of the Drude model which should be addressed. Typically in liquid metals the Fermi energy is located high enough in the conduction band that the energy dependence of the density of states does not effect the optical response of the metal. To see this, consider Faber's model for the high frequency conductivity

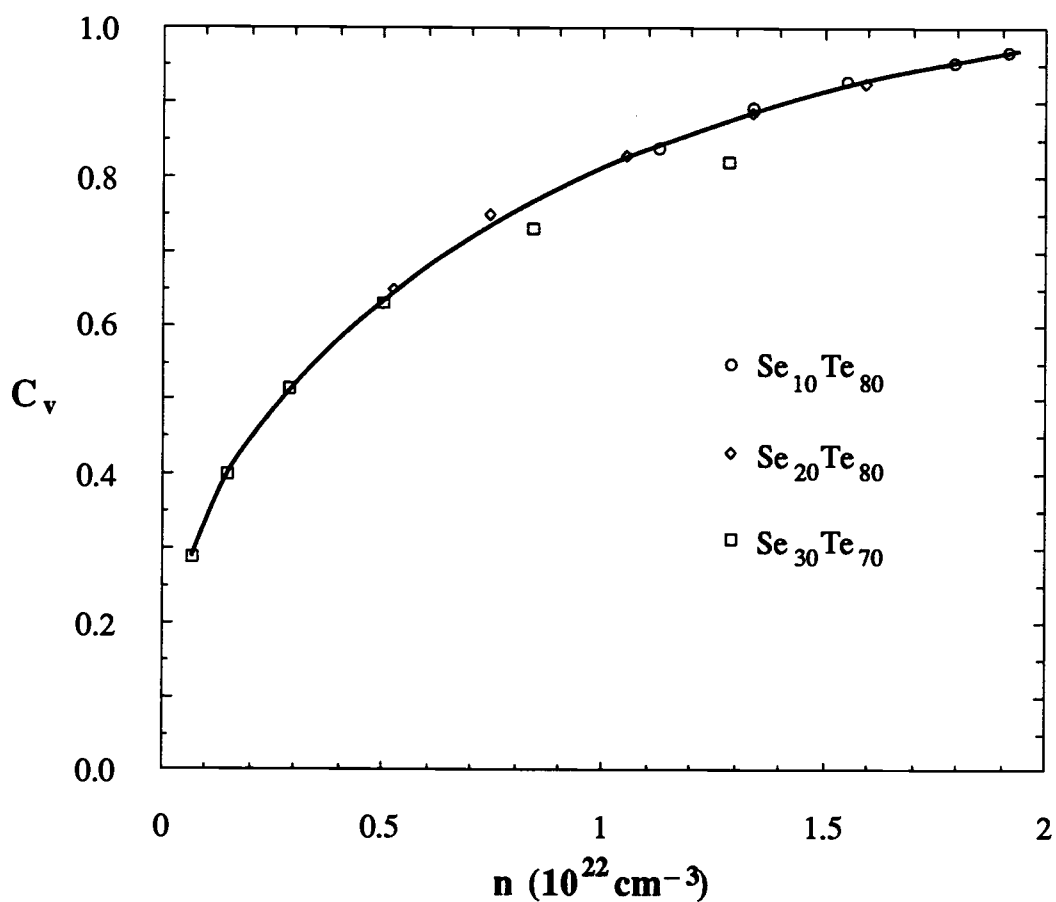


**Fig 5.2** The volume contraction plotted against the hole concentration in the liquid.

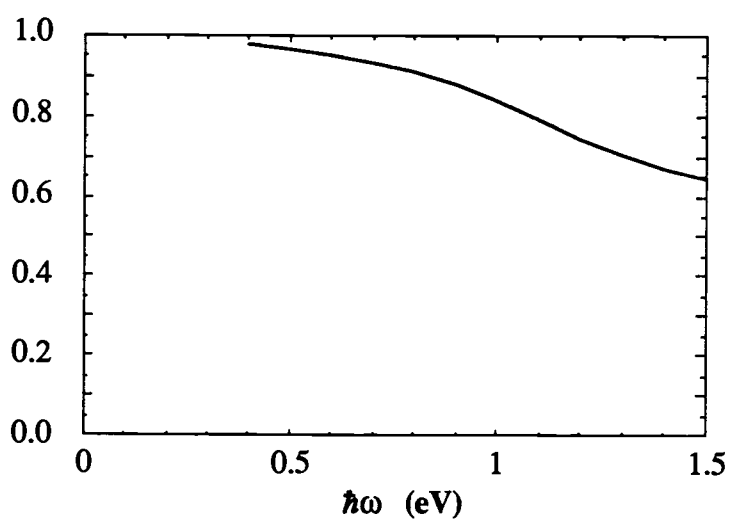


**Fig 5.3** The factor  $(1/\hbar\omega N_F^2) \int N(E) N(E+\hbar\omega) dE$  for a parabolic conduction band and  $E_F = 1 \text{ eV}$ .



$$\sigma(\omega) = \left[ \frac{ne^2\tau/m^*}{1 + (\omega\tau)^2} \right] \left\{ \frac{1}{N^2(E_F)} \frac{1}{h\omega} \int N(E) N(E + h\omega) dE \right\} \quad (5.4)$$

This equation is similar the non-direct transition model used in connection with the optical properties of liquid semiconductors. The first factor in brackets is just the usual Drude expression for the optical conductivity. The factor in braces is a factor which depends on the band structure  $N(E)$  in the conduction band. For a parabolic band, the second term is near unity at photon energies smaller than the magnitude of the Fermi energy (measured from the band edge), and it is the first term which determines the energy dependence of the conductivity. This condition is always satisfied by liquid metals in the infrared and visible part of the spectrum. Monovalent metals like Na, for example, have a Fermi energy  $\sim 5\text{eV}$ , and the Fermi energy of polyvalent metals is higher. The parameters listed in Table 5.1, however, correspond to a Fermi energy of only  $1\text{eV}$ , and the energy dependence of the second term in Eq 5.4 will affect the optical behavior of the holes. The magnitude of this factor has been calculated for a parabolic conduction band with  $E_F = 1\text{eV}$ , and the results are shown in Fig 5.3. The small width of the hole band causes the optical conductivity to decrease at higher photon energies. The effect is small enough that, for the purposes of the results being sought here, it is not important. The Drude equations will still be used to calculate the interband contribution to the optical behavior. In doing this, the results will overestimate the intraband contribution to the dielectric function at higher energies, but in the range of  $0.4\text{-}0.8\text{ eV}$  the error is negligible.

## 5.2 The Intraband and Interband Optical Components

Now the complex dielectric function of liquid Te will be separated into intraband and interband components. Denoting the measured dielectric function by

$(\epsilon_{1m}, \epsilon_{2m})$ , the interband dielectric function by  $(\epsilon_1, \epsilon_2)$ , and expressing the intraband hole contribution in terms of a complex conductivity  $(\sigma_1, \sigma_2)$ , these three quantities are related by

$$\begin{aligned} \epsilon_1 &= \epsilon_{1m} + \frac{\sigma_2}{\omega} \\ \text{and} \\ \epsilon_2 &= \epsilon_{2m} - \frac{\sigma_1}{\omega} \end{aligned} \quad (5.5)$$

The equations for the complex conductivity, written in terms of the effective mass, dc conductivity, and hole density, are

$$\begin{aligned} \frac{\sigma_1}{\omega} &= \frac{\sigma_o \hbar}{(\hbar\omega) + (\hbar\omega)^3 (\sigma_o m^* / \hbar n e^2)^2} \\ \text{and} \\ \frac{\sigma_2}{\omega} &= \frac{(\sigma_o m^* / n e^2)}{1 + (\hbar\omega)^2 (\sigma_o m^* / \hbar n e^2)^2} \end{aligned} \quad (5.6)$$

Using Eqs 5.5 and 5.6, values for  $(\sigma_1, \sigma_2)$  and  $(\epsilon_1, \epsilon_2)$  have been obtained. In Fig 5.4 the results for Te at 445°C are plotted to show the relative magnitude of the interband and intraband terms in the complex dielectric function. The data for  $\epsilon_2$  (the interband curve) clearly show the energy dependence expected for a gap between the highest filled valence band states and the conduction band edge. The results for  $\epsilon_1$  and  $\epsilon_2$  have been used to determine the absorption coefficient the liquid would have if the intraband processes were turned off. The absorption curves for Te at 445°C, 475°C, and 500°C are shown in Fig 5.5. The points fall along roughly the same curve, and the intercept with the energy-axis indicates that the energy  $E_1$  in Fig 5.1 is approximately 0.4eV.

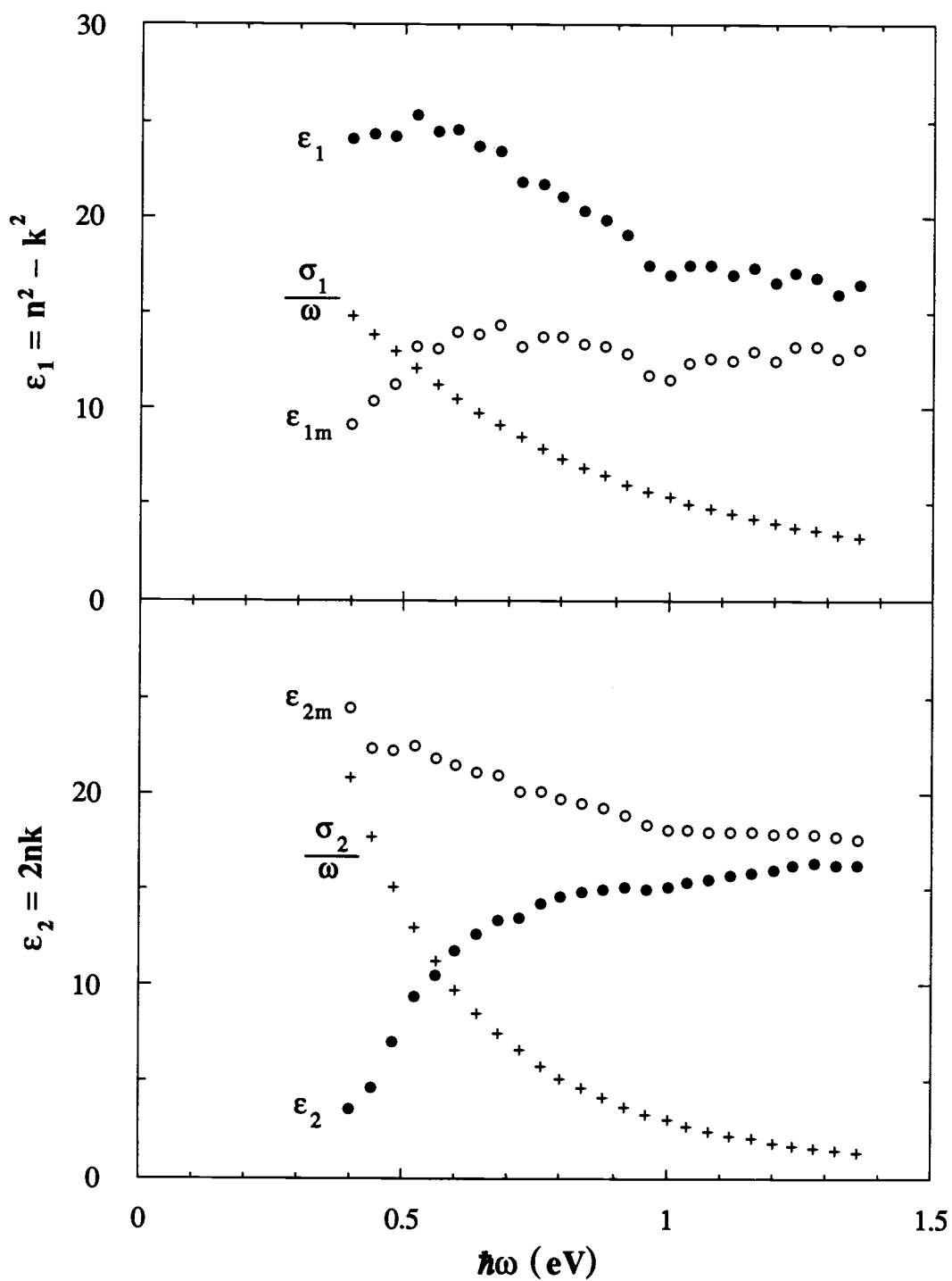


**Fig 5.4** The measured complex dielectric function of liquid Te at 445°C  $\epsilon_m$  separated into interband  $\epsilon$  and intraband  $\sigma/\omega$  components. (Note that the data are plotted in Gaussian units, though  $\sigma/\omega$  is an MKS expression.)

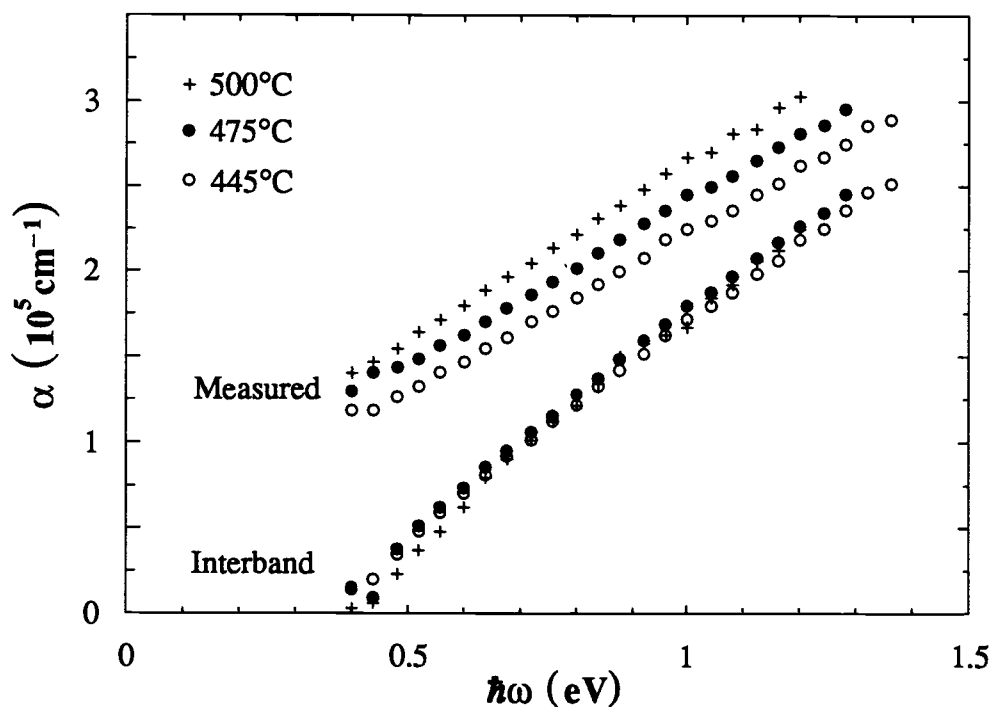


**Fig 5.5** Data for the measured absorption coefficient of liquid Te plotted along with the absorption coefficient of the calculated interband component.

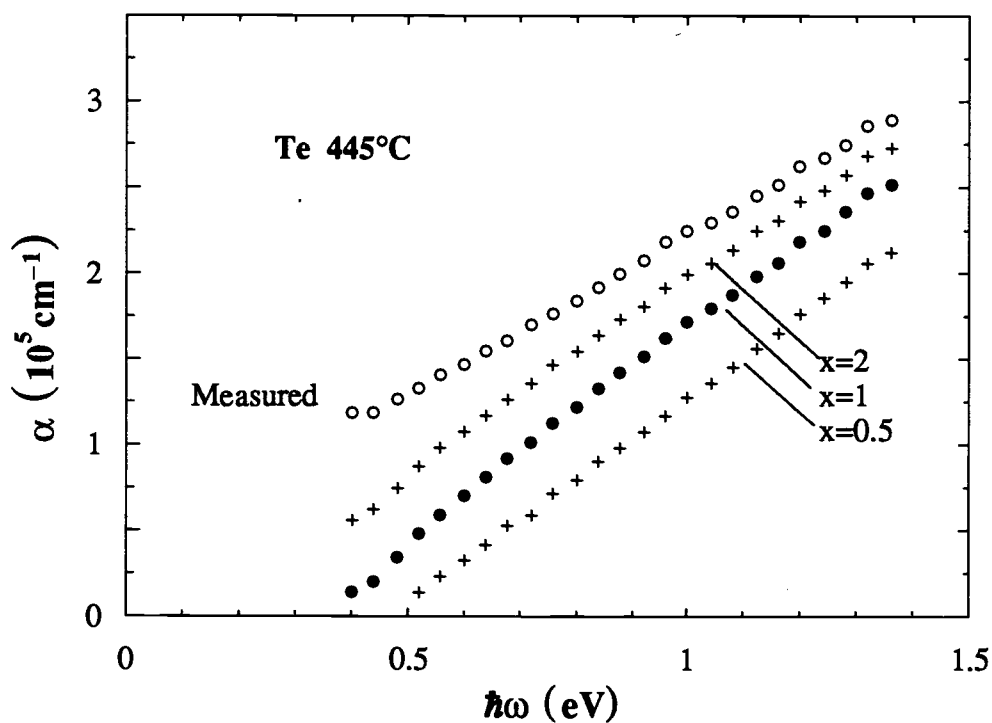


**Fig 5.6** The effect of changing the ratio  $m^*/n$  by the factor  $x$  on the calculated interband absorption.

The sensitivity of the interband results found above to the parameters used in the Drude model has been examined by varying the parameters and recalculating the absorption coefficient. The dc conductivity is accurately known, and is not considered a source of error, but the effective mass and hole density do have a range of uncertainty. These two parameters appear as a ratio ( $m^*/n$ ) in the complex conductivity. The interband absorption coefficient has been calculated in the cases where this ratio is larger by a factor of 2 and smaller by a factor of 1/2. The results in Fig 5.5 show that over a considerable range of the input parameters a gap between the Fermi energy and the conduction band edge still is found.

### 5.3 Implications for the Microscopic Structure

If the two fold bonding of the atoms persists across the semiconductor-semimetal transition, as the optical data seem to indicate, this has interesting consequences for the microscopic structure of the liquid. The high concentration of holes in Te requires a high concentration of broken bonds, and therefore very short chains. The hole densities in Table 5.1 correspond to an average chain length of 4.5 atoms at 445°C, and 3.3 atoms at 500°C. If the electronic and structural changes in Cutler's model are correct, there still remains the question as to what causes the thermodynamic transition. A decrease in the compressibility and increase in the density are also associated with the semiconductor-semimetal transition; these changes call for the introduction of a new type of bonding interaction between the atoms. Undoubtably, this new interaction must somehow be related to the short length of the 2-fold bonded units in the liquid. In the neutron diffraction data for liquid Te, the ratio of the height of the radial distribution peak in the first coordination shell to the following minimum is small, which means that the lifetime of the bond between a pair of atoms is very short. The liquid is in a very dynamic

state. And if the more recent interpretation of the diffraction data (which allows for penetration of the first coordination shell by non-covalently bonded Te atoms) is correct then the secondary bonding interaction must make it possible for atoms on neighboring 2-fold bonded units to come together as close as the covalent bonding distance, but without appreciably altering the band structure of the liquid.

Recently Cutler *et al* [54] have proposed that the secondary bonding interaction could be attributed to electrostriction: negative ions in the liquid polarize their neutral neighbors, thus causing an electrostatic bonding interaction. The effects of electrostriction were calculated using macroscopic concepts and parameters in a domain which should properly be treated microscopically, and their numerical results are therefore of limited accuracy. The results do show, however, that the magnitude of the electrostrictive interaction is sufficient to explain the observed volume contraction of the liquid.

## 6. The Absorption Edge

To complete the description of the optical properties of liquid Se-Te alloys, data for the optical absorption coefficient below the band gap have also been measured. These data add to the relatively small amount of information currently available on the the absorption edge behavior in liquid semiconductors, and in particular, they provide additional information about Urbach absorption. The properties of the absorption edge in liquid Se have been studied more extensively than other liquid semiconductors; this is because the crystalline, amorphous, and liquid phases of Se provide one of the best examples of an exponential edge among covalently bonded materials. The measurements presented here show how the properties of this edge change when Se is alloyed with Te. Unfortunately, this data does not lend itself to distinguishing between the absorption mechanisms which may be responsible for the form of the edge. In this chapter nothing more will be done than to place the optical behavior observed in this experiment in the context of previous experimental and theoretical work on the optical properties of liquid Se.

### 6.1 Comparison of Experimental Data

The absorption edge data shown in Fig 3.9 exhibit two features: approximately exponential behavior below  $\sim 5000 \text{ cm}^{-1}$ , and in the case of the alloys, a non-exponential tail at the lowest measured values of  $\alpha$ . The range of exponential behavior in the data, ie the width of the linear portions of the curves, decreases as the temperature and Te concentration are increased, and this feature gradually becomes less defined. In fact, the very short range of exponential behavior in the  $\text{Se}_{60}\text{Te}_{40}$  data would not be considered significant if it were not seen as part of a transition from the optical properties of Se. It appears that the

absorption mechanism responsible for the tailing of the edge affects the optical behavior at only the lower values of the absorption coefficient. Therefore, the properties of the exponential portion of the data will be investigated separately from the lower non-exponential data.

In Fig 6.1 the data for liquid Se are shown to project to a common focal point in the typical fashion of an Urbach absorption edge. The results of a least-squares fit to the exponential portion of the data are also shown in the figure. The focal point is not as well defined in the alloy samples, Figs 6.2 and 6.3. This may be, at least in part, due to the limited range of the exponential behavior, which makes it difficult to define the end-points to use for the curve-fit. The temperature and composition dependence of the exponential data can be represented by the Urbach expression

$$\alpha = \alpha_0 e^{(\hbar\omega - E_0)\sigma/kT}$$

if the steepness parameter  $\sigma$  is taken to be temperature dependent. Values for  $\sigma$  and  $\alpha_0$  have been calculated using the exponential functions  $Ae^{-m\hbar\omega}$  listed in Figs 6.1-6.3. The slope factor  $\sigma/kT$  is equal to  $m$ ; by multiplying  $m$  by  $kT$  the values of  $\sigma$  were determined, and the results are shown in Fig 6.4. The prefactor in the Urbach equation  $\alpha_0$  was found from the relation  $\ln(A) = \ln(\alpha_0) - E_0(\sigma/kT)$ . The focal-point energies indicated in Figs 6.1-6.3 were used for the energy parameter  $E_0$  in these calculations. Within the uncertainty of the measurements,  $\alpha_0$  was found to equal  $e^{12.0}$  independent of temperature and composition. The values obtained for the exponent were all in the range of  $12.0 \pm 0.2$ .

The slope of the absorption edge and its dependence on temperature are important factors in characterizing the optical behavior of the edge. The data for  $\sigma$  found in this work are compared to previous measurements by other researchers in Fig 6.5. There is a surprisingly large variation in both the magnitude and



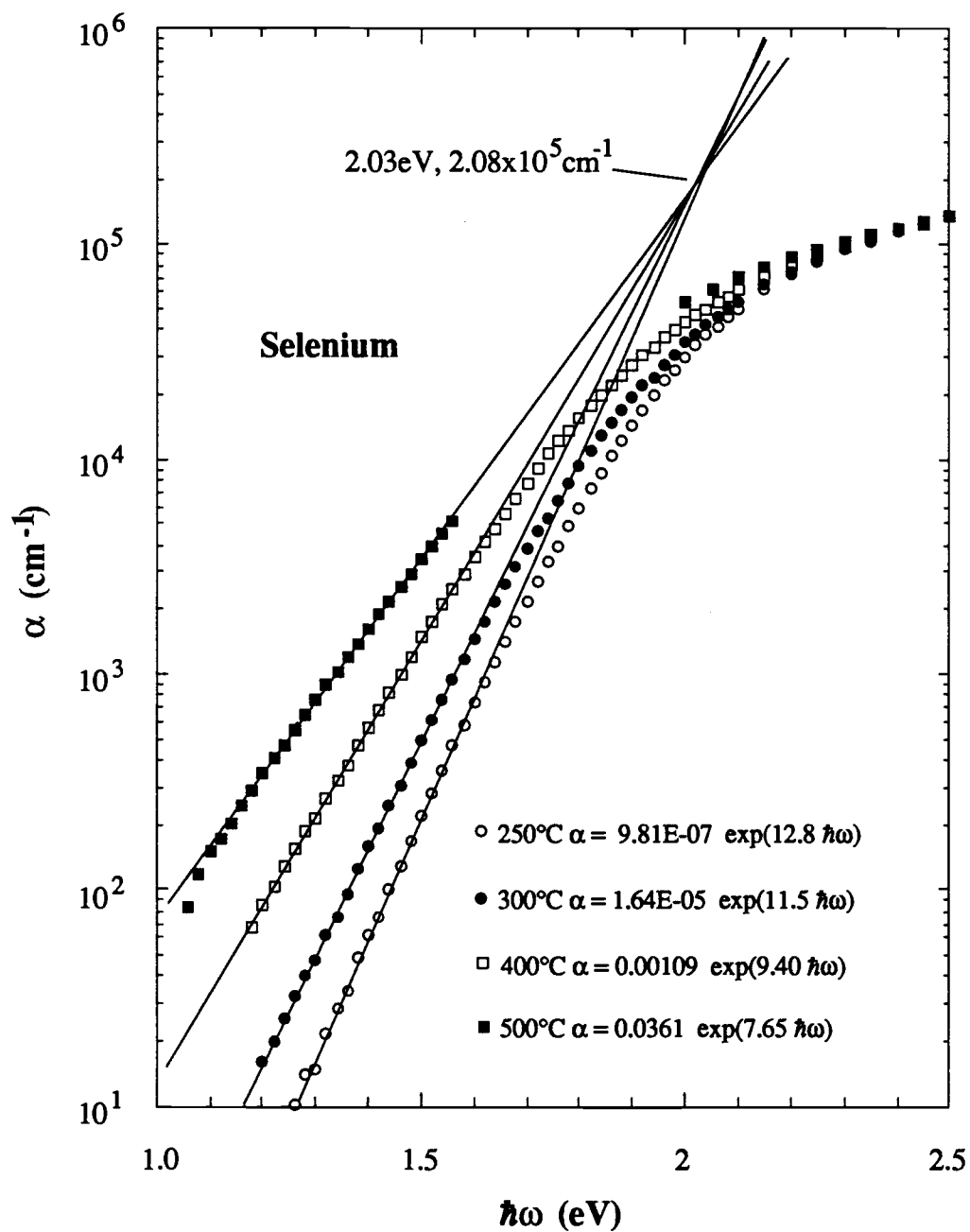


**Fig 6.1** The exponential absorption in liquid selenium.

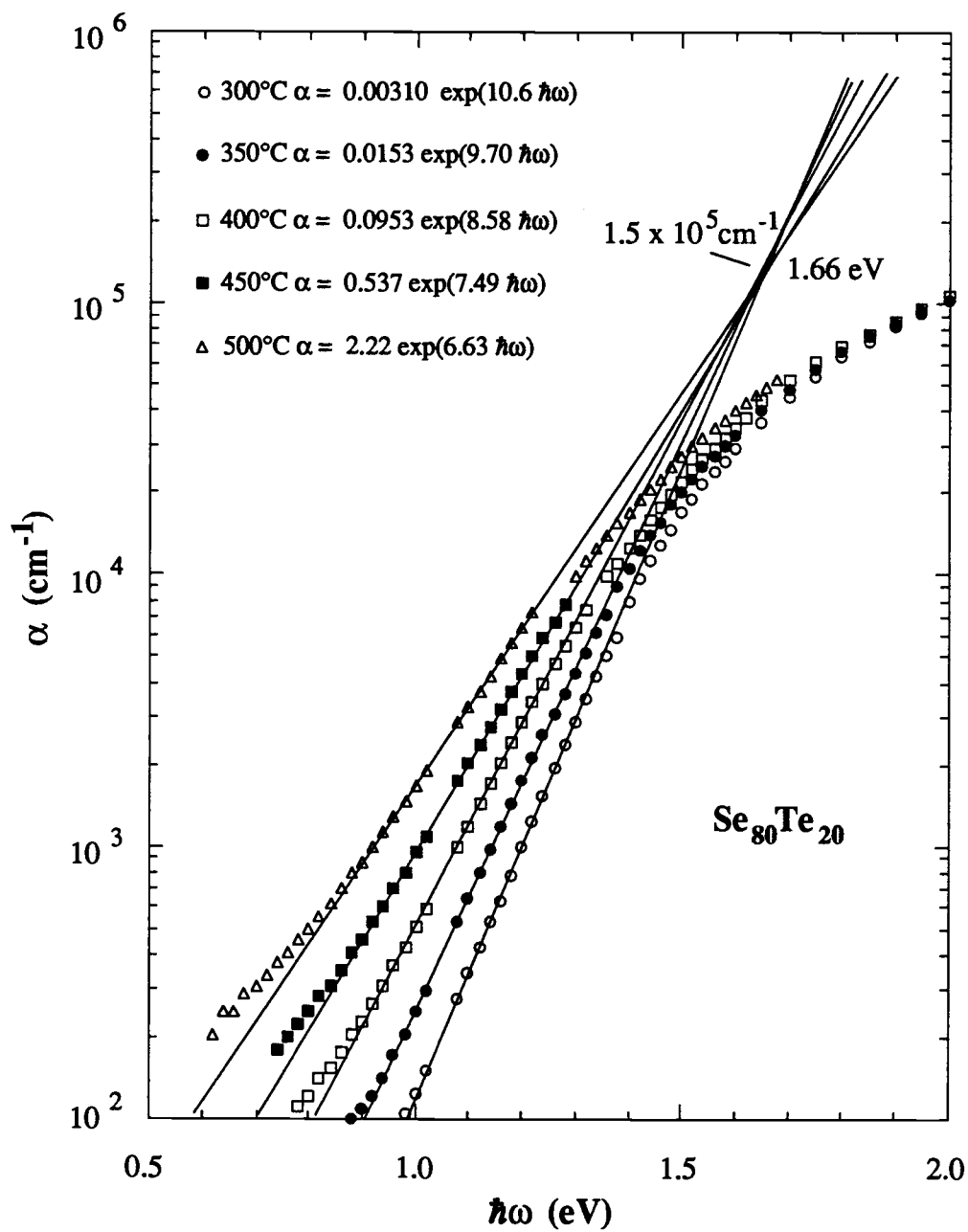


Fig 6.2 The exponential absorption in liquid  $\text{Se}_{80}\text{Te}_{20}$ .

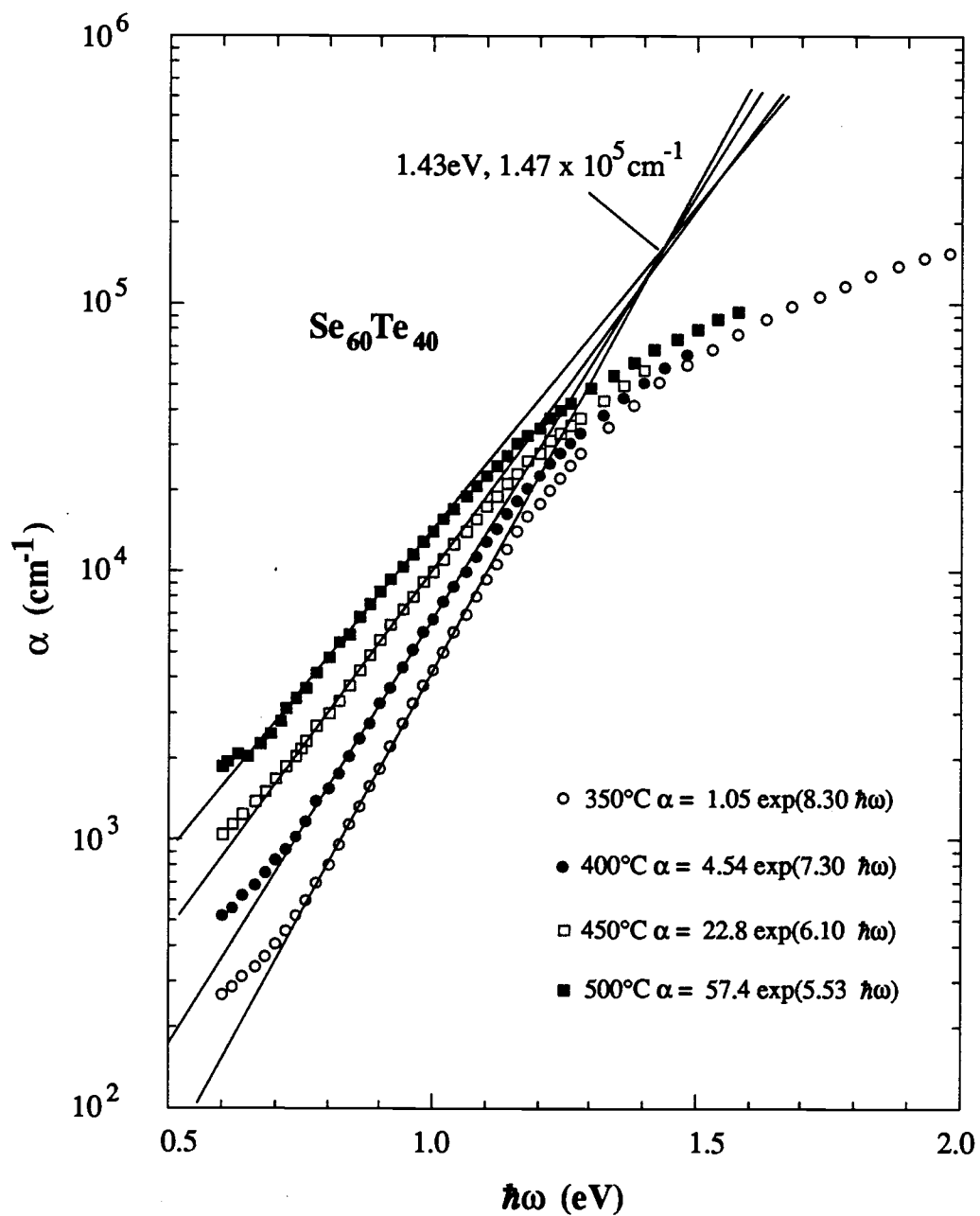


Fig 6.3 The exponential absorption in liquid  $\text{Se}_{40}\text{Te}_{60}$ .

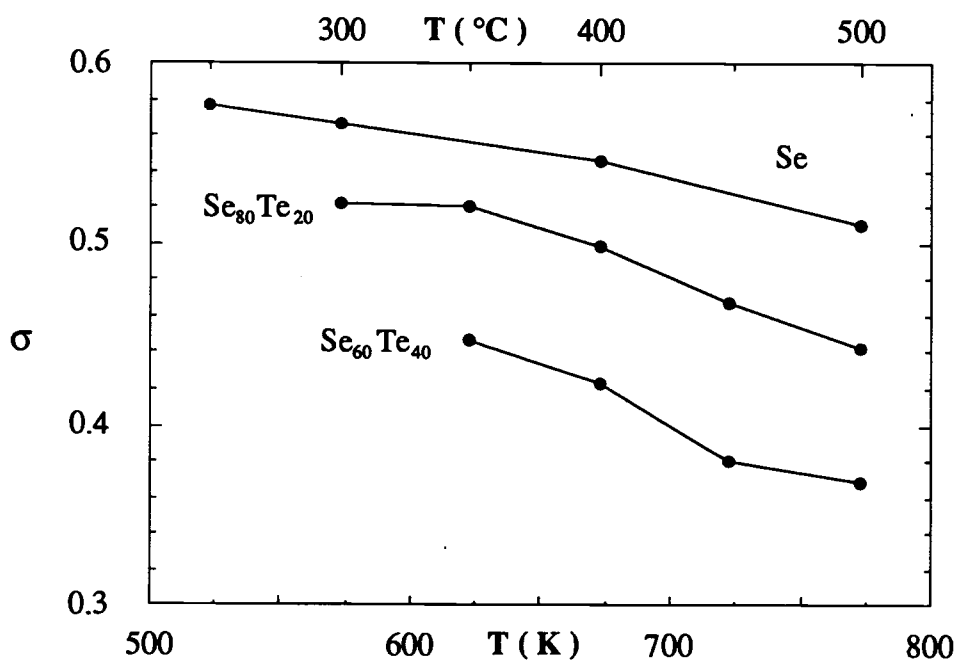


Fig 6.4 The temperature dependence of the steepness parameter.

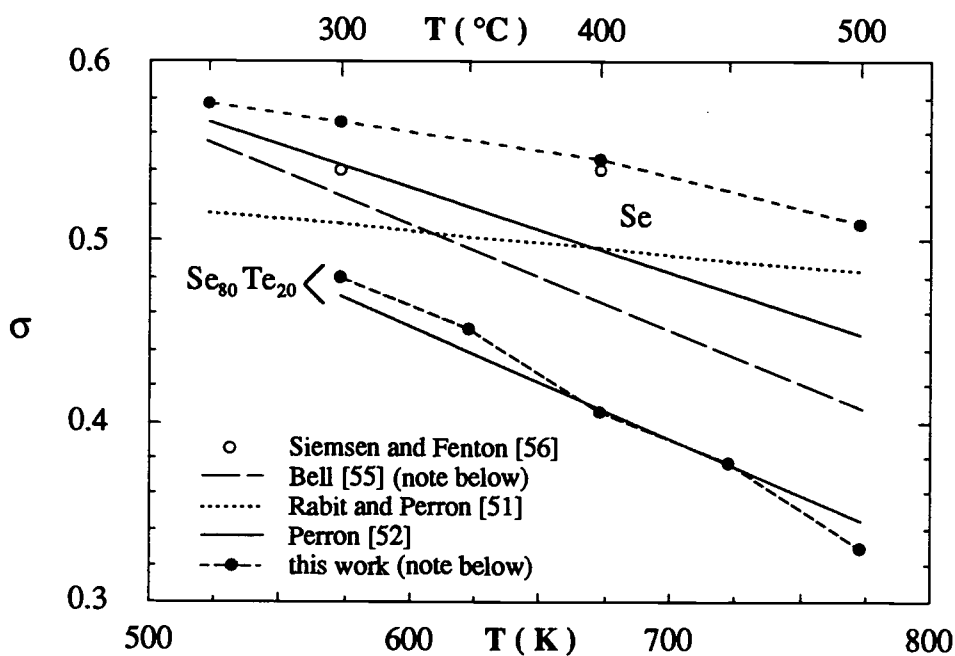


Fig 6.5 Values for the steepness parameter  $\sigma$  from different measurements. Note that for the purpose of comparison to Perron's 20% Te alloy data the values shown for  $\sigma$  from this work were calculated using the same absorption interval measured by Perron. Also, the values for Bell's measurements were determined from his data for  $\alpha$  in the range of 10 to 1000  $\text{cm}^{-1}$ .

temperature dependence of the steepness parameter for liquid Se. The new data for  $\sigma$  are larger than previous values, which means that at a given temperature the absorption edge of Se shown in Fig 6.1 is steeper than has previously been observed. The five measurements of  $\sigma$  in Fig 6.5 show a general trend in decreasing with temperature, but the slopes are inconsistent. In the lower part of Fig 6.5 the slope of the absorption edge in  $\text{Se}_{80}\text{Te}_{20}$  measured by Perron is compared to the new measurements. In order to make a fair comparison with Perron's results the values of  $\sigma$  shown for the new data were calculated using the same range of the absorption coefficient measured by Perron. Part of his data fell in the region which appears as being non-exponential in Fig 6.2, and because of this the data points for  $\sigma$  are lower than those given in Fig 6.4. In view of the scatter in the data for pure Se, the agreement between these two measurements is very good-- but may only be fortuitous.

What experimental factors could produce the variations between the measured values of  $\sigma$ ? It cannot be attributed to inaccuracies in the values used for the thicknesses of the liquid films because an error in the thickness would only shift the entire calculated absorption curve along the  $\alpha$ -axis, and not change the slope. Nor do inaccuracies in the temperature measurements provide a plausible explanation, because the temperature errors that would be required are much too large. If the scatter in the data were due to differences in the amount of impurities present in the samples this would imply a fairly large sensitivity of the optical behavior to impurity concentration. However, the work done by Bell and Cutler on Se-Tl alloys indicates that the optical behavior is relatively insensitive to the presence of impurities. The introduction of small amounts of Tl in Se is expected to shorten the length of the Se chains, and also form diatomic TlSe molecules in the liquid. These are significant changes in the liquid structure, but Bell and Cutler's

optical data for Se containing 0.1% Tl (a concentration much larger than that of any possible impurity) show only a small decrease in the slope of the absorption edge compared to pure Se.

There are two factors which may explain the differences in the data for the steepness parameter. First, it may be that the absorption edge is not accurately of exponential form. Different ranges of the absorption coefficient were used to determine  $\sigma$ , and if the edge has a small positive curvature in a  $\log(\alpha)$  vs.  $\hbar\omega$  plot this could explain part of the discrepancies between the data. And secondly, it could be a matter of errors associated with using different optical spectrometers to do the same measurement. The data shown in Fig 6.5 were taken with spectrometers using different light detectors, dispersion techniques, and different designs to couple the light in and out of the sample. In the experimental work presented in this paper it was found that spurious light signals and changes in the detector gain associated with the infrared radiation produced by the oven were troublesome problems which had to be dealt with carefully. It may be that effects of the oven radiation were not completely removed in some of the spectrometer designs, including the one used here.

## 6.2 Absorption Processes in the Liquid

Interest in the optical properties of liquid Se dates back to work done by Hartke and Regensburger on the properties of amorphous Se [57]. The optical behavior of amorphous Se is unusual among amorphous solids in that the temperature dependence of the slope of the edge varies roughly as  $1/kT$ , whereas in most amorphous solids it is independent of temperature [60]. Measurements of the optical absorption and quantum efficiency for photoconduction by Hartke and Regensburger showed that the quantum efficiency curve is shifted to higher photon

energies with respect to the absorption curve. There is a region of about 0.5eV in the vicinity of the absorption edge where the photon absorption is large, but free carriers are not produced. Hartke and Regensburger used the energy dependence of the quantum efficiency to separate their optical data into two parts: one associated with an absorption process that produces photoconductivity, and another which does not produce photoconductivity. They determined that the mechanism responsible for the nonphotoconductive absorption also gives the exponential form of the absorption edge. This they attributed to phonon-broadened excitonic absorption below the optical band gap, and they used an early version of Toyozawa's theory for the optical absorption by self-trapped excitons to explain their results. Later, Siemsen and Fenton [56] measured the optical absorption in amorphous and liquid Se as a function of temperature to see if Toyozawa's model could also account for the temperature dependence of the edge. Their results indicated that Toyozawa's theory could explain the temperature shift in the absorption edge, but their calculations were based on the assumption that the energy dependence of the quantum efficiency does not change with temperature. Subsequent photoconductivity measurements on liquid Se by Vengris [58], and Rabit and Perron [51] showed that this was not true for the liquid phase. In liquid Se the energy dependence of the absorption edge and the efficiency for the photogeneration of free carriers parallel one another fairly well, and do not show the large energy shift observed in amorphous Se. This implies that there is something different about the absorption processes occurring in the liquid form of Se compared to the amorphous solid.

Other models for the origin of the exponential absorption edge in liquid Se have been proposed. Perron suggested that the density of states band-tailing model (section 1.2.2) could explain the behavior of the edge, but this view has not

gained acceptance. Rabit and Perron suggested that the Dow-Redfield model for excitonic absorption in the presence of microfields may be applicable to liquid Se. They proposed that bond distortions in the liquid could produce the microfields required by the Dow-Redfield model, but they did not provide any theoretical work to support this hypothesis. As the electronic properties of liquid semiconductors became better understood, it was found that bond defects in the liquid play a significant role in electronic transport processes. As an extension of this, Bell and Cutler proposed that the microfields produced by charged bond defect states in the liquid could contribute to the optical absorption via electric field assisted electron-hole tunneling. They performed measurements on the absorption edge of Se-Tl alloys containing 0-0.1% Tl in the temperature range of 250 - 500°C. By assuming that the concentration of ionic defects due to the presence of Tl is thermally activated, they were able to model the absorption of the liquid at energies below half the optical band gap using the Dow-Redfield theory. They explained the differences appearing in their absorption data above and below  $E_g/2$  in terms of the absorption efficiencies that would be expected in the fields near a pair of oppositely charged ions, and the the fields near single ions.

It appears that the absorption of photons by excitons, modified by phonon interactions and the presence of strong fields near ionic defects, determine the behavior of the absorption edge in liquid Se and Se-Te alloys. At present there is insufficient information available concerning the concentration of ionic defects in Se-Te alloys to look for a correlation between the optical data and the density of these defects. It is clear that primary effects of adding Te to Se are to shift the absorption edge to lower energies, and to introduce a non-exponential tail in the absorption edge. The energy shift of the absorption edge is easily understood in terms of changes in the band structure caused by differences in the covalent bond energies



between Se and Te atoms. The tailing of the edge, on the other hand, appears to be unusual compared to other liquid semiconductors, and is not as readily explained. Liquid semiconductors whose absorption edges have been measured include S, AsSe, As<sub>2</sub>Se<sub>3</sub>, and Ge<sub>10</sub>Se<sub>90</sub>. The optical behavior of these liquids remains exponential down to at least 10 cm<sup>-1</sup> before any tailing in the edge appears. One possible way to explain the increase in the absorption coefficient at low energies in Se-Te alloys is to assume that the Te atoms tend to bond together more often than with other Se atoms. This would produce inhomogeneities in the dielectric constant in the liquid, which could cause a significant amount of scattering of the incident light. Optical scattering of this type has been observed in liquid sulfur at temperatures near the polymerization transition [59], though at lower absorption levels than the data in Figs 6.2 and 6.3 would indicate for these liquids. It should be pointed out, however, that no evidence for concentration inhomogeneities appears in the behavior of the optical data above the band gap. Consequently, this explanation for the tailing of the edge is doubtful. A better understanding of the optical absorption edge in Se-Te liquids will require further research.

## 7. Summary

This research has shown that it is possible to prepare liquid semiconductor films which are thin enough to measure the optical transmissivity at energies above the band gap. Transmissivity measurements, used along with measurements of the reflectivity of the liquid, provide a more direct means of determining the optical properties than techniques which use the reflectivity alone. Two methods have been developed to prepare films of Se-Te alloys: the thin-film evaporation technique, and the compressed liquid technique. Both techniques can be used to prepare thin films of other semiconductor liquid systems. The most important consideration in applying these techniques is the choice of material to use for the optical windows. They must be chemically inert when in contact with the sample liquid, and also as rigid as possible to minimize the distortion of their surfaces while under pressure. In the thin-film evaporation technique the gasket material must also be chemically inert, both with respect to the liquid sample and the windows. The density and hardness of the gasket film are also important considerations. The minimum film thickness which is practicable with these film preparation techniques ( $0.2\mu\text{m}$ ) sets the limit on the maximum absorption coefficient that can be measured at about  $5 \times 10^5 \text{ cm}^{-1}$ . The optical properties of semiconductors and semimetals can be measured within this limit, but transmissivity measurements on liquid metals would require films thinner by an order of magnitude.

The optical measurements performed on the Se-Te alloy system covered the composition range from pure Se to pure Te in concentration steps of 20 atomic percent, and the temperatures from the melting point to  $500^\circ\text{C}$ . In the range of temperature and composition where the liquids are semiconducting, possible forms

for the band structure have been determined using the non-direct transition model. The NDT model by itself is not sufficient to determine the band structure from the optical data because it contains three energy-dependent functions  $N_c(E)$ ,  $N_v(E)$ , and  $|M(h\omega)|^2$ . Measurements of other properties of this liquid system, along with general considerations about the optical properties of disordered materials, have suggested three possible ways to interpret the optical data:

1) *The density of states in the conduction and valence bands are symmetric.* This possibility is motivated by the band structure calculations of Joannopoulos *et al* for amorphous Se, and the fact that the optical properties of amorphous and liquid Se are very similar. The band structure calculated by taking  $N_c(E)=N_v(E)$ , and assuming the energy dependence in the matrix element function is negligible, gives liquid Se steep band edges which gradually broaden as the temperature and Te concentration are increased.

2) *The valence band edge is parabolic, and the electrons in the conduction band behave as one-dimensional states.* Theoretical work done by Kao and Cutler on the electronic properties of these liquids suggests that the valence band depends on energy roughly as  $E^{1/2}$ . The power sum-rule in the NDT model,  $r=r_c+r_v+1$ , relates the curvature of the band edges to the curvature of the quantity  $\epsilon_2(h\omega)^2$ . Considering  $r=1.1$  for liquid Se, a parabolic valence band requires  $N_c(E) \propto E^{-1/2}$ . This implies that the wavefunctions of the conduction band edge behave as one-dimensional states.

3) *Both the conduction and valence band edges are parabolic.* This possibility is motivated by the fact that in many amorphous semiconductors the optical data can be fit by using a simple parabolic band edge model. In amorphous materials the parabolic fit is achieved with the condition that  $|M(h\omega)|^2$  is energy independent. In

the case of the semiconducting Se-Te liquids the energy dependence of  $|M(h\omega)|^2$  would have to be considerable to account for the optical data.

These three forms for the density of states structure represent three extremes of simplification within the NDT model. Most likely they are all an oversimplification of the actual electronic structure of the liquid, but they do indicate possibilities to consider in future experimental and theoretical work. Because the optical properties of liquid Se are very similar to those of amorphous Se, any advancement in the understanding of the electronic structure of amorphous form would also bear upon the liquid.

The most significant result of the optical measurements is that they support the hypothesis that the two-fold bonding structure of the semiconducting liquids is maintained across the semiconductor-semimetal transition. By subtracting the intraband contribution to the optical behavior of Te it was shown that there is a gap between the occupied electron states below the Fermi energy and the bottom of what was formerly the conduction band in the semiconducting state. The width of this energy separation is approximately 0.4eV. This result is consistent with the semiconductor-semimetal transition model proposed by Cutler, and inconsistent with other models which propose that the transition is due to a change in structure from 2-fold covalent bonds to networking 3-fold covalent bonds.

The uncertainty in the magnitude of the energy separation between the Fermi level and the conduction band edge ( $E_1$  in Fig 5.1 ) is due in part to the limited veracity of the Drude model used to derive this result, and also the uncertainty in the values used for the free-carrier density and mass. It would be interesting to perform additional measurements on liquid Te at lower photon energies, where the electron states near the Fermi level dominate the optical

behavior. The slope of the absorption coefficient curve should decrease markedly at some point below 0.4eV. The energy at which this decrease occurs would give a more direct means of determining the value of  $E_1$ . It may be possible to extend the measurements down to 0.2eV with the same film preparation techniques used here by replacing the fused quartz windows with sapphire windows.

The optical properties of the absorption edge in the Se-rich alloys have been measured. Adding Te to Se shifts the band gap, and thus the absorption edge, to lower energies. It also has the effect of introducing a non-exponential tail in the absorption coefficient, which increases in magnitude with temperature and Te concentration. It was shown that the temperature dependence of the exponential portion of the edge is given by the slope factor  $\sigma/kT$  in the Urbach equation, with the steepness parameter  $\sigma$  decreasing as the temperature or Te concentration is increased. The exponential portion of the edge could be expressed as  $\alpha = e^{12.0} e^{(\hbar\omega - E_0)\sigma/kT}$  for liquids containing 0, 20, and 40 atomic percent Te. The energy term  $E_0$  is a function of composition alone, and approximately equal to the band gap energy of the liquid. A comparison of the results for  $\sigma$  with previous measurements has shown that this parameter has not been defined well. The discrepancies between the data could be attributed to the absorption edge not depending on photon energy in exactly exponential form, or to undetected errors produced by the various spectrometers used to make these measurements.

**BIBLIOGRAPHY**

1. N.F. Mott and E.A. Davis, Electronic Processes in Non-Crystalline Materials, Clarendon Press, Oxford (1971), p. 402.
2. T.E. Faber, Introduction to the Theory of Liquid Metals, Cambridge University Press (1972).
3. K. Sturm and E. Pajanne, J. Phys. F **3**, 199 (1972).
4. M.P. Tosi, M. Parrinello, and N.H. March, Nuovo Cimento B **23**, 135 (1974).
5. E.T. Arakawa, T. Inagaki, and M.W. Williams, Surface Science **96**, 248 (1980).
6. T. Inagaki, E.T. Arakawa, A.R. Cathers, and K.A. Glastad, Phys. Rev. B. **25**, 6130 (1982).
7. J. Tauc, Prog. Semiconductors **9**, 87 (1965).
8. N.K. Hindley, J. Non-Cryst. Solids **5**, 17 (1970).
9. M. Zavetova and A. Abrahams, J. Non-Cryst. Solids **29**, 383 (1978).
10. E.A. Davis, J. Non-Cryst. Solids **4**, 107 (1970).
11. K. Maschke and P. Thomas, Phys. Stat. Sol. **41**, 743 (1970).
12. S. Abe and Y. Toyozawa, J. Phys. Soc. Jpn. **50**, 2185 (1981).
13. U. Dersch, M. Grünewald, H. Overhof, and P. Thomas, J. Phys. C **20**, 121 (1987).
14. J.N. Hodgeson, Phil. Mag. **8**, 735 (1963).
15. K. Tamura, H.P. Seyer, and F. Hensel, Ber. Bunsenges. Phys. Chem. **90**, 581 (1986).
16. H.P. Seyer, K. Tamura, H. Hoshino, H. Endo, and F. Hensel, Ber. Bunsenges. Phys. Chem. **90**, 587 (1986).
17. R. Fainschtein and J.C. Thompson, Phys. Rev. B. **27**, 5967 (1983).
18. D.M. Trotter, Jr., U. Evan, and J.C. Thompson, Phys. Rev. B **17**, 4004 (1978).

19. R. Fainchtein, U. Even, and J.C. Thompson, *J. Non-Cryst. Solids* **61/62**, 47 (1984).
20. W. Hefner, R.W. Schmutzler, F. Hensel, *J. Phys. (Paris) Colloq.* **41**, 21 (1980).
21. H.W. Verleur, *J. Opt. Soc. Am.* **58**, 1356 (1968).
22. H. Sumi and Y. Toyozawa, *J. Phys. Soc. Jpn.* **31** (1971).
23. J.D. Dow and D. Redfield, *Phys. Rev. B* **1**, (1970).
24. M. Schreiber and Y. Toyozawa, *Physica B* **117/118**, 290 (1983).
25. T. Skettrup, *Phys. Rev. B* **18**, 2622 (1978).
26. A.V. Kolobov, O.V. Konstantinov, Semiconductor Physics, (ed. V.M. Tuchkevich and V. Frenkel), Consultants Bureau, New York, (1986).
27. M.H. Cohen, C.M. Soukoulis, and E.N. Economou, *AIP Reports*, No. 120, 371 (1984).
28. S. John, C. Soukoulis, M.H. Cohen, and E.N. Economou, *Phys. Rev. Lett.* **57**, 1777 (1986).
29. J.D. Wiley, D. Thomas, E. Schönherr, and A. Breitschwerdt, *J. Phys. Chem. Solids* **41**, 801 (1980).
30. E. Mohler and B. Thomas, *Phys. Rev. Lett.* **44**, 543 (1980).
31. F.G. Bell and M. Cutler, *Phys. Rev. B* **34**, 5270 (1986).
32. J.D. Joannopoulos, M. Schlüter, and M.L. Cohen, *Phys. Rev. B* **11**, 2186 (1975).
33. J. Stuke, *J. Non-Cryst. Solids* **4**, 1 (1970).
34. V.N. Bogomolov, S.V. Kholodkevich, S.G. Romanov, and L.S. Agroskin, *Sol. State Comm.*, **47** 181 (1983).
35. S.S. Kao and M. Cutler, *Phys. Rev. B* **37**, 10581 (1988).
36. S.S. Kao and M. Cutler, *Phys. Rev. B* **38**, 9457 (1988).
37. J.A. Gardner and M. Cutler, *Phys. Rev. B* **20**, 529 (1979).
38. H. Thurn and J. Ruska, *J. Non-Cryst. Solids* **22**, 331 (1976).

39. K. Takimoto and J. Ruska, *Phys. Chem. Liq.* **12**, 141 (1982).
40. S. Takeda, H. Okazaki, and S. Tamaki, *J. Phys. Soc. Jpn.* **54** (1985).
41. R. Billissent and G. Tourand, *J. Non-Cryst. Solids* **35/36**, 1221 (1980).
42. J.R. Magaña and J.S. Lannin, *Phys. Rev. B* **29**, 5663 (1984).
43. H. Richter, *J. Non-Cryst. Solids* **8/10**, 388 (1972).
44. B. Cabane and J. Friedel, *J. Phys.* **32**, 73 (1971).
45. G. Tourand and M. Breuil, *J. Phys* **32**, 813 (1971).
46. M. Cutler, Liquid Semiconductors, Academic Press (1977).
47. A. Menelle, R. Billissent, and A.M. Frank, *Europhysics Letts.*, **4**, 705 (1987).
48. M.E. Welland, M. Gay, and J.E. Enderby, Physics of Disordered Systems, eds D. Adler *et al*, Plenum Press (1985).
49. L.A. Silva and M. Cutler, *Rev. Sci. Inst.*, to be published.
50. A reference for this, and related topics, is Semiconductor Opto-Electronics, T.S. Moss, G.J. Burrell, and B. Ellis, John Wiley & Sons (1973).
51. J. Rabit and J.C. Perron, *Phys. Stat. Sol.(b)* **65**, 255 (1974).
52. J.C. Perron, Doctoral Thesis, University of Paris (1969).
53. M. Cutler and H. Rasolondramanitra, Localization and Metal-Insulator Transitions, eds H. Fritsch and D. Adler, p199, Plenum Press (1985).
54. M. Cutler, S.S. Kao, and L. Silva, manuscript in preparation.
55. F. Bell, Doctoral Thesis, Oregon State University (1986).
56. K.J. Siemsen and E.W. Fenton, *Phys. Rev.*, **161**, 632 (1967).
57. J.L. Hartke and P.J. Regensburger, *Phys. Rev.*, **139**, 970 (1965).
58. S.A. Vengris, Y.K. Vishchakas, A.P. Sakalas, and G.B. Yushka, *Soviet Phys.-Semicond.*, **6**, 903 (1972).
59. M. Zanini and J. Tauc, *Applied Optics*, **15**, 3149 (1976).
60. K.L. Chopra and S.K. Bahl, *Thin Solid Films*, **11**, 377 (1972).



## **APPENDIX**

## Appendix A

### Methods for Producing Thin Films of High Temperature Liquids

L.A. Silva and M. Cutler

Physics Department, Oregon State University, Corvallis, Oregon 97331

We describe the techniques we have developed to make micron size films of liquid  $\text{Se}_x\text{Te}_{1-x}$  alloys. Two approaches were employed. In the first, a vacuum evaporated sample film and a surrounding evaporated gasket are sandwiched between two optical windows, and the sample is then melted to obtain the liquid. In the second, a drop of the sample liquid is compressed in a cavity between two windows. By varying the gasket thickness and the cavity depth, liquid films with thicknesses ranging from  $0.3\mu\text{m}$  to  $25\mu\text{m}$  were prepared with temperatures between  $250^\circ\text{C}$  and  $500^\circ\text{C}$ .

[Submitted to The Review of Scientific Instruments in January, 1989. To be published in the September 1989 issue.]

As part of an ongoing line of research, we wished to measure directly the optical properties of the semiconducting liquid system  $\text{Se}_x\text{Te}_{1-x}$  at energies near and above the bandgap. This type of experiment requires the use of very thin liquid samples, of order  $1\mu\text{m}$  or less, to make transmissivity measurements feasible above the bandgap. In addition these films must be prepared and maintained at temperatures above the melting point of the alloy, which ranged from  $250^\circ\text{C}$  ( $x=1$ ) to  $450^\circ\text{C}$  ( $x=0$ ). In the past the samples used to measure the optical transmission of high temperature liquid semiconductors were usually prepared by injecting the liquid into a cavity between optical windows<sup>1</sup>. In our lab we tried to extend this technique to a cell with a cavity width of  $2\mu\text{m}$ , and found that while it is possible to force the fluid into the cavity with a modest amount of pressure ( $\sim 30$  psi) a continuous film does not form. Surface forces and microscopic irregularities in the windows cause the fluid to flow in a few narrow channels through the cavity.

Since there seemed to be no way to force a continuous liquid film into the cavity we thought it might be possible to start with a *solid* film between the windows which could be melted to obtain the liquid film. This is the first approach we used; the optical cell design is shown schematically in Fig 1. The cell is made by evaporating the various films shown onto the surface of an optically flat fused quartz window using a multiple film vacuum evaporation unit. Ignoring the  $\text{CaF}_2$  layer for the moment, the basic idea is to form an annular shaped gasket of  $\text{ZnS}$  with the thickness of the liquid film desired, and then evaporate the constituents of the alloy sample inside the gasket. A second quartz window is placed on top, and this cell is placed in a clamp and pressed together. The clamp design we used is also shown in Fig 1. It is necessary to press the two windows together with a uniform surface force to minimize the deformation of the windows while under

pressure. We found that by using accurately machined cylindrical clamp faces and a ratio of cavity diameter to window thickness less than one, the distortion was small enough to not affect the measurements.

Although this approach seems straightforward, a series of pitfalls were immediately encountered involving the microstructure of the evaporated films. We tried and rejected several materials for the gasket, either because they were too soft and deformed excessively under pressure or they allowed the liquid to leak through. ZnS was chosen in the end because it had the right mechanical properties and it was chemically compatible with Se and Te. Another problem we had to contend with was the porosity of the sample film itself. An evaporated selenium film, for example, has a density of  $4.2 \text{ gm/cm}^3$  -- compared to a bulk crystal density of  $4.8 \text{ gm/cm}^3$ . As an evaporated Se film is heated it anneals at a temperature well below the melting point, which allows the voids in the film to coalesce and form gaps in the solid. Then as the temperature is raised above the melting point any gas within the gaps is trapped by the liquid, resulting in a liquid film full of many small transparent bubbles. Through a process of trial and error it was found that by putting a very thin layer of  $\text{CaF}_2$  on the cavity surfaces of the window and applying a large pressure to the cell ( $>250 \text{ psi}$ ) the bubbles could be forced out of the film.

An example of the data obtained for a liquid selenium film prepared by this technique is shown in Fig 2. Liquid Se has a bandgap of  $2\text{eV}$  with a broad exponential absorption edge extending through the infrared<sup>2</sup>. The uniformity of the liquid film can be inferred from the magnitude of the interference minima of the reflectivity curve. At long wavelengths, where the absorption in the film becomes negligible, the minima should go to zero as is seen in figure 2; if the film was significantly distorted then the minima would be higher. Films of Se and Se with 20at.% Te as thin as  $0.3\mu\text{m}$  and as thick as  $2\mu\text{m}$  have been prepared using this

technique. The temperature could be varied from 250°C to 450°C without losing the sample.

The second technique we used to prepare thin film samples is perhaps the simplest one imaginable: a small solid piece of a previously melted alloy is placed into the cell cavity, it is remelted, and then the windows are pressed together to make a film. The cell design we first used in this way is shown in Fig 3a. In this case, the gasket is made from two stamped pieces of 12 $\mu$ m aluminum foil, one with a slightly smaller inner diameter than the other. The steps used in making a film were as follows. First an amount of the alloy almost sufficient to fill the cell cavity when melted was measured using a Cahn microbalance. This mass was typically ~2mg. Then the two quartz windows were placed in the clamp with the aluminum gasket resting on the lower window and the upper window raised 5mm so the sample could later be inserted into the cavity. This arrangement was placed inside an oven and heated to a temperature 10°C below the melting point of the alloy. The sample was inserted into the cavity, the temperature raised above the melting point, and then the clamp screws were tightened to press the windows together. In this process a liquid drop is compressed into a thin film which fills the optical cavity; any excess liquid spills over the step in the aluminum gasket.

To make thinner liquid films it is possible to use thinner metal foils, but foils less than about 5 $\mu$ m in thickness are difficult to manipulate without damaging. We found another way to make the cavity which dispenses of the gasket altogether. Instead of using a gasket to form the sample cavity a depression is etched into the surface of one of the optical windows using hydrofluoric acid (Fig. 3b). The depression formed by the acid was found to be as optically flat as the initial window surface, and pitting of the surface was slight. A very thin (50Å) aluminum film was evaporated on the quartz surface surrounding the etched depression to prevent the

quartz windows from fusing together when they were pressed together at high temperatures. Using an etched depression, liquid films as thin as  $0.5\mu\text{m}$  were prepared by the compressed-liquid method. Thinner films were not practicable because the sample size became very small and hard to manipulated, and the small liquid drop it formed tended not to flow into a continuous film when compressed.

This work was supported by National Science Foundation grant No. DMR-8320547.

### **References:**

- 1) F.G. Bell and M. Cutler, Rev. Sci. Inst. **57**, 1129 (1986).
- 2) J. Rabit and J.C. Perron, Phys. Status Solidi B, **65** 255 (1974).
- 3) Grafoil is a product of Union Carbide Corporation, Carbon Products Division.

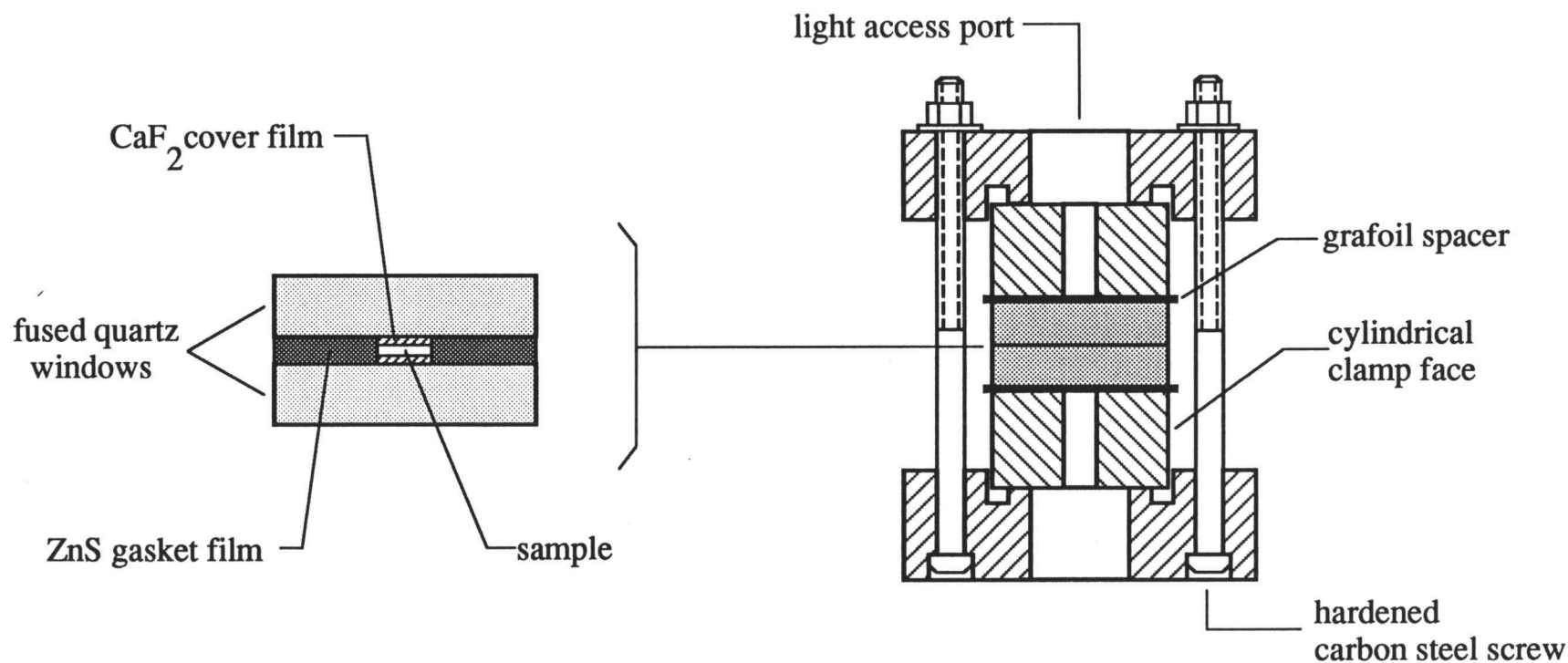


**Fig 1** The optical cell and clamp. At left is an expanded view of the optical cell showing how the evaporated films are arranged. The fused quartz windows are 1/4" thick, 1" in diameter, and are flat to within 0.1 $\mu$ m. At right is a sectional view of the steel clamp with the cell in place. Six screws are spaced around the perimeter of the clamp, which are tightened to apply pressure to the cell. The grafoil spacers provide a cushion between the clamp faces and the windows.

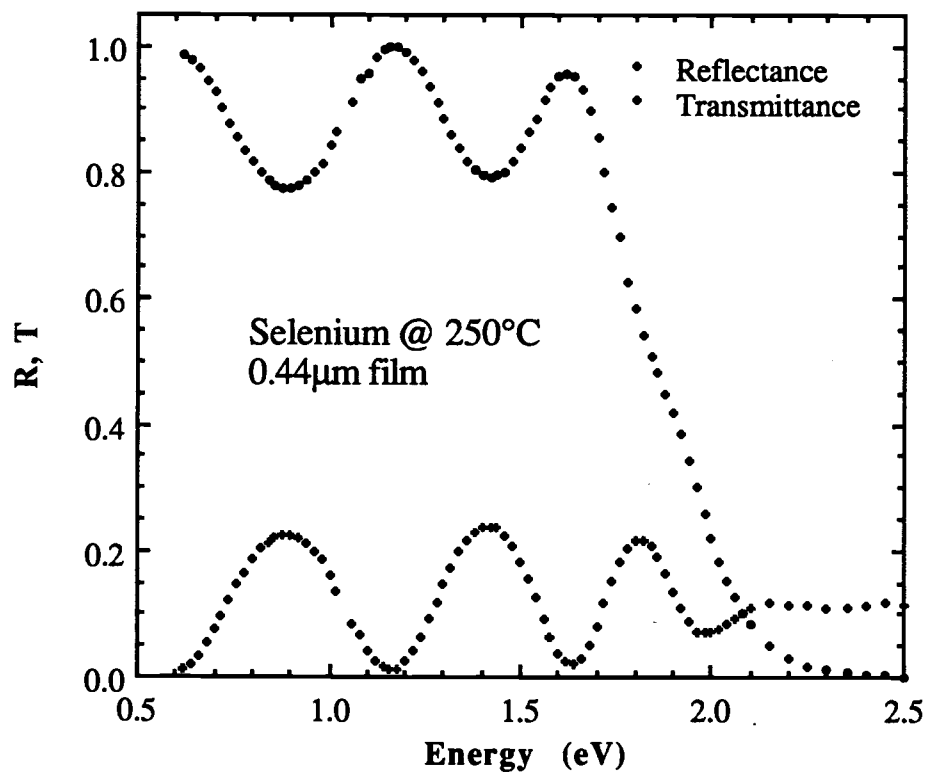


**Fig. 2** An example of the measurements obtained using the optical cell shown in Fig.1



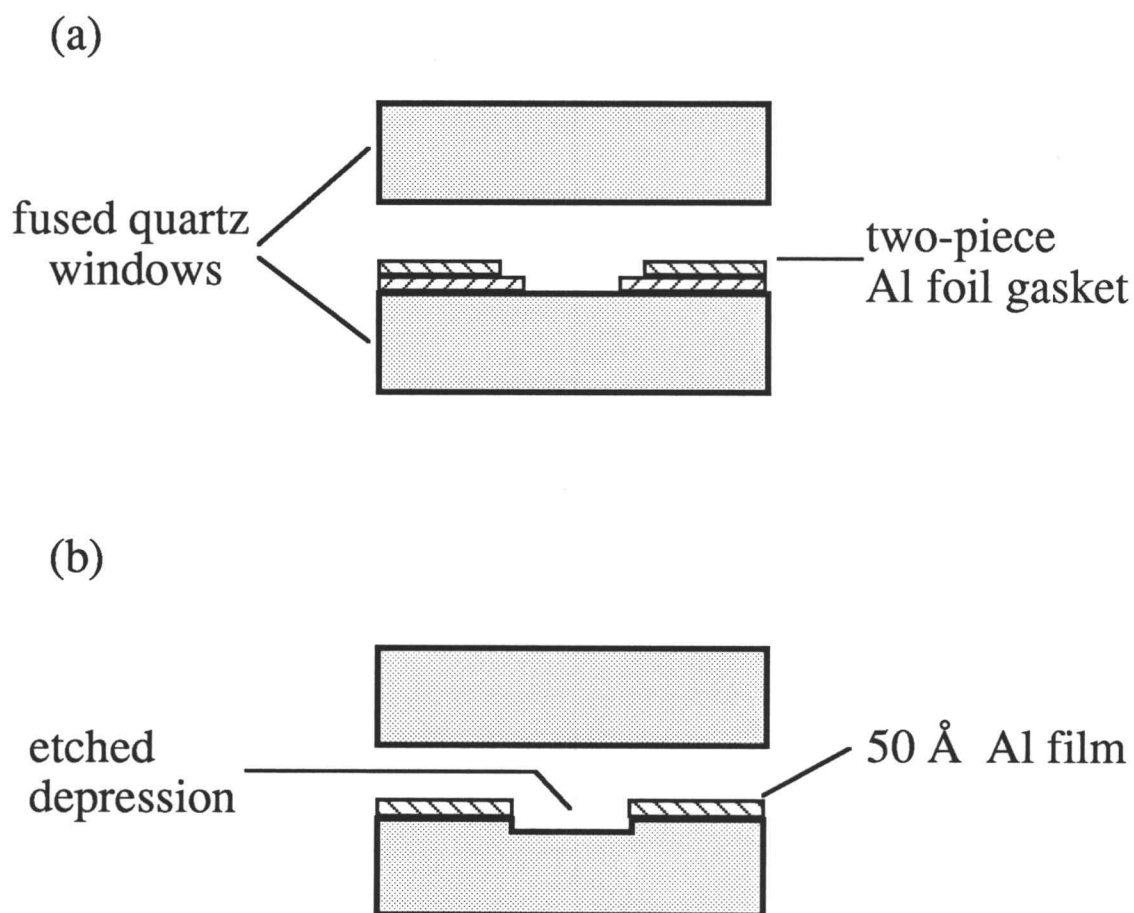


**Fig. 3** Two optical cell designs used with the compressed-liquid technique. (a) The cell cavity is formed by two stamped pieces of Al foil, each with a thickness of  $12\mu\text{m}$ . (b) The cell cavity is formed by etching one of the quartz windows with HF acid. The  $50\text{\AA}$  Al film prevents the windows from fusing together at high temperatures.